CHARM PRODUCTION BY MUONS AND ITS ROLE IN SCALE-NONINVARIANCE

George D. Gollin

October, 1980

CHARM PRODUCTION BY MUONS AND ITS ROLE IN SCALE-NONINVARIANCE

GEORGE D. GOLLIN

A DISSERTATION

PRESENTED TO THE

FACULTY OF PRINCETON UNIVERSITY

IN CANDIDACY FOR THE DEGREE

OF DOCTOR OF PHILOSOPHY

RECOMMENDED FOR ACCEPTANCE BY THE

DEPARTMENT OF

PHYSICS

JANUARY, 1981

For Melanie

"O frabjous day! Callooh, Callay!"

-Lewis Carroll

ABSTRACT

Interactions of 209 GeV muons in the Multimuon Spectrometer at Fermilab have yielded more than 8×10^4 events with two muons in the final state. After reconstruction and cuts, the data contain 20 072 events with $(81\pm10)\%$ attributed to the diffractive production of charmed states decaying to muons. The cross section for diffractive charm muoproduction is $6.9\pm^{1.1}_{1.3}$ nb where the error includes systematic uncertainties. Extrapolated to $Q^2=0$ with $\sigma(Q^2)=\sigma(0)(1+Q^2/\Lambda^2)^{-2}$, the effective cross section for 178 (100) GeV photons is $750\pm^{80}_{90}$ ($560\pm^{200}_{120}$) nb and the parameter Λ is 3.3 ± 0.2 (2.9 ± 0.2) GeV/c. The ν dependence of the cross section is similar to that of the photon-gluon-fusion model. A first determination of the structure function $F_2(c\bar{c})$ for diffractive charm production indicates that charm accounts for approximately 1/3 of the scale-noninvariance observed in inclusive muon-nucleon scattering at low Bjorken x. Okubo-Zweig-Iizuka selection rules and unitarity allow the muon data to set a 90%-confidence lower limit on the ψN total cross section of 0.9 mb.

TABLE OF CONTENTS

LIST OF TABLES

LIST OF FIGURES

CHAPTER I

INTRODUCTION

A brief history of the quark model

There is great appeal in ascribing the rich phenomenology of high energy physics to the interactions of a small number of fundamental particles. Faced with a growing zoo of subatomic particles, Fermi and Yang suggested in 1949 that pions might be composite objects.[1] They boldly calculated the properties that a nucleon-antinucleon state would exhibit (antiprotons were not discovered until 1955) and found them similar to those of the pion. In 1956 Sakata proposed an extension to the Fermi-Yang theory to allow it to describe strange particles.[2] Sakata's model used the neutron, proton, and lambda as building blocks and predicted the existence of several unusual (and nonexistent) particles such as mesons with strangeness +2 and baryons with strangeness -3 and isospin 1.[3] Six years later, Gell-Mann and Ne'eman developed the "eight-fold way," a classification scheme for mesons and baryons based on the group SU(3).[4] The "eight-fold way" of 1962 treated particle symmetries

abstractly, temporarily abandoning the Sakata model's notion of three fundamental hadron constituents. Encouraged by the success of the SU(3) model, in 1964 Gell-Mann was "tempted to look for some fundamental explanation of the situation."[5] He found that the observed hadron SU(3) multiplets could be constructed from a unitary triplet (d^- s^- u^0) and a baryon singlet b^0. More interesting to Gell-Mann was a simpler scheme which postulated three fractionally charged, spin 1/2 "quarks," each with baryon number 1/3. Baryons would be composed of three quarks or four quarks and an antiquark, etc. while mesons would be constructed from equal numbers of quarks and antiquarks.[5] Soon after, Greenberg introduced an extra degree of freedom, later to become color, into the quark model to permit the symmetric combination of three quarks in an s state.[6]

Hadron spectroscopy provided ample experimental support for the SU(3) symmetry of the "eight-fold way." Indications that quarks themselves have physical as well as mathematical significance came from several sources. The cross section for inelastic electron-proton scattering may be written in terms of two structure functions, W_1 and W_2 as

$$\frac{d^2\sigma}{dQ^2 d\nu} = \frac{E'}{E}\,\frac{4\pi\alpha^2}{Q^4}\left[\, W_2(Q^2,\nu)\cos^2\frac{\theta}{2} + 2W_1(Q^2,\nu)\sin^2\frac{\theta}{2}\right].$$

Here, E and E' are the energies of the incident and scattered electron, ν is E-E', and Q^2 is the square of the

four-momentum transferred from the electron. Experimenters at the Stanford Linear Accelerator Center (SLAC) found that W_2 depended weakly on Q^2 and that νW_2 depended only on the ratio Q^2/ν. This suggested that beam electrons were scattering elastically from point-like particles inside target protons.

More support for the existence of quarks came from measurements of muon-pair production in pion-nucleon and proton-nucleon collisions. In the spirit of the quark model, most non-resonant muon pairs should come from quark-antiquark annihilation[7] as shown in Fig. 1. Since pions contain valence antiquarks while protons do not, the ratio $\sigma(pN \rightarrow \mu^+\mu^- X)/\sigma(\pi N \rightarrow \mu^+\mu^- X)$ should be much less than 1. This was seen to be true.[8]

Charm

The unitary triplet, baryon singlet model discarded by Gell-Mann led Bjorken and Glashow in 1964 to study a constituent model for hadrons in which four fundamental "baryons" were linked by SU(4) symmetric forces.[9] Baryon number, electric charge, hypercharge, and a new quantum number, charm, were conserved quantities in their theory. They predicted that charmed mesons would have masses of

approximately 760 MeV and noted that their model was "vulnerable to rapid destruction by the experimentalists."[9] Six years later, Glashow, Iliopoulos, and Maiani (GIM) proposed another SU(4) charm model, this time a four quark extension of Gell-Mann's three quark theory.[10] The GIM model eliminated strangeness-changing neutral currents from the Weinberg-Salam model of weak interactions, which previously had predicted anomalously high rates for the decays $K_L \to \mu^+\mu^-$ and $K^+ \to \pi^+\nu\bar{\nu}$.

The ψ was discovered in proton-beryllium collisions and in electron-positron annihilation in 1974.[11] Its narrow width indicated that the ψ did not decay strongly and suggested that it was a bound state of a new quark and its antiquark, the charmed quark of the GIM model. The lightest charmed mesons, the $D^0(1863)$ and $D^+(1868)$ were observed at the Stanford electron-positron collider, SPEAR, in 1976. The D^0 was seen as a narrow peak in the invariant mass distributions of $K^-\pi^+$ and $K^-\pi^+\pi^+\pi^-$ systems and the D^+ as a bump in masses of $K^-\pi^+\pi^+$ states.[12] The system recoiling against the D was found to be always at least as massive as the D, evidence for the associated production of the new mesons. Excited states of the ψ and heavier charmed particles such as the D^*, F, χ, and Λ_c have also been observed.[13–15]

Models for charm production by muons

In the simple quark model, nucleons are said to consist of three valence quarks and a surrounding veil of sea quarks and antiquarks. A beam particle can transfer energy and momentum to a virtual charmed quark (or antiquark), creating a charmed particle. Figure 2a illustrates this process for charm muoproduction. A more modern view holds that the sea quarks arise from polarization of the vacuum by the strong interaction field around the nucleon.

Another approach is provided by the vector-meson dominance model (VMD), shown in Fig. 2b. In VMD, charm production is a two step process. A virtual photon (γ_V) from the beam muon's electromagnetic field couples directly to a vector meson, the ψ, which then scatters off the target into a pair of charmed particles.[16] The model assumes that the γ_V-ψ coupling is nearly independent of Q^2 and that the ψ-N scattering is largely diffractive so that the charmed quarks in the exchanged ψ appear in the final state. VMD predicts the Q^2-dependence of the reaction $\gamma_V N \rightarrow c\bar{c}X$ to be $(1 + Q^2/m_\psi^2)^{-2}$, the propagator for the virtual ψ in the Feynman diagram of Fig. 2b. Here, c is a charmed quark and $\bar{c}$ is its antiquark. The model does not predict the ν dependence of charm muoproduction. Unlike the simple quark model, VMD predicts a strong correlation between the momenta

of the daughter particles. VMD describes well the production of the light particles ρ, ω, and ϕ. The larger extrapolation from $Q^2 = 0$ to $Q^2 = m_\psi^2$ required for charm production however is unsettling.[16]

A recent model for heavy-quark muoproduction is the virtual photon-gluon-fusion (γGF) model.[17] Figure 2c shows the Feynman diagram for γGF charm production. A virtual photon from the beam muon fuses with a gluon from the target, producing a charmed quark and antiquark. A $c\bar{c}$ pair with sufficient invariant mass can fragment into a pair of charmed particles. γGF uses elements of quantum chromodynamics (QCD) and makes the following assumptions about the production process. The scale of the strong coupling constant, α_s, is set by the mass of the charm system. Color bookkeeping, the exchange of gluons between the $c\bar{c}$ pair and the target to "bleach" the quark pair of color, is assumed to be a soft process which does not change the γGF predictions. The production process is assumed to be unaffected by the fragmentation of quarks into hadrons. Ordinary parton model calculation rules are used, allowing results to be expressed as cross sections for γ_v-parton $\rightarrow c\bar{c}X$, summed over the contents of the nucleon and integrated over the momentum distributions of the partons.[16]

The γGF model requires some numerical input before it can make predictions. The mass of the charmed quark must be specified. The distribution of momentum fraction x_g for

gluons must be defined. The mass constant Λ used in the definition of α_s must be chosen. Parameters describing properties of the nucleon target, such as -t dependence, must be fixed. Once these are set, the model describes completely the kinematics of charm production. Q^2 and ν dependence, the $c\bar{c}$ pair mass spectrum, and the total production cross section are defined.[16] When a prescription is adopted to allow the quarks to fragment into hadrons, the γGF model describes charmed states observable in the laboratory. The predictions of γGF will be discussed in detail later.

The muon experiment

This thesis describes interactions of the form $\mu N \rightarrow \mu\mu X$ observed in the Multimuon Spectrometer (MMS) at Fermilab. Brief descriptions of the results obtained from these observations have appeared in Refs. 18 and 19. Data from approximately 4×10^{11} 215 GeV beam muons were collected during the first half of 1978. Results from 1.388×10^{11} positive and 2.892×10^{10} negative beam muons are presented, covering the range $0\ (\mathrm{GeV/c})^2 \lesssim Q^2 \lesssim 50\ (\mathrm{GeV/c})^2$ and $50\ \mathrm{GeV} \lesssim \nu \lesssim 200\ \mathrm{GeV}$. After reconstruction and cuts, the data contain 20 072 events with two muons in the final

state, most from the production and decay of charmed particles. The statistical power of such a large sample, ~50 times that of other muon experiments', allows a first measurement of differential spectra for charm muoproduction.

Chapter II describes the beam system and muon spectrometer. Chapter III describes event reconstruction, acceptance modeling, and background modeling. Extraction of the charm signal, general features of the data, and estimation of systematic errors are also discussed. Chapter IV presents results of measurements of the diffractive charm muoproduction total cross section, the Q^2 and ν dependence of charm virtual photoproduction, and the role of charm in the rise with energy of the photon-nucleon total cross section. The contribution of charm production to the scale non-invariance observed in muon-nucleon scattering at low Bjorken x is discussed. A lower limit on the ψN total cross section is presented.

CHAPTER II

THE BEAM AND THE MULTIMUON SPECTROMETER

Muons from the N1 beam line at Fermilab arrived at the south end of the muon laboratory, passed through the air gap of the Chicago Cyclotron Magnet (CCM), and entered the Multimuon Spectrometer (MMS). The trajectories of beam muons and any scattered or produced muons were registered by wire chambers placed periodically in the MMS. Data from events satisfying any of four sets of trigger requirements were recorded on magnetic tape for subsequent analysis.

The muon spectrometer was conceived as a detector for a high-luminosity muon scattering experiment studying rare processes with one or more muons in the final state. Good acceptance for both high-Q^2 scattering events and low-Q^2 multimuon events was desired. An intense muon beam incident on a long target could provide the desired luminosity while a spectrometer sensitive to muons produced at large and small angles to the beam could meet the acceptance requirements.

The detector was built in 1977 as a distributed target dipole spectrometer. Magnetized iron plates were grouped into eighteen closely spaced modules. Each module was

instrumented with wire chambers and hadron calorimetry. The spectrometer was active over its entire fiducial area, including the region traversed by the beam, allowing reconstruction of low-Q^2 multimuon events.

The beam system and individual elements of the Multimuon Spectrometer will be described below. Further details are presented in the appendices.

The muon beam

A schematic diagram of the N1 beam line is shown in Fig. 3. A primary beam of 400 GeV protons from the main ring was focused onto a 30 cm aluminum target. A series of quadrupole magnets, the quadrupole triplet train, focused the produced particles into a 400 m long decay pipe. Particles of one sign and with momentum near 215 GeV/c were bent west in enclosure 100 and were passed to enclosure 101. An east bend at enclosure 101 acted as a momentum slit and bent the beam away from its lower-energy halo. Polyethylene absorber inside the west-bending dipoles of enclosure 102 stopped hadrons in the beam. Quadrupoles in enclosure 103 refocused the beam and an east bend at enclosure 104 made the final momentum selection. The Chicago Cyclotron Magnet bent the beam east into the MMS.[20]

Figure 4 shows the locations of multi-wire proportional chambers (MWPC's) and plastic scintillation detectors used to measure the beam and reject halo muons. MWPC's and scintillator hodoscopes after the quadrupoles in enclosure 103 and at the entrance to enclosure 104 measured the horizontal positions of muons. MWPC's and scintillator hodoscopes measured horizontal and vertical coordinates at the downstream end of enclosure 104, at the entrance to the muon lab, immediately downstream of the CCM, and immediately upstream of the MMS. Halo muons were detected at three points upstream of the spectrometer. A "jaw" scintillation counter in enclosure 104 registered muons which passed through the iron of the enclosure's dipoles. A very large wall of scintillation counters downstream of the CCM also detected halo muons. A scintillator hodoscope with a hole for the beam covered the front of the muon spectrometer and counted halo particles entering the detector. A signal from any of the halo counters along the beam disabled the MMS triggers. Scintillation detectors in the beam counted incident muons and vetoed events with more than one muon in an rf bucket or with muons in the preceding or following buckets.

Data were taken with 10^{13} to 1.7×10^{13} protons/spill on the primary target. Typically 1.9×10^{6} positive muons/spill in a beam 8 inches high and 13.5 inches wide survived all vetoes. An equal number were present in the halo outside

the beam. The fraction of positive muon flux which satisfied all the veto requirements varied from 1/2 with 10^{13} protons on target to 3/8 with 1.7×10^{13} protons on target. The effective yield of positive beam muons was about 1.4×10^{-7} muons/proton. The yield of negative muons was one-third to one-half as great.

The beam energy was 215 GeV with a $\pm$2% spread. A comparison between beam energies determined by elements in the beam line and by the MMS showed that the values from the beam line were systematically 1.5 GeV greater than those from the muon spectrometer. A further check came from elastic ψ production data with three final state muons. Requiring that the beam energy equal the sum of the energies of the final state muons showed the beam system's measurement to be 2 GeV high. To maintain consistency between beam energy and final state energy, the momentum measured by the beam system was decreased during analysis by about 1.5 GeV.

The Multimuon Spectrometer

The muon spectrometer consisted of four major systems. Steel slabs served as an analyzing magnet and rectangular scintillation counters measured hadronic shower energies.

Trigger hodoscopes determined event topologies and wire chambers sampled muon trajectories. The detector is shown in Fig. 5; each of its four systems will be described below.

The magnet

The most massive component of the detector was the 475 tons of steel that served as target and analyzing magnet. The steel was rolled and flame cut into ninety-one plates, each 4 inches thick and 8 feet square. They were grouped into eighteen modules, with five slabs per module. An additional slab was placed upstream of the first detector module. The fiducial area was magnetized vertically to 19.7 kG by two coils running the length of the spectrometer through slots in the steel. The magnetic field was uniform to 3% over the central 1.4x1 m area of the slabs. It was mapped with 0.2% accuracy using flux loops. The location of the peak in the $\mu^+\mu^-$ pair mass spectrum at 3.1 GeV/c^2 from events

$$\mu N \rightarrow \mu \psi X, \quad \psi \rightarrow \mu^+\mu^-$$

provided confirmation that the field measurements were correct. The polarity of the magnet was reversed periodically. Roughly equal amounts of data were recorded with each polarity.

The magnet steel also acted as a target. The upstream single slab and slabs in the first twelve modules gave a target density for the dimuon trigger of 4.9 kg/cm^2. This corresponded to a luminosity of 500 events/pb for the data presented here. Acceptance was fairly uniform over the full target length. The average density of matter in the spectrometer was 4.7 gm/cm^3, six-tenths that of iron, allowing the magnet to act as a muon filter. Particles were required to travel through the steel of six modules, almost eighteen absorption lengths, before satisfying the $\mu\mu$ trigger. Hadronic showers developed in the steel downstream of interactions and were sampled every 10 cm by plastic-scintillator calorimeter counters.

Hadron calorimetry

Figure 6 shows a side view of a single module. Calorimeter scintillation counters 31.5 inches high by 48 inches wide were placed after each plate in the first fifteen modules. Each counter was viewed from the side by one photomultiplier tube. To achieve the large dynamic range required, signals from the tubes were amplified in two stages and the output from each stage was recorded by an analogue-to-digital converter.

Deep inelastic scattering data and ψ production data provided calorimeter calibration information. Magnetic measurements of energy lost by muons in inelastic scattering events related calorimeter pulse heights to hadronic shower sizes. The calorimeter's zero level was set with the help of ψ events which had less than 36 GeV of shower signal. By requiring agreement between the average beam energy and the average visible energy in the final state (the sum of the three muons' energies and the calorimeter signal), a zero-shower-energy pulse height was determined. The rms accuracy of the hadron calorimetry was $\Delta E=1.5E^{\frac{1}{2}}$ for ΔE and E in GeV, with a minimum uncertainty of 2.5 GeV.

Trigger hodoscopes and the dimuon trigger

Each of the spectrometer's eight trigger hodoscopes was composed of four large "paddle" counters and eight narrow "stave" counters. The arrangement of scintillator elements in a trigger bank is shown in Fig. 7. Hodoscopes were placed in the gaps following every other module, starting with the fourth. The muon experiment took data using four different triggers, run in parallel. The high-Q^2 single-muon trigger required each of three consecutive trigger banks to have no hits in any stave counter and to

have a hit in a paddle counter. The three-muon trigger required each of three consecutive banks to have hits corresponding to three particles with some vertical opening, perpendicular to the bend plane. The "straight-through" trigger required a beam muon to enter the spectrometer without passing through any of the upstream halo counters and was prescaled by typically 3×10^5. The two-muon trigger required both a shower signal from the calorimetry and a pattern of hits in three consecutive trigger hodoscopes downstream.

The dimuon calorimeter subtriggers are illustrated in Fig. 8. Calorimeter counters were ganged in overlapping clusters of ten. The first cluster included scintillators in modules one and two, the second in modules two and three, etc. giving a total of fourteen clusters. When signals from at least half the counters in a cluster exceeded a threshold level, that cluster's calorimeter subtrigger was enabled. The greater range in steel of hadronic showers enabled the calorimetry to discriminate against electromagnetic cascades. The hodoscope subtriggers required at least two counters to fire in the upstream pair of a group of three consecutive banks comprising the trigger. To reduce the rate of spurious triggers from δ-rays, the downstream bank was required to have hits in two staves with at least one empty stave between them, or hits in one paddle and any other counter, or hits in any three

counters. There were six different hodoscope subtriggers, corresponding to each combination of three successive trigger banks. Possible hit patterns satisfying a hodoscope subtrigger are shown in Fig. 9. The full dimuon trigger required both a calorimeter and a hodoscope subtrigger, with a separation along the beam direction between them. The upstream end of the earliest calorimeter cluster participating in the trigger was required to be at least seven modules from the furthest downstream trigger bank in the trigger. Table 1 lists possible calorimeter-hodoscope subtrigger combinations and Fig. 10 shows the probability of satisfying the calorimeter subtrigger as a function of shower energy. The subtrigger probability was measured when the calorimeter was calibrated. It was found by determining the fraction of the deep inelastic showers of given energy which set calorimeter subtrigger bits. The hodoscope subtrigger rate was typically 1.3×10^{-3} per beam muon while the full dimuon trigger rate was about 8×10^{-6} per beam muon.

Wire chambers

A system of nineteen multiwire proportional chambers (MWPC's) and nineteen drift chambers (DC's) measured horizontal and vertical positions of muons in the

spectrometer. An MWPC and a DC were placed upstream of the first module and in the gap following each of the eighteen detector modules. The spatial resolution of the chamber system was sufficient to allow multiple Coulomb scattering of muons in the steel magnet to limit the spectrometer's momentum resolution. The chambers were active in the beam region, greatly reducing the sensitivity of the dimuon detection efficiency to Q^2 and p_T. The wire chambers were built on aluminum jig plate, permitting them to be thin but rigid. This minimized the required widths of the inter-module gaps and maximized the average spectrometer density. The "low-Z" jig plates covered the upstream sides of the chambers and served to stop soft electron δ-rays traveling with beam muons.

The multiwire chambers had a single plane of sense wires, measuring coordinates in the horizontal (bend) plane. Signals induced on two high-voltage planes were read by center-finding circuitry shown in Fig. 11, yielding vertical and diagonal coordinates. There were 336 sense wires spaced 1/8 inch apart in each MWPC. High-voltage wires spaced 1/20 inch apart were ganged in groups of four, giving 196 diagonal channels and 178 vertical channels of information with an effective channel spacing of 1/5 inch. The proportional chambers were built on 1/2 inch jig plate and were active over an area 41.5 inches wide by 71.2 inches high. The separation between sense and high-voltage planes

was 0.4 inches. The MWPC readout electronics were gated on for 70 nsec.

The chamber resolution was approximately equal to the wire spacing divided by $\sqrt{12}$. The efficiencies of the multiwire chambers varied with position across the faces of the chambers and with chamber location along the spectrometer. Chambers near the front of the MMS had sense and induced plane efficiencies in the beam of 83% and 59% respectively while MWPC's towards the rear had sense and induced plane efficiencies in the beam of 88% and 76% respectively. Away from the beam, all proportional chambers had sense and induced plane efficiencies of 95% and 94% respectively.

Each drift chamber was built with a single sense plane of fifty-six wires measuring coordinates in the bend plane. Track finding with proportional chamber information resolved the left-right ambiguity present in single plane DC's. The drift cells were 3/4 inch wide with field shaping provided by high-voltage planes spaced 1/8 inch from the sense plane. The separation between high-voltage wires was 1/12 inch. Figure 12 illustrates the drift cell geometry and indicates the voltages applied to the field-shaping wires. The DC's were active over a 42 inch wide by 72.5 inch high area and were built on 5/8 inch aluminum jig plate.

The chamber preamplifiers read differential signals from the transmission lines formed by sense wires and the

eight closest field-shaping wires as indicated in Fig. 12. A start pulse sent from the trigger logic to the drift chamber time digitizing system enabled a 120 MHz timing clock. Signals from the chambers arriving at the digitizer within thirty-one time bins of the start pulse were latched, though most valid pulses arrived in an interval approximately twenty bins wide. The drift chamber readout was designed to latch up to four hits per channel with an average of 1/2 scaler per wire. The system has been described in detail in Ref. 21 which has been reproduced in Appendix A.

The resolution of the drift chambers was determined to be better than 250 microns by fitting muon tracks with drift chamber information. An experimental lower limit on the resolution was not determined. The theoretical resolution was 150 microns. The efficiency of the drift chambers was better than 98% in the beam.

Data acquisition

Data from the different systems were read from the experimental hardware by CAMAC whenever a trigger was satisfied. A PDP-15 received the CAMAC information and stored it on magnetic tape. On-line displays, updated after

each accelerator spill, permitted constant monitoring of the performance of the detector while the experiment was running. There were typically fifty triggers per spill; the maximum number that could be processed was about twice that. The data transfer rate of the CAMAC system and the data handling speed of the computer set the limit on event rate.

CHAPTER III

RECONSTRUCTION AND ANALYSIS

The muon experiment recorded more than 10^7 triggers on 1064 reels of computer tape. A track-finding program, TRACK, analyzed raw data, constructing muon trajectories from the wire chamber information. Taking into account multiple Coulomb scattering and energy loss, a track-fitting program, FINAL, momentum-fit muon tracks found by TRACK. A Monte Carlo program modeled the muon spectrometer, generating simulated raw data which were analyzed by TRACK and FINAL. Different physics generators permitted the Monte Carlo to describe the detector's acceptance for both charm production and background processes.

This chapter discusses event reconstruction and data analysis. The first section describes the track-finding and momentum-fitting algorithms. The second describes acceptance modeling and the third describes background simulation. The fourth discusses methods used to isolate the charm signal from the backgrounds and the fifth presents general features of the reconstructed data and Monte Carlo simulations. The sixth details methods used to estimate systematic errors.

Reconstruction

The goals of the reconstruction algorithms are conceptually simple. TRACK and FINAL attempt to determine the hadronic shower energy and the four-momenta of initial and final state muons at the interaction vertex. The implementation of these goals belies their simplicity, however. The finding program, TRACK, contains about 25,000 lines of FORTRAN and the fitting program, FINAL, even more. TRACK and FINAL analyze events of all four trigger topologies; the algorithms' reconstruction of dimuon triggers will be described below.

Track finding

Raw data from an event are unpacked and translated into wire chamber hits, calorimeter scintillator pulse heights, and latch information. A filter routine inspects patterns of hits in the trigger hodoscopes. The filter requires the hodoscope information to be consistent with all tracks intersecting at a common vertex. About 22% of the triggers, some caused by δ-rays and by stray muons entering the top or bottom of the detector, are discarded. The filter does not reject legitimate events with extra tracks.

Proportional chamber "blobs" are constructed of contiguous wire hits in each plane of the MWPC's. Since the deadtime of a drift chamber preamplifier corresponds typically to a drift distance of 2.5 mm, drift chamber "blobs" are constructed of all hits whose drift distances are within 2.5 mm of the drift distance of another hit on the same wire. MWPC hits in the planes measuring horizontal (x), vertical (y), and diagonal (u) coordinates are grouped into "triplets" or "matches" when any part of a u-plane blob is within 0.75 cm of the location expected from the pairing of a particular x blob and y blob. A blob may participate in at most three triplets; the matches are ordered by the difference between predicted and found u positions. Both triplets and blobs which are not part of a triplet are available to the routines which search for tracks.

Calorimetric information gives an estimate of the vertex position along z, the beam direction. The vertex algorithm finds the maximum calorimeter counter pulse height, A. For each slab in the detector it calculates a quantity N, where N is the difference between the number of counters with pulse height less than 0.08A and the number of counters with pulse height greater than 0.08A, for all counters upstream of that slab. The middle of the slab with the largest value of N is chosen as the vertex z position. If several slabs share the largest value of N, the center of the slab closest to the front of the detector is chosen.

TRACK uses data from the wire chambers in the beam system to project a muon track into the detector. With information from the MWPC between the first plate and the first module, an incident position and angle for the beam muon are determined. The trial trajectory is then extended downstream using a fit which is linear in y and includes energy loss and bending due to the magnetic field in x. Chamber resolution and multiple scattering determine the size of a search window at each MWPC. The triplet inside the search window which is closest to the predicted location is placed on the track. If no triplets are found, unmatched blobs are used. TRACK recalculates the muon's trajectory with the new hits and projects downstream one module. The process is continued past the vertex found by the calorimeter algorithm. After filling in the entire beam track with proportional chamber information, TRACK adds drift chamber blobs to the muon's path. The two closest blobs in each drift chamber are assigned to the track in one pass, with no refitting after the inclusion of each DC's data.

The track finder next searches for muon trajectories downstream of the vertex. TRACK begins at the back of the spectrometer and works upstream, constructing a trial track with hits from at least four MWPC's. When a track is found, drift chamber information is added simultaneously along the entire trajectory. MWPC triplets used in the track are

removed from the list of available matches, then the program begins the process again with the proportional chamber information still available.

To project a track forward from the back of the MMS, TRACK requires three triplets or two triplets and unmatched x and y hits in a third MWPC. The starting triplets may be separated by up to three proportional chambers, but there can be no more than one empty MWPC between any two chambers in the initial segment of three MWPC's. Chambers used on a track must have twelve blobs or less in the x plane. Within resolution and multiple scattering limits, the y coordinates must lie on a straight line. The curvature of the starting segment must correspond to a momentum greater than 15 GeV/c -2σ where σ is the error of the calculated momentum.

Three-chamber track segments are extrapolated past the vertex by a routine called TRACE. The actions taken by TRACE are similar to those of the beam fitting routine. The track is extended upstream one module at a time. A multiple Coulomb scattering and resolution window is opened at each chamber and a triplet or unmatched blobs are placed on the track. TRACE refits the track with the new information, including energy loss and bending in the magnetic field, and continues upstream. When a track is complete, TRACE simultaneously assigns the two best drift chamber blobs in each DC to the track and removes all used triplets from the table of available matches.

The track-hunting process continues until all possible starting segments have been investigated. Tracks are required to contain (x,y) points from at least four proportional chambers with at least two of the points from MWPC triplets. Tracks are also required to have a fit momentum of less than 325 GeV/c. The χ^2 per degree of freedom for tracks fit only with proportional chamber information must be less than 4 or 5 for x or y views respectively. Dimuon triggers with a reconstructed beam track and two or more reconstructed final-state tracks are written to secondary data tapes for analysis by the track-fitting program, FINAL.

Track fitting

FINAL assumes that tracks suffer smooth, continuous energy loss. It fits tracks by simultaneously varying the Coulomb scattering impulse in each module to minimize the χ^2 associated with the momentum fit. The algorithm calculates iteratively, rejecting information which makes a substantial contribution to the total χ^2, then performing a new fit. FINAL fits trajectories which are found by TRACK and then attempts to constrain them to a common vertex.

Figure 13 diagrams the logical flow of the fitting

routine. The initial fit to all tracks uses only MWPC information. The better drift chamber blob in each pair of blobs is then attached to the track. FINAL attempts to minimize the χ^2 of the fit and maximize the number of chambers on the track by removing hits from the track and replacing them with unattached DC blobs. Separate tracks, corresponding to a single track broken by the track finder, are fused. Halo tracks and tracks from stray muons are identified and discarded. A vertex is then chosen for dimuon triggers which possess a reconstructed beam track and at least two accepted final state tracks.

FINAL picks a trial vertex using track and calorimetric information. The z location from TRACK is used to compute and minimize the sum

$$\sum_{\substack{\text{all}\\ \text{tracks}}} \left(\frac{x_i(z_v) - x_v}{\Delta x_i}\right)^2 + \left(\frac{y_i(z_v) - y_v}{\Delta y_i}\right)^2 .$$

Here, x_V, y_V, z_V are the coordinates of the trial vertex, $x_i(z_V)$, $y_i(z_V)$ are the coordinates of the $i^{\underline{th}}$ track, and Δx_i, Δy_i are the uncertainties in the projection of the track to z_V. All tracks are refit to include the vertex. If the χ^2 of the new fit does not exceed a limit which is a function of the event's topology, FINAL searches a region extending ± 50 cm in z around z_V. The interaction vertex is chosen based on the behavior of the above sum as a function

of z. If the χ^2 of the fit which includes the vertex is large, chamber information contributing the most to the χ^2 value is discarded. FINAL then repeats the above procedure, determining a trial vertex and searching on either side of it if the new vertex fits well. If this second attempt fails, the calorimeter vertex is temporarily ignored. Tracks are returned to their original state, before MWPC and DC hits were removed. Another trial vertex is chosen, based only on track information. This vertex is used in a refit of all tracks. If too large a χ^2 results, chamber information is discarded and a new fit is made. If the fit is still poor, the event is rejected. If the trial vertex is consistent with the track information, the z position determined by the calorimeter algorithm is included in a new fit. If the calorimeter vertex z coordinate is not consistent with the track vertex, the calorimetric information is rejected and tracks are fit with only the track-determined vertex. If the calorimeter vertex agrees with the track vertex, a fit is done which includes the shower information. Once FINAL selects a vertex for an event, the fitting for that event is finished.

FINAL uses an impulse approxmation to describe the bending of muon paths in the spectrometer. Each module imparts a transverse momentum of 299 MeV/c. The fitting program assumes an impulse is applied between successive chamber hits at one point whose z position is chosen to give

the correct angular and spatial displacement for a muon traveling through the iron magnet. Since FINAL fits tracks assuming a smooth, continuous energy loss, the z position of the impulse is generally not midway between the front of the first plate and back of the fifth plate in a module. FINAL's estimate for the amount of energy lost by a particle is a function of energy and path length in matter.

Multiple Coulomb scattering of particles is also described in the impulse approximation. FINAL simultaneously varies the transverse impulse in x and y in each module to determine a best fit to a trajectory.

The track fitting program corrects the beam energy as described in the previous chapter. The correction is applied to blocks of data, each containing about 5% of the full data sample. All events in a block have the same sign of beam muon and magnet polarity. The hadron calorimeter is calibrated separately for each data block as described previously. FINAL uses the appropriate set of calibration constants for each event.

A series of cuts, to be described later, are applied to reconstructed events to discard data taken in kinematic regions where the spectrometer's acceptance changes rapidly. Before these cuts are made, 91% of the successfully analyzed events have tracks which reconstruct to satisfy the dimuon trigger. After the cuts, 98% of the events meet this requirement. Because of this, no attempt is made to require

analyzed events to satisfy the μμ trigger after reconstruction.

To compute kinematic variables such as Q^2 and ν, the analysis programs must decide which final state muon is the scattered muon and which is the produced muon. The choice is obvious when the muons downstream of the interaction have opposite charges-- the scattered, or "spectator" muon is the particle with the same charge as the beam muon. If both muons have the same sign as the beam, the more energetic μ is chosen as the spectator. When applied to opposite sign pairs, this algorithm is successful 91% of the time.

The error in vertex placement varies from 15 cm to several meters. It depends in part on the opening angle of the final state muon trajectories and the "cleanliness" of the calorimeter information. The rms momentum resolution is about 8% and varies approximately as the square root of the length of tracks in the spectrometer.

TRACK is able to reconstruct 39% of the exclusive dimuon triggers, where "exclusive" refers to events which satisfy only one trigger. Most rejected events emerge from the track finder with fewer than two final state tracks. FINAL successfully analyzes 37% of its input from TRACK. Most failed dimuon triggers do not survive FINAL's attempts to construct a vertex. These events largely are caused by noise such as shower activity in the detector and do not reconstruct to have two muons in the final state.

Acceptance modeling

A Monte Carlo simulation of the spectrometer is used to unfold detector acceptance from measured distributions. The Monte Carlo also allows an extrapolation of measured distributions into kinematic regions outside the acceptance of the detector. By using the calculation to estimate the ratio of observed to unseen events, total cross sections may be determined. To be successful, the simulation must accurately model the geometry and sensitivity of the spectrometer and must include effects such as energy loss and multiple scattering of muons. An acceptable model of the underlying physics governing interactions is needed to properly describe acceptance and to allow extrapolation outside the measured kinematic region.

The Monte Carlo simulation of the Multimuon Spectrometer consists of two parts, a shell and a physics generator. The shell describes the detector, propagates particles through the spectrometer, and writes simulated data tapes when an imaginary interaction satisfies an event trigger. The physics generator contains the model for the process being studied and produces daughter particles and hadronic showers with distributions intended to mimic actual interactions. Generators for charm production, deep inelastic scattering, vector-meson production, and π, K

production are among the routines that have been used with the Monte Carlo shell.

The shell uses randomly sampled beam muons recorded as straight-through triggers during the course of the experiment. The program propagates beam muons from the front of the spectrometer to interaction vertices, causing the muons to suffer energy loss from effects such as μ-e collisions, muon bremsstrahlung, and direct electron pair production. Simulated muon trajectories are bent by the magnetic field and are deflected by single and multiple Coulomb scattering processes. A nuclear form factor is used in the description of large-angle scatters. Daughter muons bend, lose energy, and multiple scatter in the same way. One of the physics generators creates charged π and K mesons and allows them to decay after traveling through typically half a module. The Monte Carlo causes the mesons to lose energy, multiple Coulomb scatter, and bend in the magnetic field during their brief existence. All muons are traced through the spectrometer until they leave the detector or stop. Interactions which satisfy any of the experimental triggers are encoded and written to tape with the same format as was used to record real events.

The shell assumes that the efficiency of the drift chambers is 100% and the efficiency of the MWPC's is less, as described earlier. Wire chamber hits are generated to represent particles traveling through the MMS and showers

developing downstream of an interaction. Halo muons, δ-rays, and out-of-time beam particles are not simulated. Only a minimal attempt is made to model the spreading of hadronic showers through the chambers.

A photon-gluon-fusion (γGF) model for charmed quark production, described in chapter I, serves as the heart of the physics generator used to study detector acceptance for charm. In γGF, the cross section to produce a charmed quark and its antiquark with a virtual photon is

$$\sigma_T = 4\pi^2\alpha\, W_1\, (\nu^2+Q^2)^{-1/2}$$

for transversely polarized photons and

$$\sigma_L = 4\pi^2\alpha\, W_2\, (\nu^2+Q^2)^{+1/2}/Q^2 \;-\; \sigma_T$$

for longitudinally polarized photons.[22] Here,

$$W_1 = \frac{4}{9\pi M}\int_{x_0}^{1} dx\, \alpha_s\, \frac{G(x)}{x}\, \delta^2 \left\{ \left(\frac{m^4}{4} + m^2m_c^2 - 2m_c^4 + \frac{Q^4}{4}\right) \ln\left[\frac{m^2+\lambda}{m^2-\lambda}\right] - \lambda\left(m_c^2 + \tfrac{1}{4}(m^2-Q^2)/m^2\right)\right\}$$

and

$$W_2 = \frac{4M}{9\pi}\int_{x_0}^{1} dx\, \alpha_s\, G(x)\, x\delta \left\{ \lambda\left[9\delta - \frac{1}{m^2} - 4(4m^2+m_c^2)\delta^2 + 4m^2(2m^2+m_c^2)\delta^3\right] + \ln\left[\frac{m^2+\lambda}{m^2-\lambda}\right]\left[1 - (3m^2+8m_c^2)\delta + 4(m^4+5m^2m_c^2-2m_c^4)\delta^2 - 2m^2(m^4+6m^2m_c^2-4m_c^4)\delta^3\right]\right\}$$

where

$$m^2 = 2M\nu x - Q^2 \qquad \lambda^2 = m^4 - 4m^2 m_c^2$$

$$\delta = (m^2 + Q^2)^{-1} \qquad x_0 = (4m_D^2 + Q^2)/(2M\nu)$$

$$\alpha_s = 12\pi/[25\ln(4m^2)] \qquad G(x) = 3(1-x)^5/x \ .$$

The connection between muoproduction and virtual photoproduction will be discussed in chapter IV.

Charmed quark pairs are produced quasi-elastically in γGF; that is, the $c\bar{c}$ pair carries off most of the energy of the virtual photon. To allow the model to make quantitative predictions, the charmed quark mass, m_c, is set to 1.5 GeV/c^2.[22] The distribution for the gluon momentum fraction x_g is taken to be $3(1-x_g)^5/x_g$. Here, x_g is $(Q^2 + m_{c\bar{c}}^2)/(2M\nu)$. The strong coupling constant α_s is $1.5/\ln(4m_{c\bar{c}}^2) = 3/8$. Figure 14 shows the $m_{c\bar{c}}$ pair mass spectrum that results; the average pair mass is 4.9 GeV/c^2. Only those events with $m_{c\bar{c}} > 2m_D$ are allowed to generate final states containing open charm.

One-tenth of the beam muons which produce charm interact coherently with iron nuclei while the rest interact incoherently with nucleons in Fermi motion. The γGF model does not describe the -t dependence of the production cross section, where -t is the square of the four-momentum transferred to the target. Coherence, screening, and -t dependence are parametrized in a fashion identical to that

used to describe ψ production[23] through

$$\frac{d\sigma}{dt}(\gamma Fe \to c\bar{c}X) = \left[A_e^2 e^{150t} + A_e\left(\frac{7}{8} e^{3t} + \frac{1}{8} e^{t} \right) \right] \frac{d\sigma}{dt} (\gamma N \to c\bar{c}X)\Big|_{t=0} .$$

The effective atomic number, A_e, is taken to be 0.9 times 55.85 based on measurements of screening from SLAC.[24] The coherent slope is unresolved in our ψ data and is based on lower energy photon-nucleon measurements.[25]

A prescription to describe the fragmentation of quarks into hadrons, and the semi-leptonic decay of those hadrons, is necessary to connect the γGF predictions with experimentally observable results. The Monte Carlo uses a two-stage fragmentation to turn the charmed quarks into hadrons. The first describes the escape of the $c\bar{c}$ pair from the vicinity of the target nucleon. In the spirit of γGF, the pair moves away from the production vertex with minimal interference from the target. The exchange of soft gluons to "bleach" the color from the quark pair is ignored. The $c\bar{c}$ system absorbs the maximum allowable amount of energy from the virtual photon. The second stage describes the fragmentation of the $c\bar{c}$ into D mesons. A function $D(z) = (1-z)^{0.6}$ parametrizes the breakup, where E_D^* is the energy of a charmed particle in the $c\bar{c}$ center of mass and $z = 2E_D^* / m_{c\bar{c}}$ represents the fraction of the maximum possible energy the meson receives. D(z) is based on SPEAR data[26] taken at center of mass energies comparable to typical

values of $m_{c\bar{c}}$ in the γGF model. The SPEAR data measure inclusive D production and therefore include information on D* production with the subsequent decay $D^* \rightarrow DX$.

The Monte Carlo allows the charmed quarks to fragment into neutral and charged D's in a 2:1 ratio.[26] The ratio is based on the same SPEAR measurements which yielded the function D(z). Other charmed states such as $F\bar{F}$ and $\Lambda_c\bar{\Lambda}_c$ are not explicitly simulated. Any difficulties caused by limiting the variety of particles produced by the $c\bar{c}$ pair are present only to the extent that the unmodeled states decay with characteristics different from those of a $D\bar{D}$ state. The average values of Q, the available kinetic energy in typical semileptonic decays of F's and Λ_c's, differ by $\sim$10% from the average Q in the simulated decay modes. This results in different $p_{\parallel}$ and p_T spectra for the different decay modes where $p_{\parallel}$ and p_T are muon momentum components parallel and perpendicular to the virtual photon. Monte Carlo calculations indicate that acceptance is much more sensitive to $p_{\parallel}$ than p_T. The data and Monte Carlo agree to 15% in p_T; studies of systematic uncertainties, described below, include investigation of the sensitivity of our measurements to $p_{\parallel}$ spectra.

The simulation assumes the branching ratios of 4% and 20% for $(D^0\bar{D}^0)$ and $(D^+D^-) \rightarrow \nu\mu X$ respectively.[27,28] X is taken to be K*(892) 39% of the time and K 61% of the time.[28] The net yield of muons per $c\bar{c}$ pair is 0.187 with the above

assumptions. To permit proper modeling of the shower energy and missing (neutrino) energy, D's are allowed to decay to evX with the same branching fractions.

The Monte Carlo was used to generate a data set of simulated events representing a beam flux equivalent to that producing the real data reported here. In all, 2.87×10^{9} incoherent and 3.30×10^{6} coherent Monte Carlo interactions produced 4.49×10^{6} and 8.4×10^{3} triggers, respectively. The trigger efficiency for ΥGF events with decay muons is therefore 16.7%. Including the muonic branching ratios indicated above gives a net trigger efficiency of 2.87%.

Figure 15 shows the Q^2 distributions for events which were generated by the charm model and which satisfied the simulated trigger. The spectrometer's acceptance is remarkably flat in Q^2 due to its "no-hole" construction and forward sensitivity. This is evident in the minimal difference in the shapes of the generated and triggered spectra. Figure 16 shows shower energy distributions. The different shapes of the generated and triggered plots are caused to great extent by the calorimeter subtrigger. Spectra of daughter muon energies are shown in Fig. 17. Since daughter muons must travel through at least six modules to satisfy the dimuon trigger, the detector's acceptance for slow muons is small. The energy loss per module experienced by a muon is about 1 GeV and the transverse momentum imparted by the magnetic field is about

300 MeV/c. Soft muons are stopped or slowed and pitched out of the spectrometer before they can trigger the apparatus. Distributions in ν are shown in Fig. 18. Acceptance as a function of ν, the energy lost by the beam muon, is influenced strongly by the shower requirement and the daughter-energy acceptance. For values of ν close to the beam energy, the requirement that the scattered muon travel through more than six modules has a strong effect.

The data presented in figures 15-18 include both same-sign and opposite-sign final state muon pairs. Since beam muons are bent partially out of the spectrometer while traveling to the interaction vertex, daughter muons with the opposite sign are bent back into the MMS. Consequently, after reconstruction, the acceptance for opposite-sign pairs is higher by a factor of 1.45. After analysis cuts described below, the factor decreases to 1.26.

The comparison between data and Monte Carlo samples will be discussed later.

Background modeling

The experiment identifies charmed states by their decays into a muon and at least two other particles. Since decays such as $D \to K\pi$ contribute only to the calorimeter

signal, none of the kinematic distributions can exhibit an invariant-mass peak representing charm production. To allow extraction of the charm signal, important sources of contamination must be modeled and subtracted from the data. If the spectrometer had measured two-body decays which yield mass peaks for charm, the experimental data would provide all the necessary background information. A smooth curve could be extrapolated under the mass peak, allowing accurate determination of signal-to-background ratios. Since this is not the case, a Monte Carlo simulation of the major background is used to remove non-charm contamination from the data.

The largest source of background is the decay-in-flight of π and K mesons produced in inelastic muon-nucleon collisions. Other sources of contamination are muon trident production $\mu N \rightarrow \mu \mu^+ \mu^- X$, τ pair production $\mu N \rightarrow \mu \tau^+ \tau^- X$ with $\tau \rightarrow \mu X$, and bottom meson production $\mu N \rightarrow \mu B \bar{B} X$ with B or $\bar{B} \rightarrow \mu X$.

π, K decay

The average density of the Multimuon Spectrometer is 4.7 gm/cm^3, six-tenths that of iron. Because of this, most π and K mesons produced in a hadronic shower interact and

stop in the detector before decaying. The probability for a π or K with energy γmc^2 to decay in flight is $L/(\gamma c\tau)$ where L is the particle's absorption length and τ is its mean proper lifetime. For a 20 GeV π in the MMS the total decay probability is about 4×10^{-4}, while for a 20 GeV K^+ it is 4×10^{-3}. This indicates that perhaps a tenth of a percent of the inelastic muon-nucleon collisions in the spectrometer will give rise to a shower-decay muon. Since theoretical estimates predict charm muoproduction cross sections that are a percent or less of the total inelastic cross section, accurate simulation of the π, K decay background is necessary.

A shower Monte Carlo based only on experimental data measuring muon-nucleon and hadron-nucleon interactions is used to study the π, K-decay background. Parametrizations of muon-nucleon scattering[20] and hadron muoproduction[29,30] cross sections from the Chicago-Harvard-Illinois-Oxford collaboration (CHIO) fix the Monte Carlo's absolute normalization. Bubble chamber data are used to describe the interactions of pions and kaons with target nuclei[31-46] as the shower develops in the detector. The simulation creates a full shower until all charged particles have energies less than 5 GeV. Once the hadronic cascade has been generated, the Monte Carlo chooses which, if any, of the shower mesons to let decay.

The physics generator for the π, K Monte Carlo is used

with the standard MMS shell described earlier. The shell manipulates beam information, generates simulated raw data, propagates muons, etc. The propagation routine allows π's and K's to travel through the spectrometer for the distance requested by the generator. Mesons lose energy, multiple Coulomb scatter, and bend in the magnetic field. Inelastic μN scattering vertices are chosen to reflect the fine structure of the detector. Since mesons in showers beginning near gaps between modules are more likely to decay, the vertex distribution shown in Fig. 19 results.

Once a vertex is selected, the simulation picks values for Q^2 and ν based on CHIO information. Values of Q^2 range from the minimum to the maximum kinematically allowed while ν runs from 10 GeV to the beam energy. The CHIO data are corrected to describe an isoscalar target[47] and renormalized by a factor of 0.9 to allow for nuclear screening.[24] To the desired accuracy, iron is well approximated as an isoscalar nucleus. The program keeps track of the cross section for scattering with $\nu > 10$ Gev to fix the probability of generating showers.

CHIO data describe positive and negative hadron production by 147 GeV and 219 GeV muons. CHIO parametrize their results in terms of Feynman x (x_F) and hadron momentum perpendicular to the virtual photon, p_T. Feynman x is defined as

$$x_F = \frac{P_{\parallel}^*}{\left(P_{max}^{*2} - P_T^2\right)^{1/2}} \approx \frac{2P_{\parallel}^*}{S^{1/2}} .$$

Here, $p_{\parallel}^{*}$ is the momentum of a hadron parallel to the virtual photon in the center-of-mass (CM) of the photon-nucleon system and p_{max}^{*} is the maximum momentum it can have in the CM. The total CM energy is $\sqrt{s}$. The Monte Carlo uses CHIO distributions which are averaged over Q^2 ($Q^2 > 0.3$ (GeV/c)^2) and ν ($\nu > 53$ GeV) for muon-deuteron scattering. It is assumed that the x_F and p_T distributions provide an adequate description of the region with $Q^2 < 0.3$ (GeV/c)^2 and $\nu < 53$ GeV. It is also assumed that the distributions depend weakly on ν and Q^2.

Reference 30 presents K/π ratios for the CHIO 219 GeV data. Based on these data, the simulation uses a K^+/π^+ ratio of $0.13 + 0.13p_T^2$ and a K^-/π^- ratio of $0.1 + 0.12p_T^2$. Here p_T is in GeV/c.

Neutral particles are treated in an approximate fashion by the Monte Carlo. Distributions for π^0 production are taken as an average of the π^+ and π^- distributions. A photon from π^0 decay produces muons and electrons in the ratio[48] $m_e^2/m_\mu^2 \approx 2.4\times10^{-5}$. Since a π^0 decays into two photons and each photon almost always produces a pair of particles, the average yield of muons per π^0 is 9.6×10^{-5}, less than the decay probability for a charged meson. The simulation thus assumes that neutral pions just remove energy from the shower and do not produce muons. Shower studies from another experiment indicate that this is a reasonable approximation.[49] Neutral kaons are made with the

same distributions as their charged counterparts. Half of the neutral K's are K_S's which decay quickly to two pions while the rest are K_L's which are long-lived. Therefore, half the time K^o's are used as energy sinks which do not yield muons and half the time their energy is returned to the pool available for charged meson production.

Charged and neutral mesons in the primary shower, the initial virtual photon-nucleon interaction, are generated with CHIO distributions in the range $0 < x_F < 1$. Approximate energy conservation is imposed by requiring $\sum x_F < 1$ where the sum runs over all particles generated. Primary showers violating this requirement are discarded and regenerated.

The Monte Carlo's description of primary showers neglects the dependence of kinematic distributions and charge multiplicities on atomic number A. The muon spectrometer's acceptance is appreciable only for shower-induced muons whose parent mesons had $x_F > 0.2$. In this region, distributions and multiplicities show negligible A dependence.[50] The simulation also neglects muons arising from ρ, ω, ϕ production with muonic decay of these particles.[49]

The program uses information stacks as bookkeeping aids while generating hadronic cascades. An "interaction" stack keeps track of all mesons with more than 5 GeV of energy which have not yet been made to interact in the detector to

produce secondary showers. A "history" stack records the structure of the developing shower, storing information on parentage, p_T with respect to the parent meson, etc. for each meson generated with energy greater than 5 GeV. Pions and kaons in the primary shower are loaded into the interaction and history stacks. Secondary showers result from interactions of mesons with nucleons in the spectrometer, which yield more particles. They are generated by removing a π or K from the bottom of the interaction stack, "colliding" it to produce more hadrons, and adding all new particles with sufficient energy to the bottom of the two stacks. The process is repeated until the interaction stack is empty, leaving the history stack with a complete description of the hadronic cascade.

The Monte Carlo generates an individual secondary shower in several steps. It first chooses the propagation distance that a π or K travels before interacting. Absorption lengths for mesons in iron are determined by scaling the proton absorption length at 20 GeV[51] by the ratio of the proton-deuteron and meson-deuteron total cross sections.[41-44] The $\pi^{\pm}$ absorption length is 26.8 cm or (28.3 - 30/E) cm for particles with energy greater than or less than 20 GeV, respectively. The K^+ absorption length is 36.1 cm and the K^- absorption length is 30.1 cm, independent of energy. The distance a meson travels is a function of its absorption length and its initial position in a module.

Particles produced near the back of a module have a greater chance of reaching the gap between modules.

The shower generator decreases the meson's energy by the average amount it is expected to lose traveling through the spectrometer to its interaction point. The following inelastic collisions are simulated:

$$\pi^{\pm} N \rightarrow n_1\pi^{\pm} + n_2\pi^{\mp} + n_3\pi^{0} + X$$

$$K^{\pm} N \rightarrow n_1 K^{\pm} + n_2\pi^{\pm} + n_3\pi^{\mp} + n_4\pi^{0} + X$$

The coefficients n_1-n_4 are greater than or equal to zero. These interactions are completely described by specifying the particle multiplicity, x_F, and p_T distributions. Charged multiplicities are taken from the bubble chamber data of Refs. 33-36. Multiplicities are reduced by one unit to remove the target proton from the bubble chamber distributions. The data of Ref. 34 are then used to obtain the $x_F > 0$ multiplicities from the corrected $-1 < x_F < 1$ multiplicities of the cited references. These forward multiplicities provide an absolute normalization for the momentum distributions used to generate secondary hadrons. References 31, 32, 34, and 37 provide the Feynman x and p_T information which describes charged particle production. Neutral pions are produced with distributions corresponding to those for the pion with opposite charge from the parent particle.

Secondary mesons with $x_F > 0$ are generated. As before,

approximate energy conservation is imposed by requiring $\sum x_F < 1$. After successful creation of a secondary shower, all π's and K's with more than 5 GeV of energy are loaded into the two stacks.

The Monte Carlo neglects A dependence of secondary multiplicities and momentum distributions. The data of Ref. 45 indicate that the atomic number dependence is important in the target fragmentation region, $x_F < 0$, and is negligible in the forward, positive x_F region.

The simulation does not model associated production in reactions such as $\pi N \rightarrow K\Lambda$.

The entire cascade is generated before the Monte Carlo chooses which particle will decay. If the probability of decay for a typical shower meson were large, this method would overpopulate the final generations of a shower. Early decays in the shower would deplete the hadron population available to produce more mesons in secondary cascades. Since the probability for a 120 GeV shower to produce a decay muon is about 10^{-3}, creating the full cascade while initially neglecting decays is a sufficiently accurate approximation. The Monte Carlo allows at most one meson to decay. A hadron with at least 5 GeV of energy is chosen based on a probability which is a function of absorption length, energy, and place of creation in the MMS. The probability that a particle will decay after traveling a given distance is proportional to the probability that it

neither decayed nor interacted before getting that far. Since it is much more likely for a π or K to interact than to decay, the simulation chooses the length of the hadron's flight path according to the probability that it traveled that distance before interacting. Figure 20 shows a plot of the distance between creation and decay for chosen shower mesons.

Pions decay to $\mu\nu$ with 100% probability and kaons to $\mu\nu$ with 63.5% probability. The 3.2% $K\rightarrow\mu\nu\pi$ decay mode is neglected. The laboratory frame energy of the neutrino is calculated to obtain the correct balance of shower energy, daughter energy, and missing energy. Once a decay meson is chosen, the shower generator returns program control to the Monte Carlo shell. The shell propagates through the detector all the mesons in the parent-daughter chain which terminates in a decay, calculates the Lorentz transformations needed to produce the resulting muon, and propagates the muon through the rest of the detector. Events which satisfy an event trigger are recorded on tape.

The total cross section for muon production via π, K-decay is a convolution of the inelastic scattering cross section with the probability that a decay muon comes from the hadron cascade. The average beam energy at the interaction vertex is 209 GeV. With that energy and the beam's observed momentum spread, the inelastic cross section to scatter with $\nu > 10$ GeV is 3.54μb. The cross section to

scatter and produce a decay muon with energy greater than 5 GeV is 2.28 nb. The combined trigger and reconstruction efficiency for these events is 4.6%. Figure 21 shows the probability vs. ν for a shower to produce a muon with energy greater than 9 GeV. The absolute normalization of the Monte Carlo predicts that after reconstruction but before analysis cuts, 43% of the dimuon signal is from π, K decay. After the analysis cuts described below, the decay contamination drops to 19%.

The Monte Carlo was used to generate a data sample corresponding to 1/3.915 times the beam flux represented by the data to be discussed. All π, K-decay distributions and their errors are scaled by 3.915 to compare data with Monte Carlo.

Figures 22-35 show predictions of the shower Monte Carlo. The charged multiplicity for mesons with more than 5 GeV of energy is shown in Fig. 22. The number of meson generations linking the virtual photon-nucleon interaction and the decay muon is shown in Fig. 23. Though 22% of the muons come from parent particles created in meson-nucleon showers, after reconstruction and cuts this decreases to 10%. Figure 24 shows the decay probability for generated shower mesons. The two peaks correspond to π's and K's. The ratio of K's to π's decaying in flight is 0.69 for K^+/π^+ and 0.46 for K^-/π^-. The ratio of π^+ to π^- is 0.92. This unusual charge ratio accurately

reflects the production ratio of 0.91 measured by CHIO. After reconstruction and analysis cuts, the ratios are 0.81 for K^+/π^+, 0.59 for K^-/π^-, and 0.81 for π^+/π^-. The increase in K/π fractions presumably results from the difference in acceptance caused by the greater available p_T in K decay. The change in the π^+/π^- ratio is caused by the larger acceptance for daughter muons charged opposite to the beam since most data were taken with positive beam muons. Figures 25 and 26 show ν and Q^2 for simulated inelastic muon-scattering events. Figures 27 and 28 show the x_F and p_T^2 distributions for π's and K's with more than 5 GeV of energy in the primary shower. Distributions in x_F and p_T^2 for all secondary mesons before the $\sum x_F$ requirement is imposed are shown in figures 29 and 30. The approximate energy conservation requirement rejects 14% of the generated secondary showers. Figure 31 shows the energy of hadrons allowed to decay and Fig. 32 shows the decay muon momentum along the z axis. The muon energy for events satisfying the simulated dimuon trigger is shown in Fig. 33. Figure 34 illustrates the momentum component perpendicular to the virtual photon for the muon at the decay point in events satisfying a trigger. The neutrino energy for π, K-decay triggers is shown in Fig. 35.

It is important to have confirmation that the predictions of the shower Monte Carlo are reasonable. Since most reconstructed π, K events have a muon from the decay of

a primary shower meson, data in agreement with the CHIO results would provide this check. Unfortunately, all other experiments studying hadron production by charged leptons have used lower energy beams.[52] The only possible tests of the simulation are indirect.

One check compares the missing (neutrino) energy predicted for π, K events with that observed in the data. The meson momentum spectrum is sharply peaked at low momentum. This is caused by the approximate $\exp(-3.5x_F)$ Feynman x spectrum exhibited by primary mesons[29] combined with the $(1-x_F)^4$ shape[34] which describes secondary production. Since the spectrometer's acceptance for slow muons is small, decay muons produced in the forward direction are strongly favored. A forward decay muon is accompanied by a neutrino with very little energy in the laboratory. The γGF charm model suggests that charmed quarks tend to receive half of the virtual photon's energy. Though fragmentation and decay kinematics exert a strong influence on muon energies, the parent distribution of quark momenta is not sharply peaked at low momentum. Charmed particles tend to have more energy in the laboratory than shower mesons so observed muons from charm can be produced in a wider angular range. As a result, charm events should show significantly greater missing energy. This is found to be true; the comparison between data and Monte Carlo missing energies will be discussed below.

Another effect influences the missing energy distributions for π, K and charm events. The probability for a π or K to decay in flight is proportional to 1/E where E is the meson's energy, while the probability for a charmed particle to decay promptly is independent of energy. This 1/E dependence favors slow π's and K's with a forward decay muon over faster shower mesons with more decay phase space in the acceptance of the MMS.

The results of the shower Monte carlo are consistent with the rates predicted by a Monte Carlo used by the Caltech-Fermilab-Rockefeller (CFR) neutrino experiment.[53] The CFR program uses a model by Feynman and Field[54] to generate a neutrino-induced primary shower. Data taken by CFR with incident pions are used to parametrize secondary interactions of shower mesons. The CFR Monte Carlo predicts muon yields equal to those predicted by my shower simulation for 75 GeV showers, 10% higher for 100 GeV showers, 15% higher for 125 GeV showers, and 25% higher for 150 GeV showers. The average shower energy in this experiment is 87 GeV.

Muon tridents, τ pairs, bottom mesons

Other sources of background to the charm signal include muon tridents, τ pairs with muonic decay of one τ, and bottom meson pairs with muonic decay of one or both mesons. Each has been investigated and will be described.

Barger, Keung, and Phillips (BKP) have studied the contribution of electromagnetic muon tridents to the multimuon signal which might be seen by a muon experiment.[55] They wrote a computer program which generates trident events through the three processes shown in Fig. 36. Since most tridents are not accompanied by significant shower activity, the BKP calculation predicts a small contribution to the dimuon trigger rate. Events which satisfy the trigger and are reconstructed as two-muon events should contaminate the data at the level of 1/2%. The trimuon final state trigger rate predicted by the BKP generator, when patched into a crude simulation of the MMS, provides a consistency check of the dimuon information. This check confirms that electromagnetic tridents are a small background to charm production.

Another upper limit on the trident background comes from the study of events with three muons in the final state which satisfied the dimuon trigger. This test checks the consistency of the data with the hypothesis that all the

dimuon triggers with three reconstructed final state tracks result from charm production followed by the muonic decay of both charmed particles. The production process and charm decay kinematics are assumed to be described by the γGF model discussed earlier. The charm Monte Carlo is normalized so that it predicts the same number of dimuon events after reconstruction and cuts as are present in the data after subtraction of the expected π, K-decay background. All data events and γGF events which satisfy the dimuon trigger with three reconstructed tracks are subjected again to analysis cuts after the analysis is blinded to the softest final state track. After cuts, 720 data events and 706 Monte Carlo events remain. Including statistical errors, the Monte Carlo accounts for (98 $\pm$ 5)% of the data. This suggests that most 2μ events which result from partial reconstruction of 3μ final states come from charm systems, not muon tridents. Less than one-fifth of the simulated dimuon triggers are caused by 3μ charm events. Consequently, other sources of 3μ events which feed down to the 2μ sample should account for a negligible fraction of the data. We conclude that the dimuon background from partially reconstructed muon tridents is small and neglect it.

τ leptons can decay into hadrons and neutrinos. A τ pair can therefore satisfy the dimuon full trigger through decay combinations like $\tau^+ \to \pi^+ \bar{\nu}_\tau$, $\tau^- \to \mu^- \bar{\nu}_\mu \nu_\tau$. The

reduction in the trigger rate from muon tridents provided by the calorimeter subtrigger therefore does not apply to τ-pair events. Fortunately, the kinematics of lepton production reduces the cross section for τ production by a factor of $(m_\mu/m_\tau)^2 = 3.4\times10^{-3}$ relative to trident production.[48] Including the 17.5% $\tau\to\mu\nu\bar{\nu}$ branching ratio gives an extra factor of .289 so the net ratio of τ production with a single decay muon to trident production is approximately 10^{-3}. The calorimeter subtrigger reduces the dimuon trigger rate only by a factor of 160, so the τ background should be about 0.1%, even less than the trident background. The masses of the τ and D are nearly equal. Replacing the $c\bar{c}$ by a $\tau^+\tau^-$ and the gluon by a photon in Fig. 2(c) allows a comparison of the charm and τ cross sections. The ratio is approximately $(\alpha/\alpha_s)^2$ or 10^{-3}, consistent with the above estimate. Consequently, the background from τ pairs is neglected.

The VGF model predicts a bottom meson production cross section which is less than 0.03% of the charm cross section.[55] Bottom pairs should be seen as dimuon events and as events forming exotic charge combinations like $\mu^+N\to\mu^+\mu^-\mu^-$ X from cascade decays through charm. The small number of exotic events and events with four or five muons in the final state proves that bottom production is not a significant background to charm production. Our 90%-confidence upper limit on the cross section for Υ

production[56] confirms this conclusion. Even if the bottom production cross section times muonic branching ratio were 100 times that for Υ's, $B\bar{B}$ states would comprise less than 5% of the data.

Extracting charm from the data

Raw data and simulated raw data from the γGF and π, K-decay Monte Carlo simulations are analyzed in an identical fashion. Histograms for data and Monte Carlo are generated with the same reconstruction and analysis cuts. After the π, K histograms are scaled by 3.915 they are subtracted bin-by-bin from the data histograms, yielding distributions for charm. Statistical errors quoted for charm spectra include the error on the subtraction. Systematic errors associated with this procedure will be discussed below.

Cuts applied to data and Monte Carlo events serve several purposes. Events whose reconstruction is dubious can be discarded. Data in kinematic regions where the detector's acceptance changes rapidly or is poorly understood can be rejected. Cuts which favor charm over π, K decay can improve the data's signal-to-background ratio.

A number of cuts are used to select events which are well reconstructed. The vertex selection is checked by

requiring the difference between the z position of FINAL's vertex and the calorimeter algorithm's vertex to be greater than -60 cm and less than +65 cm. The incident energy of the beam muon must lie between 206 GeV and 226 GeV. The χ^2 for the fit to the beam track must be less than 10 for four degrees of freedom in the horizontal view and less than 7.5 for three degrees of freedom in the vertical view. An aperture cut passes events whose beam muons did not enter the iron of the enclosure 104 dipoles. Events must have exactly two reconstructed final-state tracks. Each track must have horizontal and vertical χ^2 fits with less than 4.5 and 3.5 per degree of freedom, respectively. The number of degrees of freedom for tracks in the MMS depends on the length of the tracks. Data which satisfy only the dimuon, and not the trimuon, trigger are passed. Reconstructed tracks are projected upstream to the vertex and downstream until they leave the MMS. These "extended" tracks must be missing no more than four MWPC hits between the hit furthest downstream on the track and the point where the extended track leaves the detector. There must be no more than six missing chamber hits between the vertex and the hit furthest upstream on the track. To reject events associated with a shower entering the front of the spectrometer, the MWPC upstream of the first module must contain fewer than ten hits. Reconstructed tracks must differ sufficiently in curvature and direction to represent distinct muon

trajectories. Two requirements discard events in which a stale track has been interpreted as the trajectory of a produced muon. The difference between the z momentum of the beam and the sum of the z momenta of final state tracks must be greater than -18 GeV/c. The ratio of the energy lost by the beam muon to the energy observed in the final state (the sum of the muon energies and the shower energy) must be greater than 0.6.

Several analysis cuts exclude data from kinematic regions where the spectrometer's acceptance changes rapidly or changes in a way which is poorly modeled. Reconstructed tracks are required to have at least 15 GeV/c of momentum. Events are required to have more than 36.5 GeV of shower energy. Reconstructed vertices must lie between the centers of the first and eighth modules. To increase the signal-to-background ratio, daughter muons are required to have at least 0.45 GeV/c momentum perpendicular to the scattered muon. In addition, the beam muon is required to lose at least 75 GeV of energy.

The dimuon sample shrinks from 82 026 events after reconstruction cuts to 20 072 events after both reconstruction and analysis cuts are applied. The π, K-decay background drops from 43% of the data to 19% of the data. Qualitative features of the data and further justification for some of the analysis cuts will be discussed in the next section.

General features of the data

Figures 37-43 show distributions for the two Monte Carlos and data after subtraction of the π, K-decay background. Events in the histograms survived reconstruction and cuts; acceptance has not been unfolded.

Events in Fig. 37 pass all the analysis cuts except that no daughter energy requirement is made and all events are required to have $\nu > 150$ GeV. The unusual ν cut increases the sensitivity of the predictions of the Monte Carlo simulation to assumptions about charmed quark fragmentation. The inverted histogram represents the π, K Monte Carlo, absolutely normalized to the beam flux and scaled as described earlier. The upright histogram represents data after subtraction of the π, K histogram. The smooth curve shows the prediction of the νGF model, normalized to the data after the standard analysis cuts are applied. The horizontal bar indicates the rms resolution at 30 GeV. Figure 37 makes clear the need for a daughter energy cut. Though both Monte Carlo samples, and presumably the data, heavily populate the region of low daughter energy, the detector's acceptance is too small to allow reconstruction of many of these events. All other histograms and results do not include events with daughter energy less than 15 GeV.

The probability to obtain a calorimeter subtrigger as a function of shower energy is shown in Fig. 10. Because of the curve's steep rise at low energy, a minimum shower energy requirement of 36.5 GeV is imposed.

Figure 38 shows the vertex distribution for subtracted data and γGF Monte Carlo. Agreement between them is best in the front half of the spectrometer. The beam bends out of the detector while traveling through it. Tracks of daughter muons with the same charge as the beam therefore tend to become shorter as the vertex moves downstream. Inaccuracies in the algorithm used by the Monte Carlo to inject shower-induced hits into the wire chambers have the greatest effect on short tracks and therefore on events occuring in the downstream half of the spectrometer. By cutting on vertex position, the data whose acceptance is not well modeled can be discarded.

The momentum of the daughter muon perpendicular to the virtual photon is shown in Fig. 39. As in Fig. 37, data, γGF, and π, K Monte Carlo events are shown. The horizontal bar indicating rms resolution is 0.15 GeV/c wide. The cut requiring 0.45 GeV/c daughter momentum perpendicular to the scattered muon essentially demands that the daughter μ have a p_T which is nonzero by at least 3σ. The number of tridents contaminating the data is further reduced by this cut. The mean p_T for the subtracted data is 15% higher than for the charm Monte Carlo. This variable is sensitive to

assumptions about -t dependence, not part of the γGF model, so the disagreement does not necessarily reflect a problem with the charm production model.

Figure 40 shows the energy lost by the beam muon for data and both Monte Carlo data sets. All canonical cuts except the ν cut are imposed. The horizontal bar illustrates rms resolution. The agreement between subtracted data and Monte Carlo is spectacular. The π, K-decay events have lower average ν. The ratio of subtracted data to π, K is small for large ν but is of order unity for $\nu < 75$ GeV. To reduce sensitivity to the absolute normalization of the shower Monte Carlo, data with $\nu < 75$ GeV are discarded. The dashed curve shows the predictions of the charm Monte Carlo when the γGF ν dependence is replaced by a flat ν dependence and the fragmentation is changed to $D(z) = \delta(z-1)$.

The Q^2 distributions are shown in Fig. 41. Horizontal bars indicate rms resolution. The π, K events tend to have lower Q^2 than the subtracted data. The γGF model predicts a Q^2 spectrum that is slightly higher than observed.

Figure 42 presents the missing energy for subtracted data and the two Monte Carlos. As expected, the mean missing energy is substantially less in the π, K sample than in the charm sample. The mean missing energies are 4.45 ± 0.53 GeV, 14.59 ± 0.18 GeV, and 18.18 ± 0.24 GeV for π, K Monte Carlo, γGF Monte Carlo, and subtracted data. The

horizontal bar indicates rms resolution and the arrow shows the change in the centroid of the data which results if the calorimeter calibration is varied $\pm 2.5\%$. The relationship between shower energy and pulse height used in both Monte Carlos is fixed by deep inelastic scattering events as described in chapter II. This is an accurate description for π, K-decay events since they <u>are</u> inelastic scattering events. The showers in charm events, in the νGF picture, are caused by the decay products of the charmed particles since very little energy is transfered to the target nucleon. Charm decays almost always include K's in the final state. Since K's have shorter lifetimes and longer absorption lengths than π's, there is no reason to expect that the signature of a charm shower, which may be initiated by two K's and a π, will exactly match that of an inelastic μN collision, which usually does not contain fast strange particles.[30]

Figure 43 shows the inelasticity for data and Monte Carlos. Inelasticity is defined as 1 - E(daughter μ) / ν.

Mean values of reconstructed ν, Q^2, daughter energy, inelasticity, missing energy, and momentum perpendicular to the virtual photon are presented in Table 2. Particularly in the case of ν, daughter energy, and missing energy, the tabulation excludes the possibility that the dimuon data can be explained by π, K-decay.

Systematic errors

After reconstruction, cuts, and background subtraction, the data contain 16 376 events attributed to the production and muonic decay of charmed particles. A sample this large has considerable statistical power-- a total cross section can be determined to a statistical precision of better than 1%. To understand the limitations on the accuracy of results presented here, systematic errors must be investigated. Systematic effects can come from two sources. The backgrounds to charm production may be described incorrectly or the acceptance of the muon spectrometer for charm events may be simulated inaccurately.

The predictions of the shower Monte Carlo are sensitive to the K/π ratio in primary showers. This is the information which is least well determined by CHIO.[29,30] To gauge the Monte Carlo's sensitivity to this ratio, showers were generated with K/π ratios of 0.4 for both signs. The data of Ref. 30 are inconsistent with ratios this high. Simulated trigger rates increased by 60% and the number of shower events surviving the standard cuts increased by 73%.

Since only 10% of the π, K events passing analysis cuts come from the decay of secondary hadrons, the predictions of the simulation are not sensitive to assumptions made about the interactions of primary hadrons in the detector.

A synthesis of charm and shower Monte Carlo samples provides a consistency check. The data are represented as a combination of both simulations. By seeing how the relative normalizations must be changed to fit different kinematic distributions of the data, an estimate of the accuracy of the Monte Carlos was obtained. It is not correct to fix the π, K normalization this way since it then becomes impossible to test the γGF model against the data.

We conclude that the background description provided by the shower Monte Carlo is accurate to within 50%. Therefore, after analysis cuts, our best estimate is that the decay in flight of π and K mesons contributes $(19\pm10)\%$ of the dimuon signal where the quoted error is systematic.

The acceptance of the muon spectrometer is by far most sensitive to the energy spectrum of produced muons. The γGF model describes quasi-elastic charm production; that is, the $c\bar{c}$ pair receives most of the energy of the virtual photon. The charm model accurately predicts the ν dependence of the subtracted data. Varying the fragmentation function D(z) used to create D's from $c\bar{c}$ pairs allows investigation of this sensitivity. D(z) provides the link between ν, which is correctly modeled, and daughter energy. The form for D(z) used[26] in acceptance modeling is $D(z) = (1-z)^{0.4}$. Remodeling with $D(z) = (1-z)^3$ and $D(z) = (1-\min(z,0.99))^{-1.5}$ changes the detector acceptance by -19% and +20%, respectively. The exponents in the "too soft" and "too

hard" functions are more than 5σ from the value determined at SPEAR.[26] The mean daughter energies which result are presented in Table 3. Agreement in energy and other distributions is spoiled by using the alternative fragmentation descriptions.

When same-sign dimuon data and opposite-sign dimuon data are analyzed separately, little change is seen in data-to-Monte Carlo ratios. Cross sections based only on same-sign or opposite-sign events differ by 3.5% from those based on both signs.

Systematic uncertainties in π, K modeling and charm modeling are not expected to be significantly correlated. An estimate of the total systematic error is made by reanalyzing the data with different assumptions. Errors are parametrized by (1) decreasing, (2) increasing by 50% the subtracted shower background and by recalculating the acceptance with the (3) softer, (4) harder fragmentation function. The effects on results are obtained by reanalyzing the data with each of the four systematic changes, adjusting the ΥGF normalization to yield the observed number of events past cuts, and replotting or recalculating acceptance-corrected information. All positive deviations from the canonical results are added in quadrature to yield the positive systematic error and all negative deviations are added in quadrature to yield the negative systematic error. The results define bands of

systematic tolerance around observed distributions. Cross sections presented in the next chapter will include systematic errors of +28% and -20%.

CHAPTER IV

RESULTS AND DISCUSSION

The spectra in figures 37 and 39-43 reflect physical processes seen through the prism of experimental acceptance. By removing detector effects with a Monte Carlo simulation, the nature of the underlying physics may be studied. This chapter describes acceptance correction and presents measurements of charm production by muons and virtual photons. Results include the total diffractive cross section for muoproduction of charm and the Q^2 and ν dependence of virtual photoproduction of charm. The cross section for charm production by real photons and its contribution to the rise in the photon-nucleon total cross section are discussed. The role played by charm in the scale-noninvariance of muon-nucleon scattering at low Bjorken x, $Q^2/(2M\nu)$, is described. A lower limit on the ψ-nucleon total cross section is presented.

Acceptance correction

Most spectra presented in the following sections are differential in Q^2 or ν. To unfold the experimental acceptance, data, π, K-decay Monte Carlo, and γGF Monte Carlo are placed in $(\ln(Q^2), \ln(\nu))$ bins. If $\Delta\sigma(Q^2,\nu)$ is the number of events in the $(\ln(Q^2), \ln(\nu))$ bin which includes the values Q^2 and ν, the ratio of subtracted data to charm Monte Carlo in a bin is

$$\frac{\Delta\sigma(\text{data}) - \Delta\sigma(\pi,K)}{\Delta\sigma(\gamma\text{GF})}$$

For small bins, the ratio of the acceptances for subtracted data and charm Monte Carlo will be constant across the width of a bin. Because of resolution smearing, the measured average values of Q^2 and ν in a bin will generally differ from the true average values. The charm Monte Carlo is used to calculate the shift between measured and true mean Q^2 and ν. The acceptance-corrected differential cross section which results is

$$\frac{d^2\sigma(\text{charm})}{dQ^2 d\nu} = \frac{d^2\sigma(\gamma\text{GF})}{dQ^2 d\nu} \times \frac{\Delta\sigma(\text{data}) - \Delta\sigma(\pi,K)}{\Delta\sigma(\gamma\text{GF})} .$$

Here, σ(charm) is the cross section for charm production by muons and Q^2 and ν are the corrected average values in the bin. This procedure, which equates real cross sections with

Monte Carlo cross sections weighted by the ratio of subtracted data to Monte Carlo, is used to obtain the results presented in the following sections.

Diffractive charm muoproduction cross section

The measured cross section for diffractive charm production by 209 GeV muons is $6.9^{+1.9}_{-1.4}$ nb. "Diffractive production" refers to the creation of $c\bar{c}$ pairs carrying most of the laboratory energy of the virtual photon, as in the VGF and VMD models. This analysis is insensitive to mechanisms which might produce charm nearly at rest in the photon- nucleon center of mass. To correct for experimental acceptance, the cross section is computed by multiplying the VGF prediction of 5.0 nb by the ratio of subtracted data to VGF Monte Carlo. A total of 20 072 data events, 944 π, K Monte Carlo events (scaled to 3696 events), and 13 678 VGF Monte Carlo events survived reconstruction and analysis cuts to contribute to this ratio. The error on the cross section is systematic and reflects uncertainties in background subtraction and acceptance modeling, as described earlier. The statistical uncertainty is negligible compared to the systematic error. Ignoring nuclear shadowing and coherence would raise the reported cross section by 9.4%. After a

(26±5)% relative acceptance correction, the opposite-sign to same-sign ratio for background-subtracted data is 1.07±.06.

A Michigan State-Fermilab (MSF) experiment has reported a cross section for charm production by 270 GeV muons of 3±1 nb.[57] Correcting the beam energy to 209 GeV, using the VGF model, reduces the MSF cross section to 2.1±0.7 nb. The MSF data contain 412 fully reconstructed dimuon events; the collaboration simulates detector acceptance with a phenomenological model containing three free parameters.[58] Their choice of parameters was based on a sample of 32 dimuon events observed earlier at a beam energy of 150 GeV.[59] The 150 GeV sample contained an estimated 4.9 trident events and a small, but unspecified, number of π, K-decay events. Our results are inconsistent with the MSF measurement.

Virtual and real photoproduction of charm

As a beam muon passes near a target nucleon, its electromagnetic field may transfer momentum and energy to the target. In the single-photon approximation, the interaction is described as the absorption by the target of a virtual photon from the beam particle. There is intuitive appeal to characterizing the muon's field as a cloud of

virtual quanta-- classically, the field of a rapidly moving charge behaves like a pulse of radiation as it passes a stationary observer.[60] In the spirit of this, the differential charm production cross section may be written

$$\frac{d^2\sigma}{dQ^2 d\nu} = \Gamma_T \sigma_T + \Gamma_L \sigma_L .$$

The factors Γ_T and Γ_L represent the fluxes of transversely and longitudinally polarized virtual photons with mass^2=$-Q^2$ and energy ν. The terms $\sigma_T(Q^2,\nu)$ and $\sigma_L(Q^2,\nu)$ are the cross sections for photons of the two polarizations to be absorbed by the target to yield charmed particles. More compactly, defining $\epsilon = \Gamma_L/\Gamma_T$ and $R = \sigma_L/\sigma_T$ gives

$$\frac{d^2\sigma}{dQ^2 d\nu} = \Gamma_T (1+\epsilon R)\sigma_T .$$

Parametrizations of Γ_T and ϵ from Ref. 61 are used to extract virtual photon cross sections from muon cross sections:

$$\Gamma_T = \frac{\alpha}{2\pi} \frac{(\nu^2+Q^2)^{1/2}}{Q^2 E^2 (1-\epsilon)}$$

$$\epsilon^{-1} = 1 + \frac{2(Q^2+\nu^2)\tan^2\frac{\theta}{2}}{Q^2}$$

Here, E is the beam energy, M is the nucleon mass, θ is the muon scattering angle in the laboratory, and (Bjorken) x is

$Q^2/(2M\nu)$. Figure 44 shows $Q^2\Gamma_T$ vs. Q^2 for different values of ν; Fig. 45 illustrates the polarization ratio, ϵ. The flux Γ_T is normalized so that as Q^2 approaches zero, the effective cross section $\sigma_{eff} = (1+\epsilon R)\sigma_T$ approaches the cross section for real photons of energy ν.

Q^2 dependence of the effective photon cross section

The effective photon cross section is obtained by factoring the equivalent flux of transversely polarized virtual photons out of the muon cross section. A measurement of R would require a substantial amount of data at a second beam energy and has not been made. There is no reason to expect σ_L/σ_T for charm production to equal σ_L/σ_T for deep inelastic scattering. In peripheral models like γGF and VMD, the photon couples to the produced quark pair, not to a valence quark in the target. Consequently, the kinematic effects which determine R for charm are different from those which influence R for inelastic scattering. Figure 46 shows R as predicted by γGF and Fig. 47 shows the product ϵR.

The Q^2 dependence of the effective photon cross section is shown in Fig. 48 and Table 4. The data are grouped into two ν bins, covering the regions 75 GeV$< \nu <$ 133 GeV with

$\langle\nu\rangle$ = 100 GeV and ν > 133 GeV with $\langle\nu\rangle$ = 178 GeV. In the figure, data points are shown with statistical errors. The solid lines are best fits to VMD propagators, $\sigma(Q^2) = \sigma(0)(1+Q^2/\Lambda^2)^{-2}$. The dashed curves, normalized to the nominal value of $\sigma(0)$, indicate the influence of the systematic effects discussed previously. Systematic errors are parametrized by (1) decreasing, (2) increasing by 50% the subtracted π, K-decay background and by recalculating the acceptance with the (3) softer, (4) harder fragmentation function described above. The mass parameter Λ is 3.3 ± 0.2 GeV/c and 2.9 ± 0.2 GeV/c for the 178 GeV and 100 GeV data, respectively. Extrapolated to $Q^2=0$, the data are best fit by $\sigma(0)$ of 750^{+180}_{-130} nb and 560^{+200}_{-120} nb for the 178 GeV and 100 GeV data. The errors on Λ and $\sigma(0)$ are systematic. A drop in σ_{eff} with decreasing Q^2 is present below $Q^2=.32$ $(GeV/c)^2$. Fits which do not include data in this region yield essentially the same results.

A wide-band photon-beam experiment has measured cross sections averaged from 50-200 GeV of 464 ± 207 nb for $D^0\bar{D}^0$ pair production[62] and, later, 295 ± 130 nb for inclusive D^0 production.[63] Using SPEAR data[21], one may crudely estimate the neutral D:charged D:F:Λ_c ratio to be 2:1:1:1 at $m_{c\bar{c}} \sim$ 4-5 GeV/c^2. The average of the two D^0 cross sections is 343 ± 110 nb, corresponding to a total cross section for charm production of $\sim$860 nb. This is consistent with our measurement. The authors of Refs. 62 and 63 determine

experimental acceptance with a model which uses a fragmentation function $D(z)=\delta(z-1)$ and assumes no energy dependence above 50 GeV. The dashed curve in Fig. 40 shows that the muon data do not support these assumptions.

Contribution of charm to the rise in the photon-nucleon total cross section

Above ~40 GeV, the photon-nucleon total cross section increases with energy.[64,65] This rise presumably reflects the "hadronlike properties" of the photon;[65] most hadronic total cross sections begin to rise in this energy region. The authors of Ref. 65 suggest that charm production may contribute 2 to 6 μb of this increase in the energy range from 20 GeV to 185 GeV. A fit to half the photon-deuteron cross section from Ref. 64 is shown in Fig. 49. Since the threshold energy for charm production is about 11 GeV, the charm cross section rises from zero at low energy to the values reported here at ν=100 GeV and ν=178 GeV. Diffractively produced charm is seen to make only a minor contribution to the rise in the photon-nucleon total cross section.

ν dependence of the effective photon cross section

The ν dependence of the effective photon cross section in the range $0.32\ (GeV/c)^2 < Q^2 < 1.8\ (GeV/c)^2$ is shown in Fig. 50 and Table 5. For fixed ν, the cross section σ_{eff} varies by less than 20% in this range of Q^2. Data in the figure are shown with statistical errors. Systematic uncertainties, parametrized as described previously, are indicated by the shaded band, referenced to the solid curve for visual clarity. To gauge the systematic error associated with a given point, the shaded region should be moved vertically until the position cut by the solid line rests on the data point. Data with $\nu < 75$ GeV are excluded from the analysis because of their large systematic uncertainty.

The solid curve exhibits the ν dependence of the γGF model with the gluon x_g distribution $3(1-x_g)^5/x_g$ and represents the data with 13% confidence. Other gluon distribution choices, $(1-x_g)^9/x_g$ and "broad glue"[17] $(1-x_g)^5(13.5+1.07/x_g)$ are indicated by dashed curves. The dashed curve labeled "BN" represents the phenomenological parametrization of Bletzacker and Nieh[66] and the horizontal dashed line represents energy-independence. All curves are normalized to the data.

The muon data clearly indicate that σ_{eff} increases with

photon energy. The standard "counting-rule" gluon distribution is favored, but systematic uncertainties prevent the analysis from ruling out the BN model or the two extreme choices for the gluon x_g distribution.

The charm structure function

In quantum mechanics, the probability for a free particle in a state $|\vec{p}\rangle$ to scatter from a potential $V(\vec{r})$ into a state $|\vec{p}'\rangle$ is $\left|\langle \vec{p}'| V(\vec{r}) |\vec{p}\rangle\right|^2$, in familiar notation. If the potential is localized in space and reasonably "well behaved," the initial and final states are well approximated by plane waves. Neglecting normalization, in non-relativistic quantum mechanics, the scattering probability becomes

$$\left| \int d^3\vec{r}\; e^{i(\vec{p}-\vec{p}')\cdot\vec{r}}\, V(\vec{r}) \right|^2 .$$

Defining $\vec{q}$ to be $\vec{p}-\vec{p}'$ and $F(q^2)$ to be the Fourier transform of the potential allows the scattering probability to be written as $|F(q^2)|^2$. By studying the scattering process, the short-range nature of the potential $V(\vec{r})$ can be measured.

The high energy analogue of $F(q^2)$ in potential scattering is the nucleon structure function $F_2(x,Q^2)$ in

deep inelastic lepton scattering. For muon-nucleon collisions, the scattering cross section is

$$\frac{d^2\sigma}{dQ^2 d\nu} = \frac{4\pi\alpha^2}{\nu Q^4}\left[1 - y + \frac{y^2}{2(1+R(x,Q^2))}\right] F_2(x,Q^2) \ .$$

The variables x and y are $Q^2/(2M\nu)$ and ν/E where M is the nucleon mass and E is the beam energy. By measuring the structure functions F_2 and R, the small-scale structure of the nucleon can be probed. As before, R is σ_L/σ_T, the ratio of the cross sections for the target to absorb longitudinally and transversely polarized virtual photons with mass$^2 = -Q^2$ and energy ν.

The quark model provides a particularly simple interpretation for F_2. Beam muons scatter elastically from the pointlike constituents of the nucleon. Subsequent interactions of the struck quark with the rest of the target produce a hadronic shower and do not influence the initial collision. Since the muon-quark interaction is elastic, the relationship between Q^2 and ν is $Q^2 = 2m\nu$, where m is the quark mass. Within the quark-parton model, the muon scatters elastically from a quark which carries momentum xP, where P is the nucleon momentum in a frame where P is very large. The structure function $F_2(x,Q^2)$ is x times the probability to find a quark in the nucleon with this momentum. In this model, F_2 is scale-invariant and depends only on x, not on both x and Q^2. This is seen to be

approximately true; $F_2(x,Q^2)$ with x held constant shows only weak Q^2 dependence.[20,67] In quantum chromodynamics (QCD), the quark-antiquark pairs in processes like $g \to q\bar{q} \to g$ should be revealed by the short-distance resolution of high-Q^2 scattering. Consequently, as Q^2 increases, the nucleon momentum should seem to be carried by more and more quarks and the average quark momentum should drop. The structure function F_2 will increase at small x and decrease at large x as Q^2 grows. This scale-noninvariance of F_2 has been experimentally observed.[20,67] F_2 increases with Q^2 for fixed $x \lesssim 0.25$ and decreases with increasing Q^2 for fixed $x \gtrsim 0.25$.

The description of scattering in terms of structure functions is equivalent to the description in terms of virtual photon fluxes and cross sections. The relationship between F_2, σ_T, and σ_L is[20]

$$F_2 = \frac{\nu(\nu - Q^2/2M)}{4\pi^2\alpha} \frac{Q^2}{Q^2+\nu^2} (\sigma_T+\sigma_L).$$

A structure function may be defined for any process once its Q^2 and ν dependence are measured.

We define a charm structure function, $F_2(c\bar{c})$ as the analogue of the nucleon structure function F_2 through the expression

$$\frac{d^2\sigma(c\bar{c})}{dQ^2 d\nu} = \frac{4\pi\alpha^2}{\nu Q^4}\left[1 - y + y^2/2\right] F_2(c\bar{c}).$$

In this definition, $R(x,Q^2)$ is neglected. However, the

comparison of $F_2(c\bar{c})$ with γGF model calculations takes the model's predictions both for σ_L and σ_T fully into account. Figure 51 and Table 6 show $F_2(c\bar{c})$ as a function of Q^2 for fixed ν at two values of average ν. Data are presented in the figure with statistical errors; the systematic uncertainty associated with each point is indicated by the shaded band. As in Fig. 50, the systematic error for a point may be determined by moving the shaded region to cover that point. Each curve, at each of the two average photon energies, is normalized to the data. The curves labeled m_c=1.5 and m_c=1.2 are γGF predictions with charmed quark masses of 1.5 GeV/c^2 and 1.2 GeV/c^2. Curves labeled ψDM are vector-meson dominance predictions using the ψ mass in the VMD propagator. The curves labeled BN represent the model of Ref. 66. Shown at the top is a fit adapted from CHIO[20] to the inclusive structure function F_2 for isospin-0 muon-nucleon scattering. At its peak, $F_2(c\bar{c})$ is ~4% of F_2.

Since a $c\bar{c}$ state must have $m_{c\bar{c}} \gtrsim 2m_D$ to produce charmed particles, the parametrized quark mass m_c affects γGF's absolute normalization, not the shapes of its distributions. The maxima predicted by both the γGF and BN models resemble the data in shape and ν dependence, but occur at higher values of Q^2. The ψ-dominance functions drop too slowly at high Q^2. Systematic errors are only weakly correlated with Q^2 and do not obscure the disagreement. When α_s is redefined to be a function of $m_{c\bar{c}}^2+Q^2$, instead of $m_{c\bar{c}}^2$, the

agreement between data and νGF improves.[68]

$R(x,Q^2)$ is absorbed by $F_2(c\bar{c})$ in the definition of the structure function used in this analysis. Alternative assumptions about R could be made; the values of such a redefined F_2 would change typically by less than the reported systematic uncertainties.

The role of charm in scale-noninvariance

The relationship between $F_2(c\bar{c})$ and $\sigma_{eff}(c\bar{c})$ may be written as

$$F_2(c\bar{c}) \approx \frac{1-x}{4\pi^2\alpha}\left(\frac{Q^2}{1+Q^2/\nu^2}\right)\sigma_{eff}(c\bar{c}).$$

Since most data reported here have $x \leq 0.1$, at fixed ν $F_2(c\bar{c})$ will grow with Q^2 until σ_{eff} begins to decrease, when $Q^2 \geq m_\psi^2$. Because σ_{eff} rises with energy, $F_2(c\bar{c})$ will also increase when Q^2 and ν are increased but x is held constant.

In the past, muon experiments measuring deep inelastic scattering have been unable to recognize charm production in their inclusive scattering data.[20,30,67] The detectors used by these experiments have been insensitive in the region traversed by the beam, which has severely limited their detection efficiency for charm states. As a result, typical measurements of inclusive F_2 and its scale-noninvariance

have included all or part of the contribution from charm. Data from this experiment determine how much of the previously measured F_2 results from diffractive charm production, described by $F_2(c\bar{c})$.

Figure 52 shows the behavior of $F_2(c\bar{c})$ as a function of Q^2, with x held constant. Data points are arranged in pairs, alternately closed and open, and are connected by solid "bowtie-shaped" bands. The points in a pair represent data with the same value of x, but different Q^2. Data are shown with statistical errors. The systematic uncertainty in the slope of a line connecting the points in a pair is indicated by the solid band. Pairs are labeled by their values of Bjorken x. The dashed curves are the predictions of the γ GF model, normalized to the data and damped at high Q^2 by the ad hoc factor $(1 + Q^2/(100\ GeV^2/c^2))^{-2}$. The damping factor forces the model to agree with the data at large values of Q^2. The dot-dashed lines represent the changes in $F_2(c\bar{c})$ as Q^2 is increased but x is held constant that would be necessary to equal the changes in the CHIO fit to F_2 which occur under the same circumstances. Their relative sizes are given by the percentages next to the lines.

The scale-noninvariance of $F_2(c\bar{c})$ is indicated by the non-zero slope in the line connecting the points in each pair. Diffractively-produced charm causes about one-third of the low-x scale-noninvariance measured by CHIO in the

range $2\ (GeV/c)^2 < Q^2 < 10\ (GeV/c)^2$. This charm-induced scale breaking is a purely kinematic effect related to the heavy mass of charmed particles.

The production of bound charm states also contributes to the scale-noninvariance of F_2. The ψ muoproduction rate agrees[18,19,23] with the unmodified QGF prediction if elastic ψ production accounts for 1/6 of all charmonium production. To estimate the net effect of charm on F_2, the model's predictions for 2.8 nb of bound and 6.9 nb of open charm are combined to produce the results in Table 7. The numbers in the table are grouped in pairs. The top number in each pair is $10^4 d F_2(c\bar{c}) / d \ln(Q^2)$ at fixed x. $F_2(c\bar{c})$ is calculated as the sum of $F_2(c\bar{c})$ for $m_{c\bar{c}} < 2m_D$ as predicted by QGF and $F_2(c\bar{c})$ for open charm production as predicted by QGF but damped at high Q^2 and normalized to the data. This damped, renormalized $F_2(c\bar{c})$ matches the data in Fig. 52. The bottom number is $10^4 d F_2 / d \ln(Q^2)$ at fixed x for the fit to F_2 adapted from CHIO.[20] Charmonium production increases the scale-noninvariance of $F_2(c\bar{c})$ by ~15%.

The results in Table 7 are calculated, not measured. Data from the muon experiment cover the Q^2-ν region of the two columns on the right side of the table. Where the charm scale-noninvariance is most important, the calculation is reliable to $\sim \pm 40\%$. The QGF model predicts that charm accounts for about one-third of the inclusive scale-noninvariance in the region

$2(GeV/c)^2 < Q^2 < 13(GeV/c)^2$ and $50\ GeV < \nu < 200\ GeV$, centered at $x \sim 0.025$. This region provided most of the original evidence[67] for scale-noninvariance in muon scattering.

The consequences of charm-induced scale breaking for QCD predictions of scale-noninvariance depend on the level of detail sustained by the QCD calculation. Calculations which correctly describe the charmed sea in principle should be able to predict scale-breaking which properly includes the effects of charm production. Alternatively, $F_2(c\bar{c})$ may be subtracted from the experimentally measured structure function F_2 for comparison with QCD models which do not quantitatively describe the charmed sea at low Q^2.

The data indicate that the mechanism for charm production resembles γGF. The study of events with three final state muons discussed earlier also suggests that γGF correctly describes these events. If this is true, charmed quarks tend to share equally the photon's energy. Results from another muon experiment confirm this tendency.[69]

The ratio of ψ production to charm production and the ψN total cross section

The Okubo-Zweig-Iizuka[70] (OZI) selection rules and vector-meson dominance suggest a relationship between ψ

production and charm production.[71] In the OZI picture, final states from ψ-N collisions tend to contain charmed quarks. It is more likely for the $c\bar{c}$ of the ψ to survive the interaction than to annihilate. Vector-meson dominance describes ψ photoproduction as a two-step process. The incident photon changes into a ψ which then scatters from the target. The virtual ψ gains enough energy and momentum to materialize as a real particle. Together, OZI rules and VMD indicate that charm production should result from inelastic ψN scattering. In this light, the ratio of charm production and ψ production should equal the ratio of the inelastic and elastic ψ-N scattering cross sections.

Sivers, Townsend, and West (STW) discuss the connection between charm production and inelastic ψN interactions.[71] They use VMD and the width for the decay $\psi \rightarrow e^+e^-$ to derive a relationship between $d\sigma/dt(\gamma N \rightarrow \psi N)$ and $d\sigma/dt(\psi N \rightarrow \psi N)$. The optical theorem and -t dependence measured at SLAC then determine the ψN total cross section in terms of $d\sigma/dt(\psi N \rightarrow \psi N)$. STW equate the ψN total cross section with the $\psi N \rightarrow$ charm cross section and estimate the ratio of ψ photoproduction to charm photoproduction to be $(1.3\pm0.4)\times10^{-2}/\lambda$. The constant λ depends on the variation of the $\gamma\psi$ and the ψN couplings with Q^2; its value is about one-half. Our data on ψ production[23] and the results reported here fix the ratio of elastic ψ to diffractive charm production at 0.045 ± 0.022, somewhat larger than their

prediction.

Sivers, Townsend, and West also calculate a lower limit for the ψN total cross section without assuming VMD.[71] They use unitarity and OZI rules to obtain the limit in terms of the ψ photoproduction cross section, the charm photoproduction cross section, particle masses, and the amount of OZI violation. With our data on ψ and charm production, their calculation yields the 90% confidence limit

$$\sigma_{total}\ (\psi N) > 0.9 \text{ mb.}$$

Conclusions

Data from the Multimuon Spectrometer at Fermilab have provided a first measurement of differential spectra for diffractive charm production by muons. The results are in general agreement with the virtual photon-gluon fusion model.[17] At large Q^2, the data show disagreement both with that model and with the predictions of Vector Meson Dominance. By redefining the strong coupling constant α_s, the agreement between γGF and data can be improved. Charm production contributes substantially to the scale-noninvariance at low Bjorken x which has been

observed[20,67] in inclusive muon-nucleon scattering. The ratio of the rates for ψ and charm photoproduction is higher than predicted by a calculation[71] which uses VMD and OZI rules. Without VMD, a calculation[71] and charm and ψ[23] production data set a lower limit on the ψN total cross section of 0.9 mb (90% confidence).

ACKNOWLEDGEMENTS

This experiment was performed by groups from Princeton, Berkeley, and Fermilab. The Princeton group consisted of my advisor, Frank Shoemaker, Pam Surko, and me. We were aided by the mechanical expertise of Howard Edwards and other technicians at the EP lab. Carl Bopp, Ann David, and Marius Isaila labored with herculean fortitude to assemble our drift chamber electronics. Al Clark, Karl Johnson, Roy Kerth, Stew Loken, Tom Markiewicz, Peter Meyers, Wesley Smith, Mark Strovink, and Bill Wenzel were the physicists in the Berkeley contingent. Fred Goozen and other technicians provided skilled technical support from LBL. John Caron toiled arduously to create sophisticated analysis software and Teri Martin tended the administrative fires in Berkeley. Rol Johnson, Craig Moore, Marshall Mugge, and Bob Shafer were in the Fermilab group. Garvie Hale's able assistance at Fermilab was invaluable. I owe a substantial debt of gratitude to all who worked on the muon experiment.

Dr. Yee Keung kindly gave me Monte Carlo generators for charm and muon tridents and explained some of their features. Professors Frank Merritt and Michael Shaevitz willingly discussed shower Monte Carlo simulations with me. The high energy physics groups of the University of Chicago graciously provided me with office space and transportation

between Hyde Park and Fermilab for the last year of my graduate work.

Appendix A (IEEE Transactions on Nuclear Science, Vol. NS-26, No. 1, February 1979)

DRIFT CHAMBER SYSTEM FOR A HIGH RATE EXPERIMENT*

G. Gollin, M. V. Isaila, F. C. Shoemaker and P. Surko

Department of Physics, Princeton University, Princeton, N. J. 08540

Abstract

A system of 19 large drift chambers has been built and used in an experiment in the FNAL muon beam. The design of the chambers and electronics enabled the system to perform with incident particle rates of up to 10^7 per second.

Introduction

A magnetized iron spectrometer has been built and used in a muon experiment, E203A/391, at Fermilab. The iron is in modules separated by 10 inch gaps in which are located the track chambers. Each gap has a multiwire proportional chamber with horizontal, vertical, and diagonal coordinates read out. The anode wires, which measure the position of tracks in the bending (horizontal) plane, have 1/8 inch spacing.

To improve the resolution in the bending plane and to increase by redundancy the efficiency of detection, a single sense plane drift chamber was included in each gap. The drift chamber's active area is 42 x 72 inches. The left-right ambiguity in the drift chambers was to be resolved by track fitting in the drift and multiwire chambers.

The iron in the region between the chambers formed a distributed target, magnetized vertically with a quite uniform field. Since the beam passed directly through all of the chambers, the beam muon's track could be tied to the final state muons' tracks at the interaction vertex, improving the resolution in momentum and track angle. In addition, final state tracks from multi-muon events which lie in the beam region were not lost. Because the drift chambers had the intense beam and halo passing directly through them, their design was somewhat different from that of most chamber systems.

The experiment was designed for an incident muon flux (including the halo) of up to 10^7 per second. Therefore, a shorter than usual drift distance was chosen to minimize the number of accidental tracks. Even so, a three prong event would be expected to have two or three accidental tracks accompanying it in the data read out from the drift chambers. Because of this, the chamber system needed to be able to record more than one hit per wire per event[1]. The sense amplifier-discriminators were built with a short dead time and the time digitizing system was designed with the ability to latch more than one signal per wire. With this multi-hit capability, the data could be plagued by false signals made by straggling electrons from ion pairs created away from the mid plane of the cell. These electrons follow longer electric field lines to the sense wire. The drift cell geometry was chosen to effectively minimize this problem.

Chamber Design

The drift cells were constructed using graded potentials on the cathode wires, similar to the system developed by Charpak[2]. The cells' dimensions also were similar, except that the maximum drift distance was chosen to be 3/8 inch. This was a compromise between the cost of too many channels and the problem of excessive background tracks associated with too long a memory (drift) time. With this drift distance, the maximum drift time on the mid plane of the cell was 175 ns. The spacing between the cathode wire planes was 1/4 inch. A thin chamber with Charpak's geometry is advantageous if the electronics are designed with multi-hit capability in each channel, as it minimizes the number of late electrons.

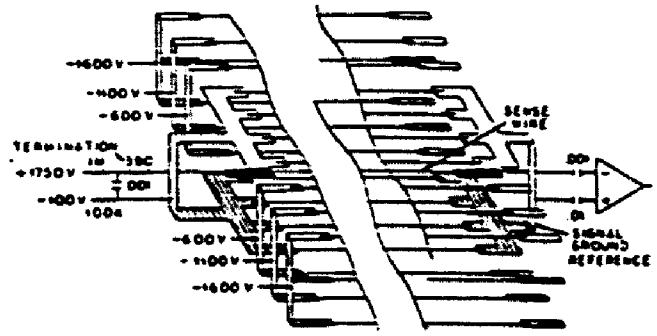

Fig. 1. Schematic Diagram of one Drift Chamber Cell

Fig. 1. is a schematic diagram of one drift cell, showing the applied voltages and the signal connections. Note that the four wires closest to the sense wire on each side of the chamber are connected together to provide a "clean" signal ground reference. These eight wires, with the sense wire, form a coaxial transmission line with a characteristic impedance of about 400 ohms. The signal from an event divides, half going towards the sense amplifier, half going in the opposite direction, towards the bottom of the chamber. The reflection of the latter from the end of the line would arrive at the amplifier too late to be of use and could increase the effective dead-time of the sense amplifier. Therefore, the sense wire is terminated at the bottom of the chamber. The cathode wire system was biased at -100 volts to form a clearing field which prevents electrons released outside of the drift cells from entering the cells and producing late signals. Without this bias, the late electron signal was 60 per cent of the number of tracks through the chamber. With the bias, straggling electrons contributed less than 15% of the rate. The lower limit on this contribution is uncertain since monte-carlo calculations predicted that delta rays accompanying the muons would produce about this rate of double hits.

A plot of the electric field equipotentials in a half cell, made using conducting paper, is shown in Fig. 2. The spacing of the equipotentials is 167 volts. Note that the connection of four of the cathode wires together did not damage the uniformity of the drift field. The sense (anode) wires were 20 micron gold plated tungsten. The cathode wires were 100 micron silver plated beryllium copper. In tests with model chambers, it was found that 50 micron cathode wires produced field emission.

*Supported by the Department of Energy Contract #EY-76-C-02-3072

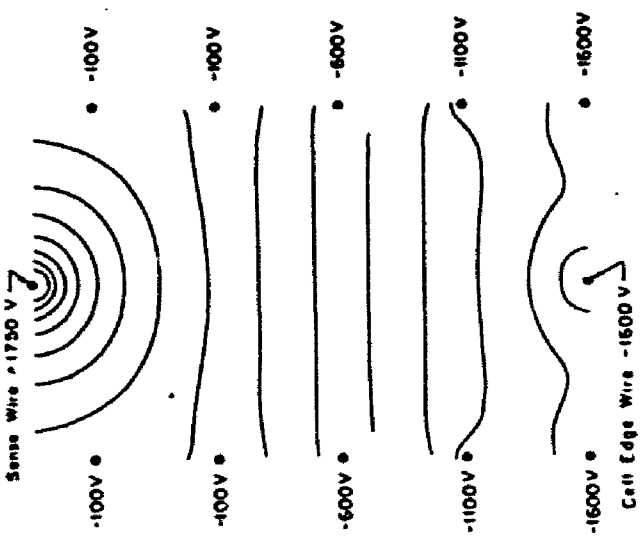

Fig. 2. Equipotentials of the Electric Field in a Half Cell

In an iron spectrometer, there is no need for thin chamber windows, so the drift chambers were built on 5/8 inch thick sheets of aluminum "tool and jig" plate. Each plate was 4 x 8 feet. This simplified the construction, and enabled the active width of the chamber to be a larger fraction of the space between the magnet coils than would be the case if a heavy frame were needed. The chambers were mounted with the (low Z) aluminum plate up beam from the active volume to reduce the number of delta rays. The down beam window was 1/16 inch aluminum, providing an impermeable structure and good shielding, as well as an equipotential for the clearing field.

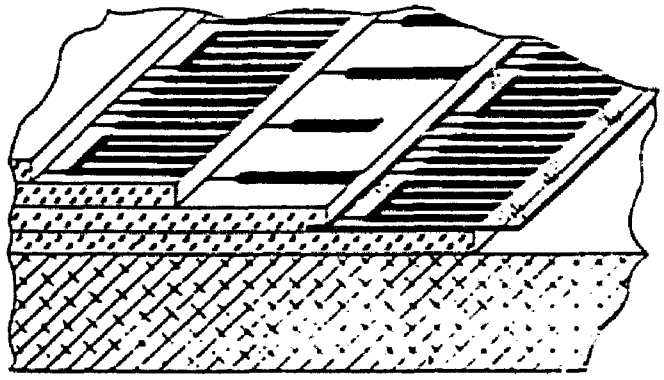

Fig. 3. Chamber Construction Detail

Fig. 3 shows the way the wires were mounted. They were soldered to pads formed by printed circuit techniques on 1/8 inch thick G-10 sheets. After each plane was wound, the next layer of G-10 was epoxied in place. The Mylar covering the solder pads on the bottom layer of cathode wires was needed to prevent dark current from flowing to these pads. The sense wires and cell edge wires were laid by hand on precisely scribed lines. No difficulty was found in replacing broken or mis-laid wires - all that was required was the removal of one or two of the cathode wires on the top plane. This construction did initially cause problems in the proper cleaning of the wire planes. A brush and solvents, the usual chamber cleaning tools, did not reach the bottom cathode plane and as a result, the chambers had excessive noise rates. It was found, however, that squirting solvents onto the wires and blowing them dry with nitrogen reduced the noise rates nearly to the calculated cosmic ray rate.

The length of the sense wires, 72 inches, is about the maximum stable length for a safe tension on the 20 micron tungsten wire. To insure that the wires remained centered between the cathode planes, bridges of G-10 were placed 12 inches on either side of the center, dividing the chamber into thirds. These constrained the cathode planes as well as the sense plane, so that twists in the supporting aluminum plate would not influence the spacing. The space between the G-10 strips on either side of the sense plane was determined by the cell edge wires, so that the thinner sense wires were free. To insure that they did not hang up on the bridges, the chambers were pounded with a hammer as they hung with the wires vertical.

The gas was similar to that used by Charpak,[2] approximately 2/3 argon, 1/3 isobutane, except that the concentration of methylal was increased. During tests on model chambers, it was found that an intense Ru^{106} beta gun could quickly deaden a section of a chamber unless the methylal content of the gas was greater than in Charpak's. Consequently, all of the argon was bubbled through methylal at 0° C. There was no degradation of the chambers' performance caused by the intense muon beam in spite of the large currents (80 μA per drift chamber) drawn during the spill.

Sense Amplifier - Discriminator

The sense amplifiers were each constructed of two Texas Instruments 10116 ECL integrated circuits. These are triple differential line receivers with differential outputs. The voltage gain from differential input to differential output is about 13, and the rise time is about 5 ns for small signals and 2 ns for saturated signals. Fig. 4 shows the amplifiers' schematic diagram. Not shown are pulldown resistors between the amplifier outputs and -5 volts on all stages. The pulldown resistors were 1500 ohms on all stages except the last, which had 330 ohm resistors.

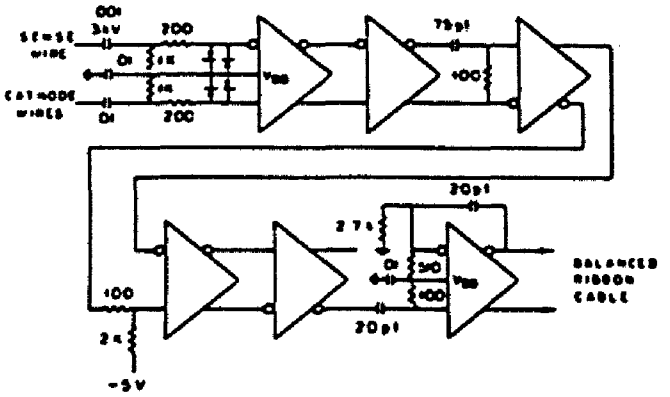

Fig. 4. Schematic Diagram of the Sense Amplifier-Discriminator

To increase the system's common mode noise immunity, the amplifier's differential inputs were AC coupled to the cathode and sense wires of the drift chamber. AC coupling produced no problems because it was necessary to clip the input pulses severely to reduce the dead time to acceptable levels. Drift chamber pulses typically have a length of 200 ns. The clipping was performed by 7.5 ns RC differentiation between the second and third stages. It was placed there to avoid saturation of any amplifiers before the clip, and to eliminate any difficulties due to DC offset of the input stage.

The input of the amplifier was protected by back-to-back diodes. It is not known that they were needed, but there was no difficulty with failure of inputs during the experiment. Note that the input has a high impedance (2000 ohms differential). This increased the sensitivity of the amplifier by pulse-reflection doubling and caused no difficulties because the opposite end of the sense wire was terminated.

The sensitivity of the amplifier-discriminator was set by the 200 millivolt bias at the input to the third stage. The subsequent stages produced a saturated ECL pulse which triggered the output stage through a 2 ns time constant. The output was connected as a one-shot (monostable) circuit which produced a 15 ns standard output pulse with a differential amplitude of about 1.8 volts.

The threshold sensitivity was 0.5 millivolts, measured with a signal which had a 200 ns decay time-constant to simulate drift chamber pulses. The dead time, measured at the end of the 200 foot ribbon cable, and after the line receiver in the digitizer, was 35 ns. The calculated efficiency, assuming 6 tracks in the chamber, is then about 0.98.

Time Digitizers

The digitizers designed for this experiment followed generally the logical system which Sauli[1] refers to as a Digitron[3] with "complete addressing". A five-bit binary scaler is capable of dividing the drift time into 31 time bins, of about 7 nanoseconds each. Because of the multiple scattering in the iron, a finer subdivision would be pointless. This made possible a relatively simple system, shown in Fig. 5.

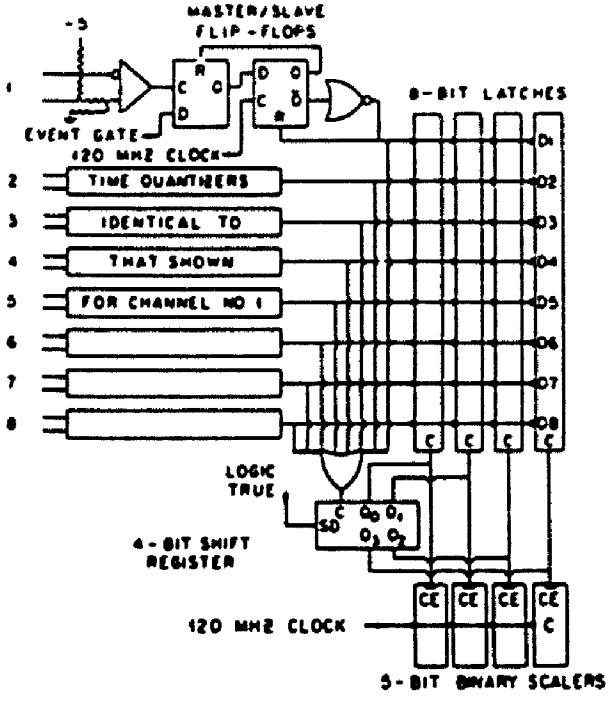

Fig. 5. Schematic Diagram of the Time Digitizer

The signals from the sense amplifiers were transmitted and delayed by ribbon cables about 200 feet long. The experiment's trigger logic produced a "pre-trigger" which was used to initiate the digitizing process and which served as the time reference. This minimized the delay required in the ribbon cables. If the full trigger requirements turned out to be unsatisfied, the digitizers were cleared, resulting in a deadtime of only a microsecond. The differential signal from the ribbon cable was amplified by a 10115 differential line receiver. The resistor network at the input terminated the cable and provided 300 millivolts of forward bias. This was necessary because the 15 ns pulses were attenuated much more by the cable than was the DC level from the ECL output of the sense amplifier. The pre-trigger initiated the event gate and the train of 31 clock pulses. The digitizers accepted signals only for the duration of the event gate.

The signal was processed first by a Time Quantizer[3] which produced at its output the first clock pulse following the rising edge of the signal. This allowed all of the subsequent electronics to be designed for synchronized signals. Each Time Quantizer was constructed of two 10131 master-slave D-type flip-flops.[4] The outputs of the 8 time quantizers passed via an 8-way OR to a shift register which had its serial data input tied high. The first signal to be received therefore caused the output Q_0 of the shift register to go high and this, in turn, latched the pattern of signals in that time bin and stopped the first scaler. The next signal from the 8-way OR caused Q_1 of the shift register to go high, latching the pattern of signals in that time bin and stopping the second scaler, etc. The shift register was a Fairchild 10000, the scalers were Fairchild 10016's with the fifth bit provided by a flip-flop driven by the 10016's fourth bit. The latches were 10153's. Not shown on the diagram is the delay in the signals between the Time Quantizers and the latches needed to synchronize them with levels from the shift register. Note that up to 4 of the 31 time bins may be occupied, and that any pattern of signals on the 8 inputs within a time bin is recorded, with one bit per channel. The track efficiency of this system is given by the formula:

$$\varepsilon = \left(\sum_{j=0}^{t} \frac{n!}{(n-j)!\,j!} \exp\left(-\frac{n(n-1)}{mp}\right) \left(1-\exp\left[-\frac{n}{mp}\right]\right)^{j} \right)^{\frac{p}{n}}$$

where m = the number of active time bins = 21
p = the number of boards per chamber = 7
t = the number of time slots per board = 4
n = the number of tracks per chamber.

For n = 6, the efficiency is 0.9985 for recording each track. The efficiency for recording 3 of the 6 tracks (assuming 3 are background) is 0.995. The boards were originally designed for a clock frequency of 150 MHz and all were successfully tested at that frequency. When the experiment was set up, however, difficulties with the clock fanout required the reduction to 120 MHz, so that the drift time for the major portion of the cell covered only 21 time bins.

This formula for the efficiency assumes that the tracks are distributed statistically over the entire chamber. This, of course, was not the case - more than half of them were in the beam region. To avoid an overload of the digitizers connected to the cells in the beam region, a "matrix box" was inserted between the sense amplifiers and the digitizers. This transposed the matrix of eight amplifier modules each with seven outputs to connect to seven digitizers each with eight inputs. Thus the first digitizer board was connected to the first, eighth, fifteenth, ... cells, the second digitizer board to the second, ninth, ... cells, etc. The intense beam region was therefore distributed over all of the digitizer boards.

In addition to the logic shown on the diagram, overflows were recorded if more than 4 time bins were occupied. The ECL levels from the counters and latches were converted to TTL and were read out serially into a FIFO register, with empty data words suppressed. This serial readout occurred while the CAMAC system was reading data from other parts of the experiment so that no additional time was lost. The FIFO was read out by the CAMAC system.

The digitizers were constructed on Multiwire[5] circuit boards. The conductors on these boards are #34 AWG insulated copper wires which are laid by a computer-controlled machine in a layer of epoxy which covers a copper-clad G-10 printed circuit board. If the copper layer forms a continuous ground plane (interrupted only by small holes) then these conductors form good 50-ohm transmission lines. There was no difficulty transmitting the 150 MHz clock train on these boards. The advantage of this construction is that the conductors may cross without detectable cross-talk. The layout is therefore very much simpler than that of a printed circuit board. There is some cross-talk if conductors have long runs at the minimum (0.05 inch) spacing, but this is easily avoided. In the layout of the digitizers, care was required to match the path lengths to keep the signals synchronized. No difficulty has been observed, however, due to lack of synchronization in the production boards.

The boards were mounted in crates which served two chambers each. The seven data-boards for each chamber generated 16-bit data words, each of which had embedded in it a 3-bit board address. A chamber-address board for each chamber generated a word containing chamber number and overflow bits. This word was distinguished from data by an "illegal" board address bit pattern. The fanout of the clock and event gate for the seven boards in each chamber group was also performed on the chamber address board.

The principal difficulty with this system during the experiment was with the miniature coaxial cable connectors used for the clock. When there was an indication of trouble, it usually could be fixed by wiggling the cables.

System Performance

The operating sense wire voltage for the drift chambers was chosen after investigating the voltage dependence of both the efficiency and the resolution. The efficiency, measured with cosmic rays and a plastic scintillator telescope, typically plateaued below +1550 volts. The resolution, measured in a small test chamber, did not reach its plateau until about +1700 volts. At this voltage, the amplification at the sense wire presumably was great enough to place the signal from a single electron above the sense amplifier-discriminator threshold. During the first part of the experiment, the chambers were operated at +1800 volts. Later this was reduced to +1700 volts to decrease the signal size into the sense amplifiers, possibly reducing slightly their dead time. The effect on the resolution and efficiency was negligible.

The relationship between drift time and drift distance is shown in Fig. 6. The straight line is for reference only, to guide the eye. The 31 points were obtained by integrating the population vs time bin histogram from a low intensity run with straight-through triggers. The average illumination of the cells was expected to be extremely uniform over the drift space. The histogram had a tail which extended out to time bin 31 although most of the hits fell in time bins 3 through 23. This tail produced the asymptotic approach of the points to the maximum drift distance. That this was the correct interpretation was established by fitting data from beam tracks in five adjacent chambers with a parabola. Even small deviations from this relationship worsened the χ^2 of the fit.

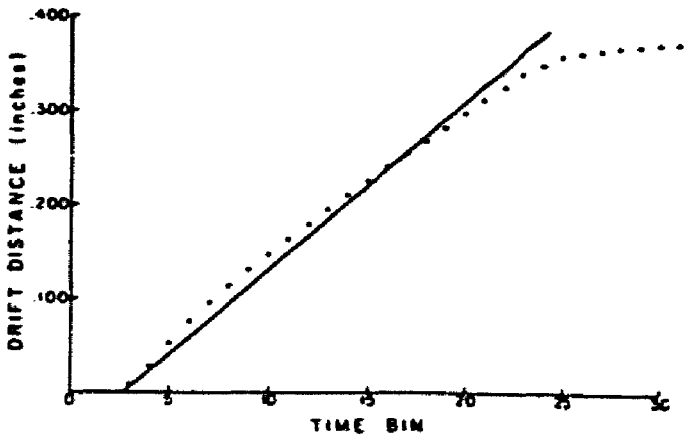

Fig. 6. Graph of Drift Distance vs Time Bin Number

This asymptotic approach to the maximum drift distance is believed to be due to the fact that electrons from tracks close to the cell edge wire, if not released exactly on the mid plane, have significantly longer drift distances along the curved electric field lines. There is probably some worsening of the resolution in this region. The nonlinearity is taken care of in the track programs by simply using a look-up table containing 31 entries per chamber group. Because of some cable length differences, there are three groups of chambers. The average drift speed is 18 mils per time bin, or about 5.5 cm/μsec.

The resolution of the drift chambers while in place in the spectrometer was checked by the aforementioned fitting program. Since it was expected that there might be some chamber construction errors, the chamber resolution assumed in the program was double that expected from the width of the time bins, or 10 mils (250 microns). The multiple scattering in the iron was put in carefully, including the correlations between the scattering offsets in adjacent chambers. The resulting χ^2 distributions were narrower than that theoretically expected, but with a considerable tail. This is interpreted as showing that the chambers had close to their ideal resolution. The tail is believed to be due to delta rays which happen to produce ions closer to the sense wire than the muon track. The trackfinding program now in use in the analysis of the experiment, which fits to both the drift chambers and the multiwire proportional chambers, gives a residual distribution for the drift chambers with a width of about 860 microns. This is largely due to multiple scattering in the iron.

The chamber hit efficiency, measured with non-interacting beam muons, averaged better than 98.5%. This efficiency was calculated from data taken three quarters of the way through the experiment's run with a muon beam containing about 5.5×10^6 muons per spill with additional muons in the halo. The full width at half maximum of this beam was ten drift cells.

The noise rate for the OR of all 56 channels in a chamber was typically 4 kHz. The rate expected from cosmic rays was about 1 kHz. No dark current was observed up to +2100 volts on the sense wire during these tests. After the chambers were installed in the

spectrometer, none had a dark current above 300 pA, the minimum observable. At the end of the experiment, after a total of 4×10^{11} muons had passed through the spectrometer with an average intensity of 5×10^{6} beam muons per pulse, the dark current drawn by one chamber was intermittently up to 1 μA, while all of the othrs remained unobservable. This should be compared with the 80 μA drawn by each chamber while the beam was passing through the apparatus. Neither the chamber efficiency nor the resolution were observed to change appreciably over the course of the experiment.

Acknowledgements

We wish to thank our collaborators on this experiment, the members of the Lawrence Berkeley Laboratory and Fermilab groups, for their assistance and support. The construction of the chambers and the electronic systems were ably performed by members of our technical support group. We wish to thank A. Mike Malling for his help during the early parts of the development and installation of the equipment.

References

1. F. Sauli, "Comments on Some Proposed Schemes for Drift Chamber Electronics", CERN NP Internal Report 73-12 (Rev.) (1973).

2. G. Charpak, F. Sauli and W. Duinker, "High-Accuracy Drift Chambers and Their Use in Strong Magnetic Fields", Nucl. Instr. and Meth., 108, 413-426 (1973).

3. I. Piser, "A Multi-Channel Time Recorder", NP Internal Report 73-14 (1973).

4. Suggested by A. R. Clark, Private Communication.

5. Manufactured by Photocircuits Division, Kollmorgen Corp., Glen Cove, N.Y.

APPENDIX B

THE TURBO-ENCABULATOR*

For a number of years work has been proceeding in order to bring to perfection the crudely-conceived idea of a machine that would not only supply inverse reactive current for use in unilateral phase detractors, but would also be capable of automatically synchronizing cardinal grammeters. Such a machine is the "Turbo-Encabulator." The only new principle involved is that instead of power being generated by the relative motion of conductors and fluxes, it is produced by the modial interaction of magnetoreluctance and capacitive directance.

The original machine had a base-plate of prefabulated amulite, surmounted by a malleable quasiboscular casing in such a way that the two spurving bearings were in a direct line with the pentametric fan. The latter consisted simply of six hydrocoptic marzlevanes, so fitted to the ambifacient lunar waneshaft that side fumbling was effectively prevented. The main winding was of normal lotus-O-delta type placed in panendermic semi-boloid slots in the stator, every seventh conductor being connected by a non-reversible

tremic pipe to the differential girdle spring on the up end of the grammeters.

Forty-one manestically spaced grouting brushes were arranged to feed into the rotor slip-stream a mixture of high S-value phenylhydrobenzamine and five per cent reminative tetraliodohexamine. Both of these liquids have specific periosities of 2.5Cn where n is the diathetical evolute of retrograde kinetic phase disposition and C is Cholmondoley's annular grillage coefficient. Initially, n was measured with the aid of a metapolar refractive pelfrometer (for a description of this ingenious instrument see L. F. Rumpelverstein, Z. Electrotechnischtratishce-donnerblitze III, 212 (1929)), but up to the present date nothing has been found to equal the transcending missive dadoscope. (See H. Feducci et al., Proc. Peruv. Acad. Scat. Sci. 43, 187 (1979)).

Mechanical engineers will appreciate the difficulty of nubing together a metahesive purwell and a superamitive wannelsprocket. Indeed this proved to be a stumbling block to further development until, in 1952, it was found that the use of anhydrous nagling pins enabled a dryptonastic boiling shim to be tankered to the bendyles.

The early attempts to construct a sufficiently stable spiral decommutator failed largely because of a lack of appreciation of the large quasi-piestic stress in the sembling studs; the latter were specifically designed to

hold the tremic pipes to the spanshaft. When, however, it was discovered that wending could be prevented by a simple recession of the lipping sockets, almost perfect running was secured.

The operating point is maintained as near as possible to the h.f. rem. peak by constantly fretting the anthragenous spandrels. This is a distinct advance on the standard nivelsheave in that no additional dramcock oil is required after the phase detractors have remissed.

Undoubtedly, the Turbo-Encabulator has now reached a very high level of technical development. It has been shown that it may successfully be used for encabulating nofer trunnions. In addition, whenever a barescent skor motion is required, it may be employed in conjunction with a drawn reciprocating dingle arm to reduce sinusoidal depleneration. The future promises frogs, dogs, and television sets.

*Based on a lecture delivered to Physics 1 by P.G. Bamberg, Jr., Harvard University, Cambridge, Massachusetts, 1974.

REFERENCES

1. E. Fermi and C. N. Yang, Phys. Rev. 76, 1739 (1949).

2. S. Sakata, Prog. Theor. Phys. 16, 686 (1956).

3. K. Matumoto, Prog. Theor. Phys. 16, 583 (1956).

4. See, for example, M. Gell-Mann, Phys Rev. 125, 1067 (1962).

5. M. Gell-Mann, Phys. Lett. 8, 214 (1964).

6. O. W. Greenberg, Phys. Rev. Lett. 13, 598 (1964).

7. S. D. Drell and T.-M. Yan, Phys. Rev. Lett. 25, 316 (1970).

8. See, for example, K. J. Anderson et al., Phys. Rev. Lett. 42, 944 (1979).

9. B. J. Bjorken and S. L. Glashow, Phys. Lett. 11, 255 (1964).

10. S. L. Glashow, J. Iliopoulos, and L. Maiani, Phys. Rev. D2, 1285 (1970).

11. J. J. Aubert et al., Phys. Rev. Lett. 33, 1404 (1974); J.-E. Augustin et al., Phys. Rev. Lett. 33, 1406 (1974).

12. G. Goldhaber et al., Phys. Rev. Lett. 37, 255 (1976); I. Peruzzi et al., Phys. Rev. Lett. 37, 569 (1976).

13. G. J. Feldman et al., Phys. Rev. Lett. 38, 1313 (1977).

14. R. Brandelik et al., Z. Physik C1, 233 (1979).

15. See, for example, J. Kirkby in Proc. IX Int. Symp. on Lepton and Photon Interactions at High Energy (Batavia, 1979).

16. J. P. Leveille, University of Wisconsin Report No. COO-881-120 (1979).

17. See, for example, J. P. Leveille and T. Weiler,

Nucl. Phys. B147, 147 (1979), and references cited therin.

18. A.R. Clark et al., Phys. Rev. Lett. 45, 682 (1980).

19. A.R. Clark et al., Lawrence Berkeley Laboratory Report No. LBL- 10879 (to be published).

20. B.A. Gordon et al., Phys. Rev. D20, 2645 (1979).

21. G. Gollin et al., IEEE Trans. Nuc. Sci. NS-26, 59 (1979).

22. V. Barger, W. Y. Keung, and R. J. N. Phillips, Phys. Lett. 91B, 253 (1980).

23. A. R. Clark et al., Phys. Rev. Lett. 43, 187 (1979).

24. W. R. Ditzler et al., Phys. Lett. 57B, 201 (1975).

25. See, for example, A. Silverman, in Proc. Int. Symp. on Electron and Photon Interactions at High Energies (Daresbury, 1969), Table 2.

26. P. A. Rapidis et al., Phys. Lett. 84B, 507 (1979).

27. The decay matrix elements of I. Hinchcliffe and C. H. Llewellyn Smith, Nucl. Phys. B114, 45 (1976) are used to describe D decay.

28. J. Kirkby in Proc. IX Int. Symp. on Lepton and Photon Interactions at High Energy (Batavia, 1979); M. Coles, private communication. Our experiment measures the product of the cross section and the average yield of muons.

29. W.A. Loomis et al., Phys. Rev. D19, 2543 (1979).

30. J. Proudfoot, Ph.D. Thesis, University of Oxford, 1978 (unpublished).

31. P. Bosetti et al., Nucl. Phys. B54, 141 (1973).

32. P. Bosetti et al., Nucl. Phys. B60, 307 (1973).

33. G.A. Akopdjanov et al., Nucl. Phys. B75, 401 (1974).

34. W. Morris et al., Phys. Lett. 56B, 395 (1975).

35. E.L. Berger et al., Nucl. Phys. B77, 365 (1974).

36. V.V. Ammosov et al., Nucl. Phys. B58, 77 (1973).

37. S.L. Stone et al., Nucl. Phys. B32, 19 (1971).

38. R. Barloutaud et al., Sov. J. Nucl. Phys., 24, 303 (1976).

39. A. Bialas in Proc. First Workshop on Ultrarelativistic Nuclear Collisions, Lawrence Berkeley Laboratory Report No. LBL-8957 (1979).

40. A. Bialas and E. Bialas, Phys. Rev. D21, 675 (1980).

41. S.P. Denisov et al., Phys. Lett. 36B, 415 (1971).

42. S.P. Denisov et al., Nucl. Phys. B65, 1 (1973).

43. A.S. Carroll et al., Phys. Rev. Lett. 33, 932 (1974).

44. W. Galbraith et al., Phys. Rev. 138, 913 (1965).

45. J.E. Elias et al., Fermilab Report No. FERMILAB-Pub- 79/47-EXP 7185.178 (1979).

46. J.A. Gaidos et al., Nucl. Phys. B32, 10 (1971).

47. S.C. Loken, private communication. The correction is a hand fit to SLAC data comparing electron-neutron and electron-proton scattering.

48. D.H. Perkins, Introduction to High Energy Physics, Addison-Wesley, Reading, Massachusetts, 1972, p. 40.

49. M. Shaevitz, private communication. Prompt muons from hadronic showers contribute less than 10% of the total muon yield.

50. W.A. Loomis, private communication.

51. C. Bricman et al., Review of Particle Properties, Lawrence Berkeley Laboratory, Berkeley, 1978, p. 34.

52. See, for example, J.F. Martin et al., Phys. Rev. D20, 5 (1979). This experiment used 20.5 GeV electrons at SLAC.

53. M. Shaevitz, private communication.

54. See, for example, R.D. Field and R.P. Feynman, Phys. Rev. D15, 2590 (1977).

55. V. Barger, W.Y. Keung, and R.J.N. Phillips, Phys. Rev. D20, 630 (1979).

56. A.R. Clark et al., Phys. Rev. Lett. 45, 686 (1980).

57. D. Bauer et al., Phys. Rev. Lett. 43, 1551 (1979).

58. The MSF model is similar to that of F. Bletzacker, H.T. Nieh, and A. Soni, Phys. Rev. Lett. 37, 1316 (1976).

59. C. Chang et al., Phys. Rev. Lett. 39, 519 (1977).

60. J.D. Jackson, Classical Electrodynamics, John Wiley and Sons, New York, 1962, p. 520.

61. F.J. Gilman, Phys. Rev. 167,1365 (1968). The more familiar form for Γ_T is from L.N. Hand, Phys. Rev. 129, 1834 (1963); Hand's flux is $(1-x)/(1+Q^2/\nu^2)^{1/2}$ times Gilman's. Values of $x=Q^2/(2M\nu)$ range from about .001 to .1 in the data presented here.

62. M.S. Atiya et al., Phys. Rev. Lett. 43, 414 (1979).

63. P. Avery et al., Phys. Rev. Lett. 44, 1309 (1980).

64. D.O. Caldwell et al., Phys. Rev. Lett. 42, 533 (1979).

65. D.O. Caldwell et al., Phys. Rev. Lett. 40, 1222 (1978).

66. F. Bletzacker and H.T. Nieh, SUNY-Stony Brook Report No. ITP-SB-77-44 (unpublished).

67. Y. Watanabe et al., Phys. Rev. Lett. 35, 898 (1975); C. Chang et al., Phys. Rev. Lett. 35, 901 (1975).

68. T. Weiler, "Photon-Gluon Fusion and Diffractive and

Non-diffractive ψ-Leptoproduction," presented at XX International Conference on High Energy Physics, Madison, Wisconsin, 1980.

69. J. J. Aubert et al., CERN Report No. CERN- EP/80-62, 1980.

70. S. Okubo, Phys. Lett. 5, 160 (1963); G. Zweig, report, 1964 (unpublished); J. Iizuka, Prog. Theor. Phys. Suppl. 37-38, 21 (1966).

71. D. Sivers, J. Townsend, and G. West, Phys. Rev. D3, 1234, (1976).

TABLE 1

Calorimeter and hodoscope subtrigger combinations resulting in a full dimuon trigger. Cluster 1 includes calorimeter counters in modules 1 and 2, cluster 2 includes modules 2 and 3, etc. as described in the text. Hodoscope group 1 includes trigger banks 1, 2, and 3, placed after modules 4, 6, and 8, group 2 includes trigger banks 2, 3, and 4 after modules 6, 8, 10, etc.

Calorimeter cluster with subtrigger	Required hodoscope groups with subtrigger
1 (and any others downstream)	any of 1-6
2 (and any others downstream)	any of 2-6
3 (and any others downstream)	any of 3-6
4 (and any others downstream)	any of 4-6
5 (and 6 if present)	5 or 6
6	6

TABLE 2

Mean values of six reconstructed kinematic quantities for data before background subtraction, for charm Monte Carlo, and for π, K-decay Monte Carlo. All events have E(daughter μ) > 15 GeV, ν > 75 GeV, and satisfy the standard analysis cuts described in chapter III. Statistical errors are shown.

Reconstructed kinematic quantity	Data	Monte Carlo Charm	Monte Carlo π, K
$\langle\nu\rangle$ (GeV)	132.2 $\pm$0.2	136.1 $\pm$0.3	120.4 $\pm$1.0
Geometric mean Q^2 $(GeV/c)^2$	0.547 $\pm$0.004	0.729 $\pm$0.006	0.260 $\pm$0.011
$\langle$Daughter μ energy$\rangle$ (GeV)	26.02 $\pm$0.07	26.35 $\pm$0.08	23.58 $\pm$0.21
$\langle$Inelasticity$\rangle$	0.794 $\pm$0.001	0.800 $\pm$0.001	0.793 $\pm$0.003
$\langle$Missing energy$\rangle$ (GeV)	15.65 $\pm$0.14	14.59 $\pm$0.18	4.45 $\pm$0.53
$\langle p(\text{daughter})_{\perp}$ to $\vec{\nu}\rangle$ (GeV/c)	0.749 $\pm$0.003	0.676 $\pm$0.003	0.618 $\pm$0.008

TABLE 3

Effects of charmed quark fragmentation on daughter energy and acceptance. To increase sensitivity to the choice of fragmentation function D(z), mean daughter energies are shown for νGF Monte Carlo events with $\nu > 150$ GeV.

D(z)	$\langle E(\text{daughter } \mu) \rangle$	Relative acceptance
$(1-z)^{0.4}$	28.31 ± 0.15	1.00
$(1-z)^{3}$	26.94	0.81
$(1-z)^{-1.5}$ $(z < 0.99)$	29.78	1.20
Subtracted data	28.20 ± 0.20	

TABLE 4

The Q^2 dependence of the virtual photoproduction cross section for charm. Results are presented for two values of average ν. Errors are statistical.

Q^2 (GeV^2/c^2)	σ_{eff} ($\gamma_\nu N \rightarrow c\bar{c}X$) (nb)	
	$\langle\nu\rangle$=100 GeV	$\langle\nu\rangle$=178 GeV
0.075	467.3 ± 24.7	627.1 ± 53.1
0.133	518.6 ± 29.7	628.7 ± 55.1
0.237	498.3 ± 31.8	687.7 ± 47.6
0.422	556.7 ± 45.4	720.7 ± 41.5
0.750	517.5 ± 31.0	698.5 ± 28.8
1.33	444.3 ± 26.4	588.8 ± 41.0
2.37	371.4 ± 23.4	488.0 ± 19.6
4.22	219.4 ± 18.5	378.7 ± 20.8
7.50	149.0 ± 14.1	274.8 ± 16.8
13.3	86.12 ± 8.63	149.8 ± 12.5
23.7	30.76 ± 5.43	68.50 ± 9.63
42.2	7.94 ± 2.96	19.97 ± 6.04

TABLE 5

The ν dependence of the virtual photoproduction cross section for charm in the range $.32 < Q^2 < 1.8$ $(GeV/c)^2$. The first error shown is statistical, the second systematic.

ν (GeV)	σ_{eff} $(\gamma_v N \rightarrow c\bar{c}X)$ (nb)
60.4	$378.8 \pm 162.6 \; {}^{+289.}_{-291.}$
69.8	$393.9 \pm 102.0 \; {}^{+189.}_{-187.}$
80.6	$408.7 \pm 53.31 \; {}^{+112.}_{-106.}$
93.1	$424.4 \pm 40.56 \; {}^{+65.}_{-76.}$
107.	$631.8 \pm 41.53 \; {}^{+36.}_{-30.}$
124.	$559.0 \pm 27.31 \; {}^{+61.}_{-14.}$
143.	$606.7 \pm 29.51 \; {}^{+97.}_{-34.}$
165.	$641.1 \pm 30.67 \; {}^{+130.}_{-49.}$
191.	$693.1 \pm 44.68 \; {}^{+162.}_{-60.}$

TABLE 6

The Q^2 dependence of the charm structure function $F_2(c\bar{c})$ for two values of average ν. The first error shown is statistical, the second systematic.

Q^2 $(GeV/c)^2$	$F_2(c\bar{c})$ $\langle\nu\rangle$=100 GeV	$\langle\nu\rangle$=178 GeV
0.075	$(3.002 \pm 0.159\ ^{+0.451}_{-0.631})\times10^{-4}$	$(3.516 \pm 0.297\ ^{+0.291}_{-0.222})\times10^{-4}$
0.133	$(6.117 \pm 0.351\ ^{+0.513}_{-0.513})\times10^{-4}$	$(7.221 \pm 0.633\ ^{+0.778}_{-0.888})\times10^{-4}$
0.237	$(10.69 \pm 0.683\ ^{+0.641}_{-1.20})\times10^{-4}$	$(15.48 \pm 1.07\ ^{+2.28}_{-1.15})\times10^{-4}$
0.422	$(21.60 \pm 1.76\ ^{+2.48}_{-3.07})\times10^{-4}$	$(30.99 \pm 1.78\ ^{+1.21}_{-2.11})\times10^{-4}$
0.750	$(36.08 \pm 2.16\ ^{+2.86}_{-4.95})\times10^{-4}$	$(55.89 \pm 2.30\ ^{+2.65}_{-4.55})\times10^{-4}$
1.33	$(55.27 \pm 3.28\ ^{+3.24}_{-3.50})\times10^{-4}$	$(84.93 \pm 5.91\ ^{+4.38}_{-7.00})\times10^{-4}$
2.37	$(81.86 \pm 5.16\ ^{+10.4}_{-3.83})\times10^{-4}$	$(123.1 \pm 4.93\ ^{+7.48}_{-3.40})\times10^{-4}$
4.22	$(85.32 \pm 7.21\ ^{+8.26}_{-19.2})\times10^{-4}$	$(163.9 \pm 9.01\ ^{+7.53}_{-17.3})\times10^{-4}$
7.50	$(102.0 \pm 9.62\ ^{+6.08}_{-10.5})\times10^{-4}$	$(203.0 \pm 12.4\ ^{+12.2}_{-8.01})\times10^{-4}$
13.3	$(104.0 \pm 10.4\ ^{+14.0}_{-7.10})\times10^{-4}$	$(190.1 \pm 15.9\ ^{+17.0}_{-22.2})\times10^{-4}$
23.7	$(65.60 \pm 11.6\ ^{+2.76}_{-28.4})\times10^{-4}$	$(150.6 \pm 21.2\ ^{+5.17}_{-5.20})\times10^{-4}$
42.2	$(29.94 \pm 11.2\ ^{+1.17}_{-1.71})\times10^{-4}$	$(76.78 \pm 23.2\ ^{+23.7}_{-11.9})\times10^{-4}$

TABLE 7

Calculated $10^4 d F_2 / d \ln Q^2$ at fixed Bjorken x vs. ν (top), Q^2 (left margin), and x (diagonals, right margin). For each Q^2-ν combination, two values are shown. The bottom value is fit to the structure function F_2 for muon-nucleon scattering (Ref. 20). The top value is the contribution $F_2(c\bar{c})$ to F_2 from diffractive muoproduction of bound and unbound charmed quarks.

ν(GeV)	27	42	67	106	168	
Q^2 $(GeV/c)^2$	$10^4 \partial F_2(c\bar{c})/\partial \ell n Q^2$ / $10^4 \partial F_2(\mu N)/\partial \ell n Q^2$					x
0.63	17 / 1070	30 / 1090	43 / 1110	54 / 1120	58 / 1130	
1.0	23 / 980	43 / 1010	63 / 1040	77 / 1050	84 / 1060	0.002
1.6	30 / 650	59 / 680	87 / 700	107 / 720	116 / 730	0.003
2.5	36 / 310.	73 / 340	110 / 350	139 / 360	146 / 360	0.005
4.0	36 / 320	80 / 390	128 / 430	162 / 460	163 / 480	0.008
6.3	29 / 210	75 / 330	128 / 410	165 / 460	154 / 490	0.013
10	15 / 50	54 / 220	104 / 340	138 / 430	112 / 480	0.020
16	4 / -130	27 / 50	64 / 230	90 / 360	52 / 440	0.032
25	-2 / -189	7 / -126	26 / 50	40 / 230	0 / 370	0.050
40	0 / -31	-1 / -171	6 / -122	10 / 50	-22 / 240	0.080
63		0 / -23	1 / -154	1 / -119	-16 / 50	0.130

Figure 1.-- Drell-Yan production of muon pairs through quark-antiquark annihilation.

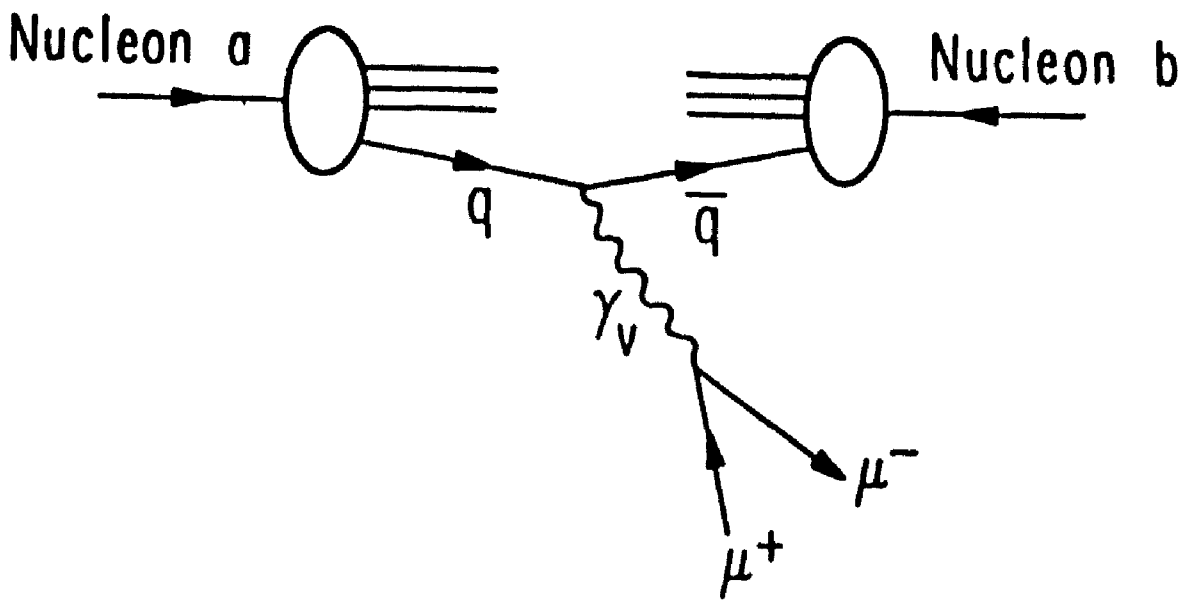

Figure 1.

Figure 2.-- Models for charmed particle production. (a) charmed sea production; (b) vector-meson dominance production; (c) virtual photon-gluon-fusion production.

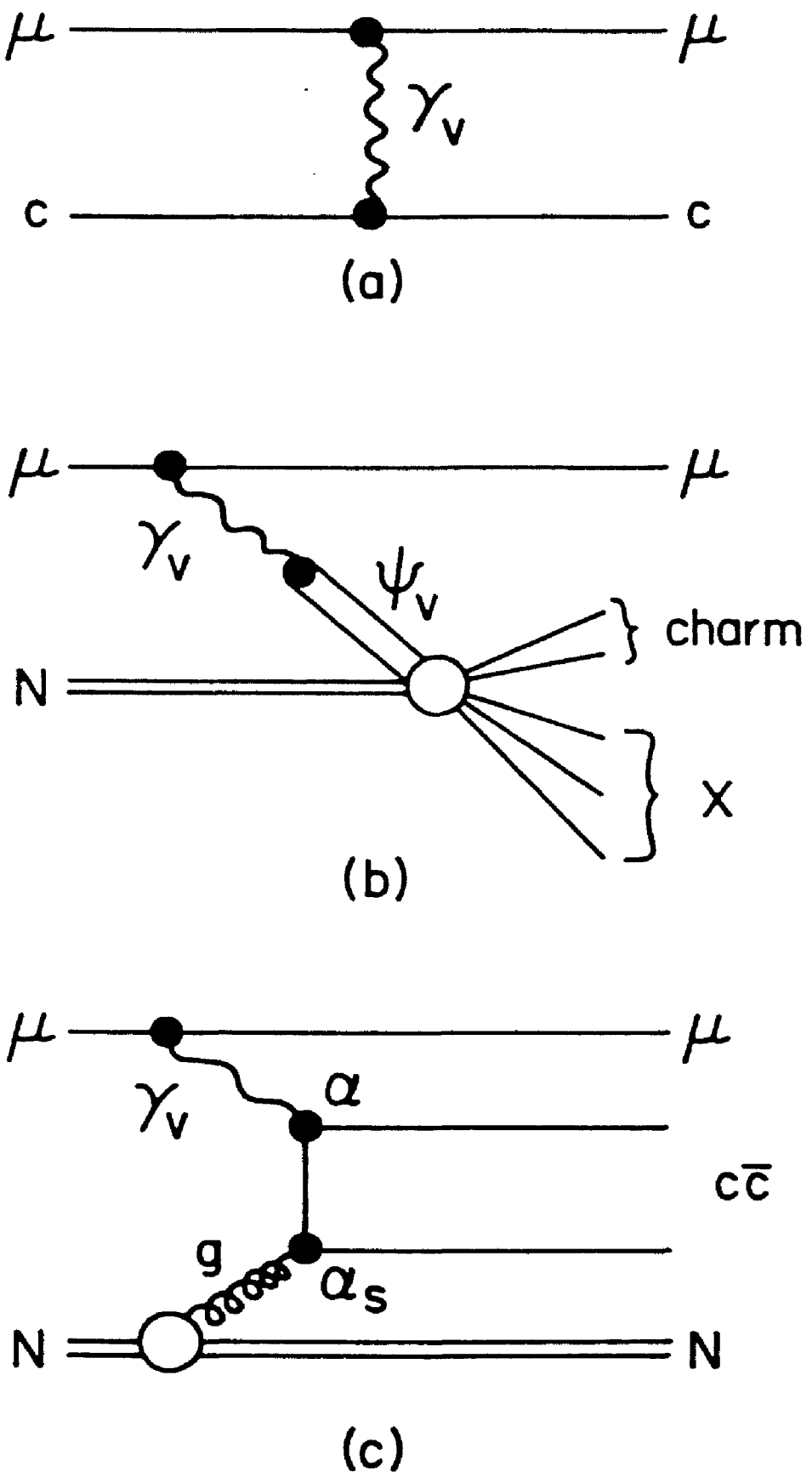

Figure 2.

Figure 3.-- The N1 beam line at Fermilab. North is towards the bottom of the page and west is towards the right. Magnets D1 and Q2 are in enclosure 100, Q3 and D2 in enclosure 101, and D3 in enclosure 102. Q4 is in enclosure 103 and D4 is in enclosure 104.

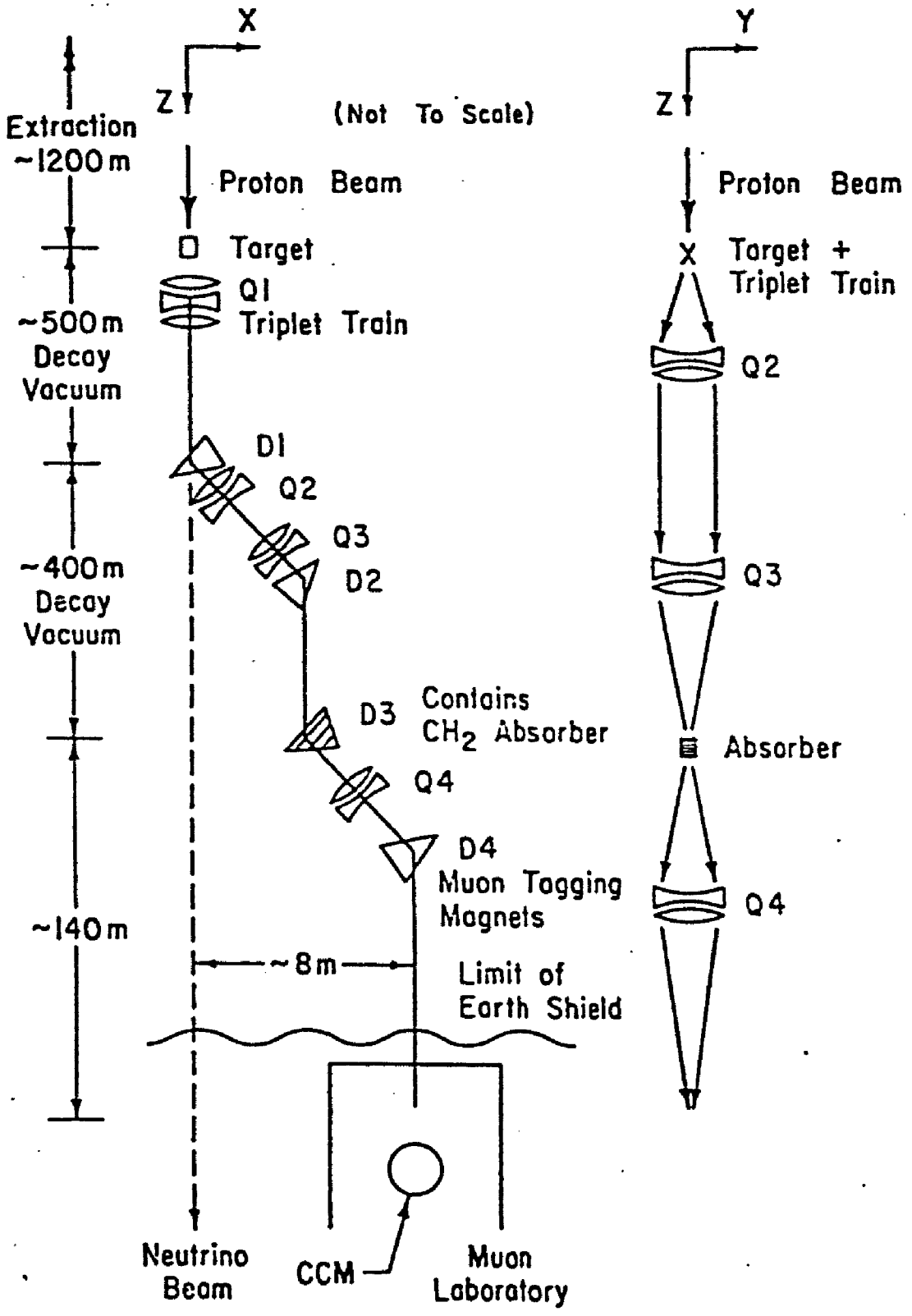
X
Z
(Not To Scale)
Y
Z
Extraction
~1200m
Proton Beam
Target
Q1
Triplet Train
Proton Beam
X Target +
Triplet Train
~500m
Decay
Vacuum
Q2
D1
Q2
Q3
D2
Q3
~400m
Decay
Vacuum
D3
Contains
CH_2 Absorber
Absorber
Q4
D4
Muon Tagging
Magnets
Q4
~140m
~8m
Limit of
Earth Shield
Neutrino
Beam
CCM
Muon
Laboratory

Figure 3.

Figure 4.-- Multiwire proportional chambers and scintillation counters in the muon beam.

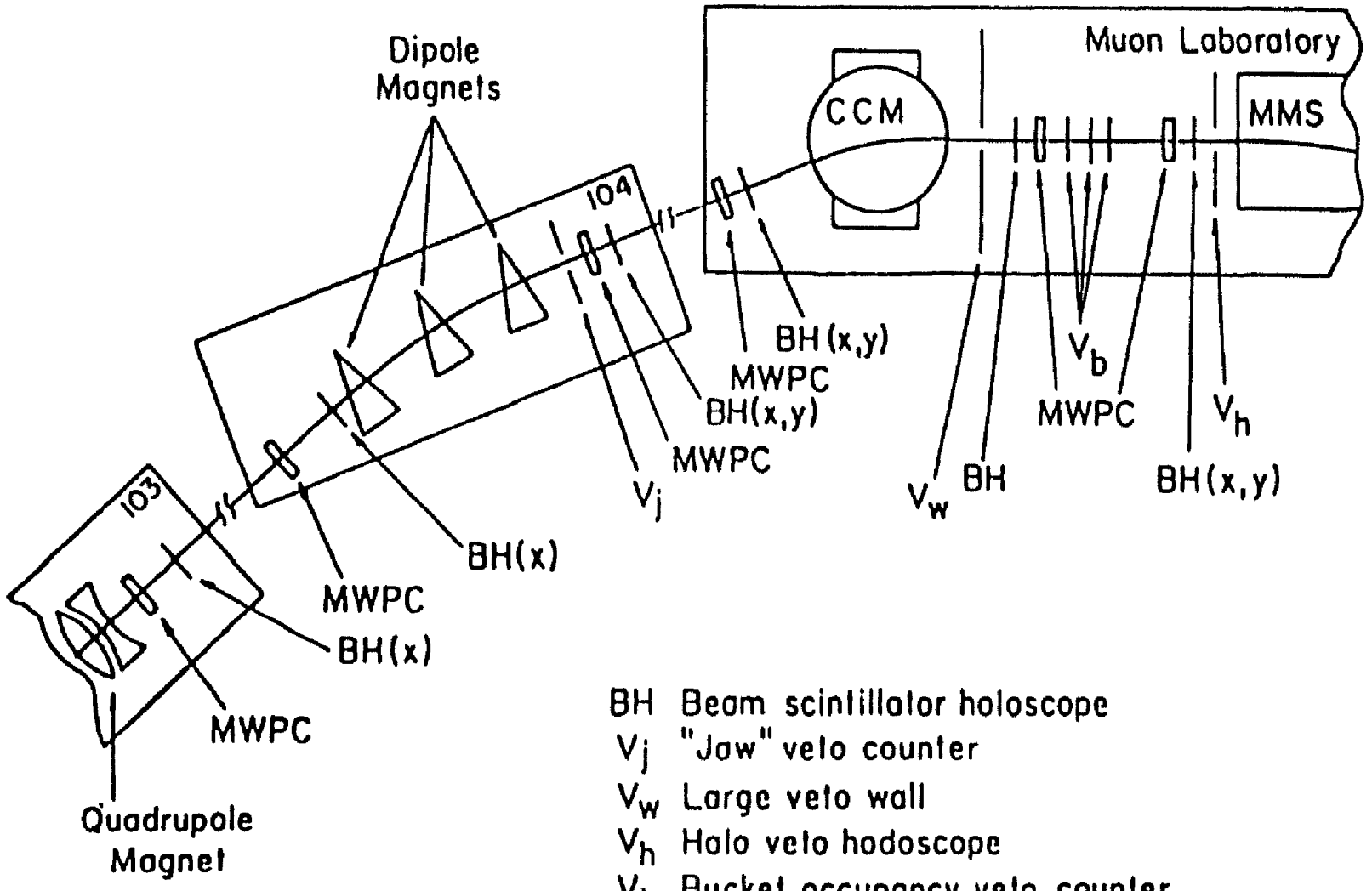

BH Beam scintillator holoscope
V_j "Jaw" velo counter
V_w Large velo wall
V_h Halo velo hodoscope
V_b Bucket occupancy velo counter
MMS Multimuon Spectrometer
CCM Chicago Cyclotron Magnet

Figure 4

Figure 5.-- The Multimuon Spectrometer. The magnet, serving also as target and hadron absorber, reaches 19.7 kGauss within a 1.8x1x16 m^3 fiducial volume. Over the central 1.4x1x16 m^3, the magnetic field is uniform to 3% and mapped to 0.2%. Eighteen pairs of multiwire proportional (MWPC) and drift chambers (DC), fully sensitive over 1.8x1 m^2, determine muon momenta typically to 8%. The MWPC's register coordinates at 30° and 90° to the bend direction by means of 0.2 inch cathode strips. Banks of trigger scintillators (S_1-S_{12}) occupy 8 of 18 magnet modules. Interleaved with the 4-inch thick magnet plates in modules 1-15 are 75 calorimeter scintillators resolving hadron energy E with rms uncertainty $1.5E^{1/2}$ (GeV). Not shown upstream of module 1 are one MWPC and DC, 63 beam scintillators, 8 beam MWPC's, and 94 scintillators sensitive to accidental beam and halo muons.

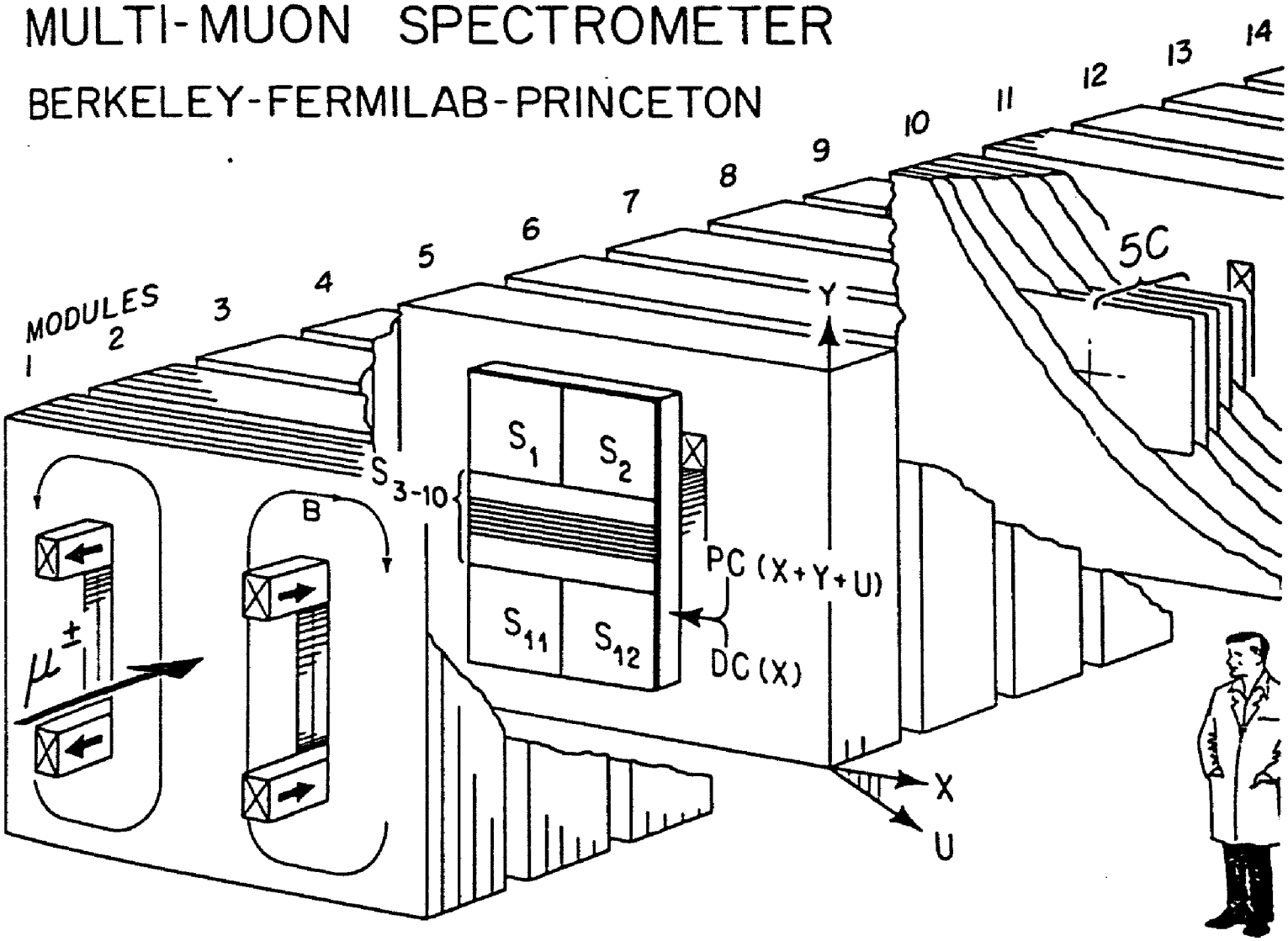

XBL 795-15:

Figure 5.

Figure 6.-- One module in the muon spectrometer.

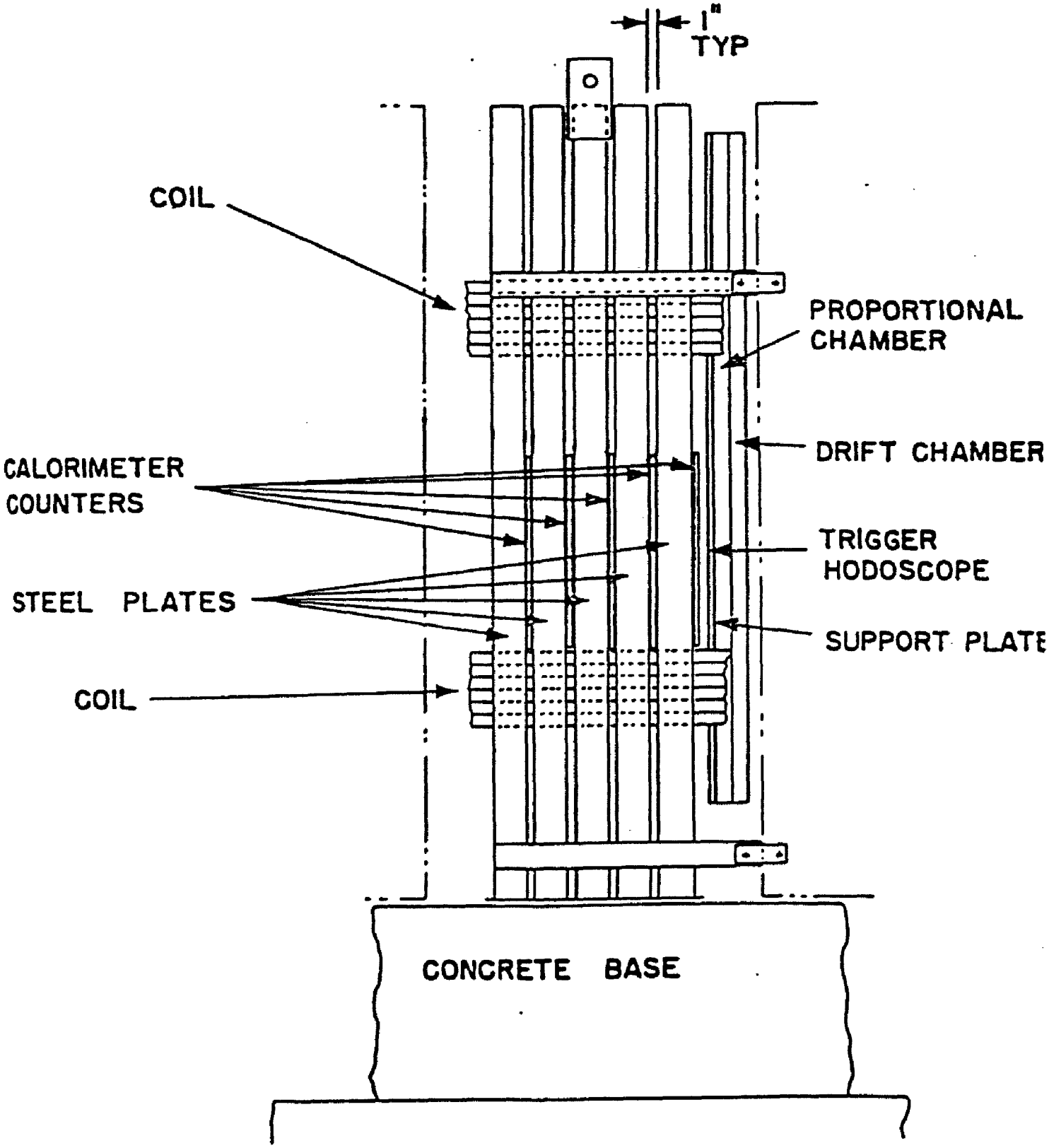
1"
TYP
COIL
PROPORTIONAL
CHAMBER
DRIFT CHAMBER
CALORIMETER
COUNTERS
TRIGGER
HODOSCOPE
STEEL PLATES
SUPPORT PLATE
COIL
CONCRETE BASE

Figure 6.

Figure 7.-- A trigger hodoscope. Counters S_1, S_2, S_{11}, and S_{12} are "paddles," 20.75 inches wide and 23.8 inches high. Counters S_3-S_{10} are "staves." S_3 and S_{10} are 41.5 inches wide and 5.98 inches high while S_4-S_9 are 41.5 inches wide and 1.55 inches high.

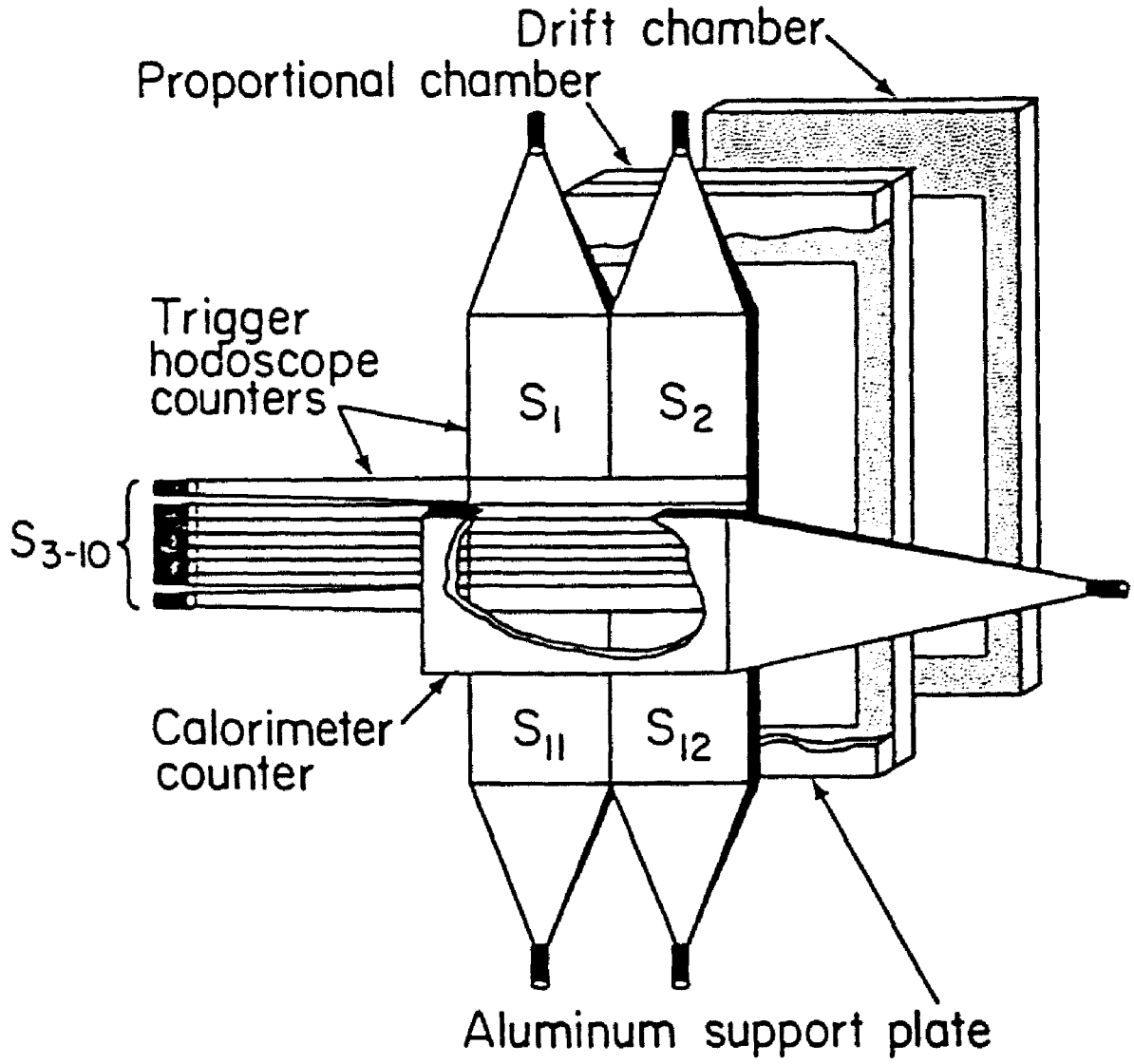
Drift chamber
Proportional chamber
Trigger
hodoscope
counters
S1
S2
S3-10
Calorimeter
counter
S11
S12
Aluminum support plate
XBL 795-1602

Figure 7.

Figure 8.-- Calorimeter subtrigger patterns for dimuon events. (a) cluster grouping of counters; (b) examples of subtriggers. Pulse heights in at least five of ten scintillators in a cluster must exceed a threshold for that cluster to satisfy a calorimeter subtrigger.

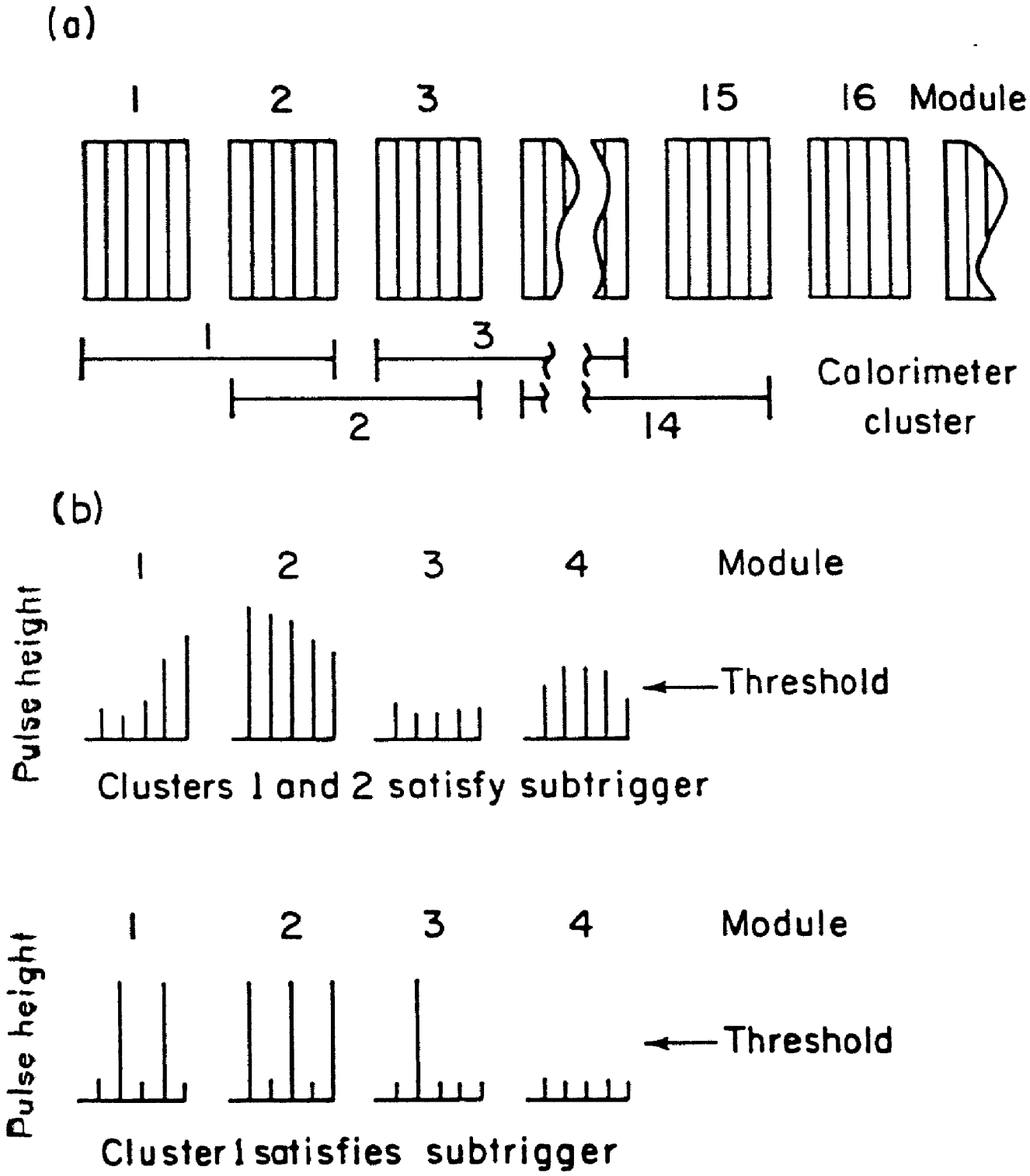
(a)
1
2
3
15
16
Module
1
3
2
14
Calorimeter cluster
(b)
1
2
3
4
Module
Pulse height
Threshold
Clusters 1 and 2 satisfy subtrigger
1
2
3
4
Module
Pulse height
Threshold
Cluster 1 satisfies subtrigger

Figure 8.

Figure 9.-- Trigger hodoscope subtrigger patterns for dimuon events: (a) typical subtrigger; (b) other possible combinations of hits in the third hodoscope.

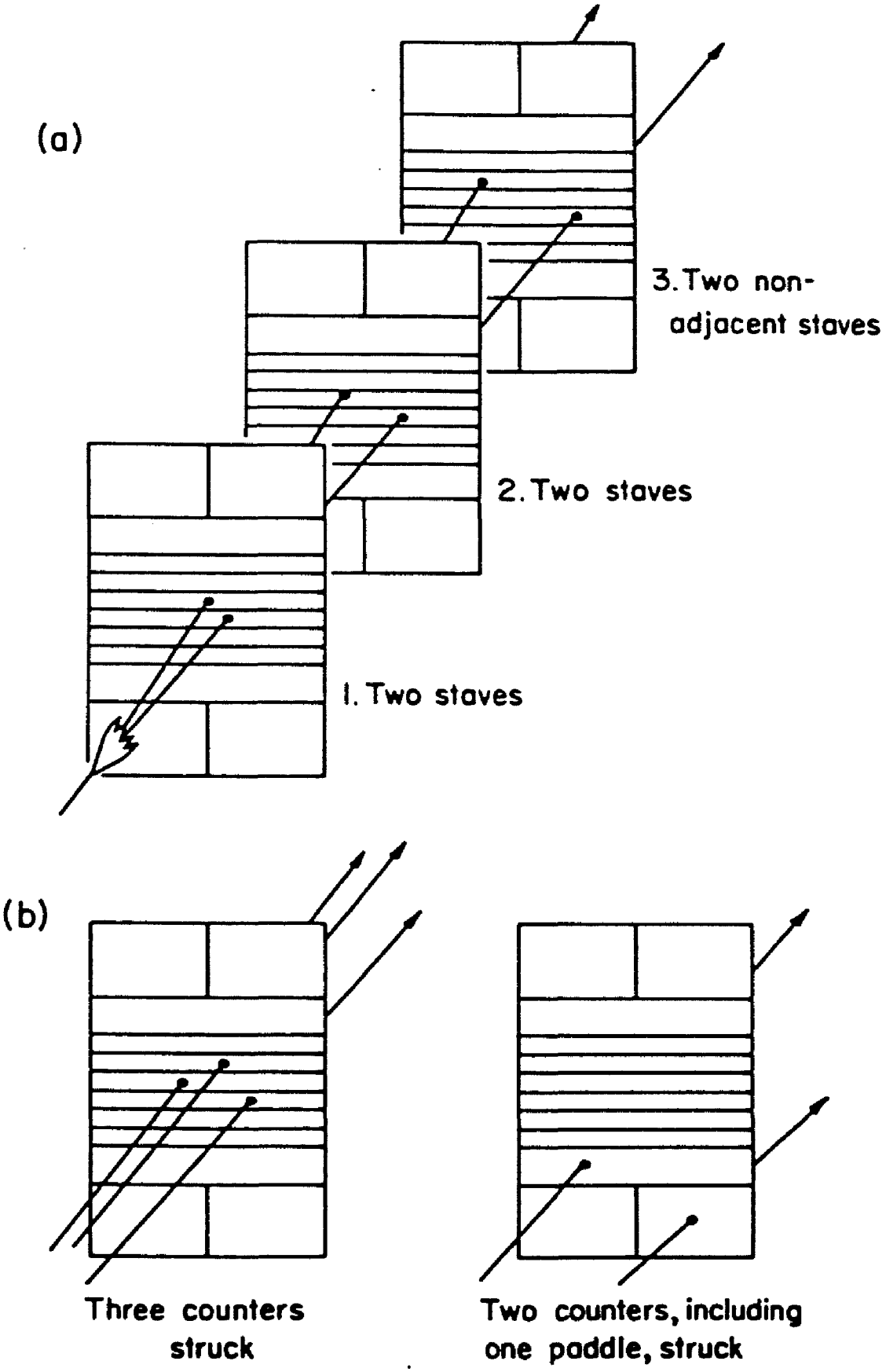
(a)
3. Two non-adjacent staves
2. Two staves
1. Two staves
(b)
Three counters struck
Two counters, including one paddle, struck

Figure 9.

Figure 10.-- Calorimeter subtrigger probability vs. shower energy.

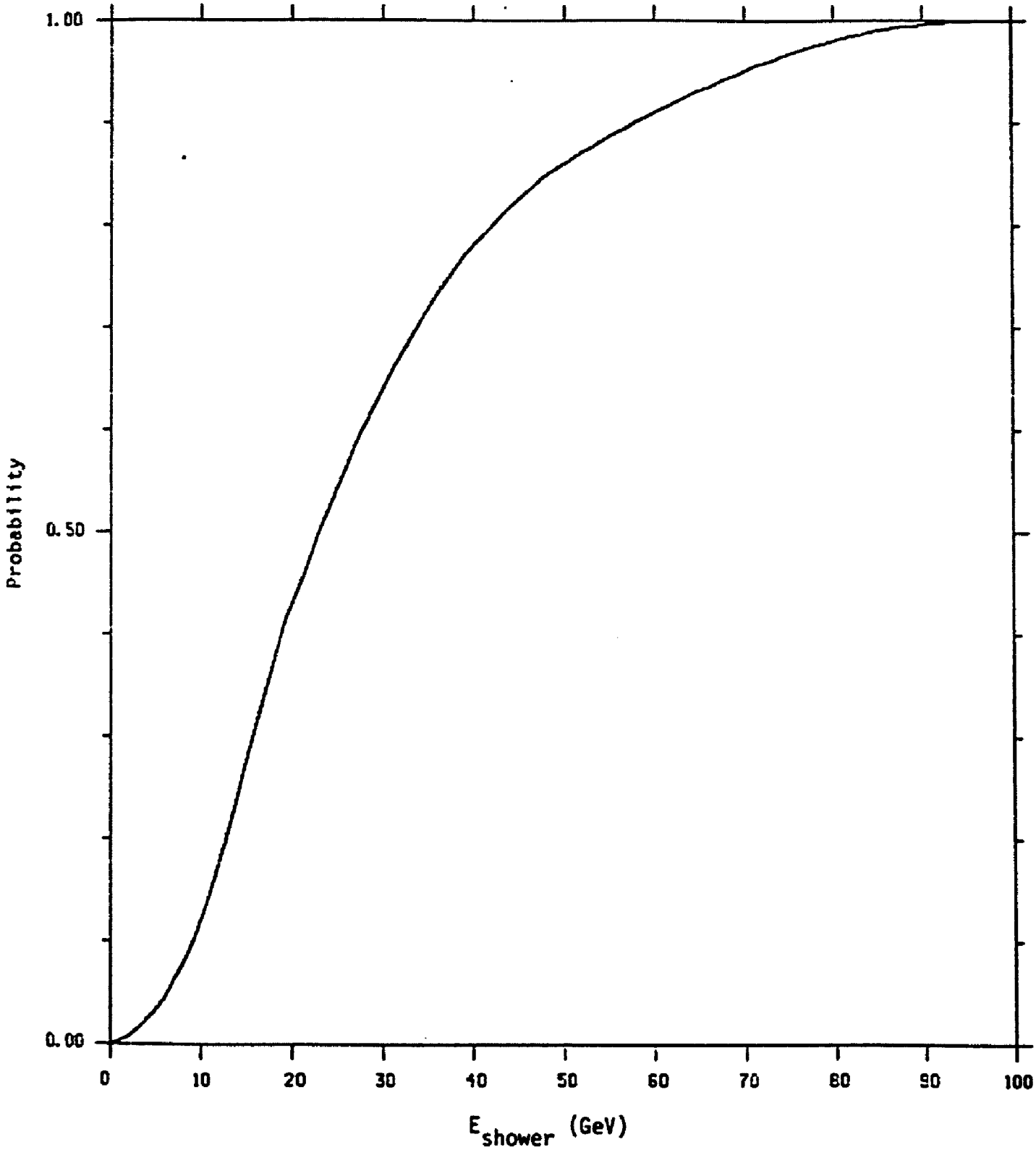
1.00
0.50
0.00
Probability
0
10
20
30
40
50
60
70
80
90
100
E shower (GeV)

Figure 10.

Figure 11.-- Multiwire proportional chamber center-finding electronics.

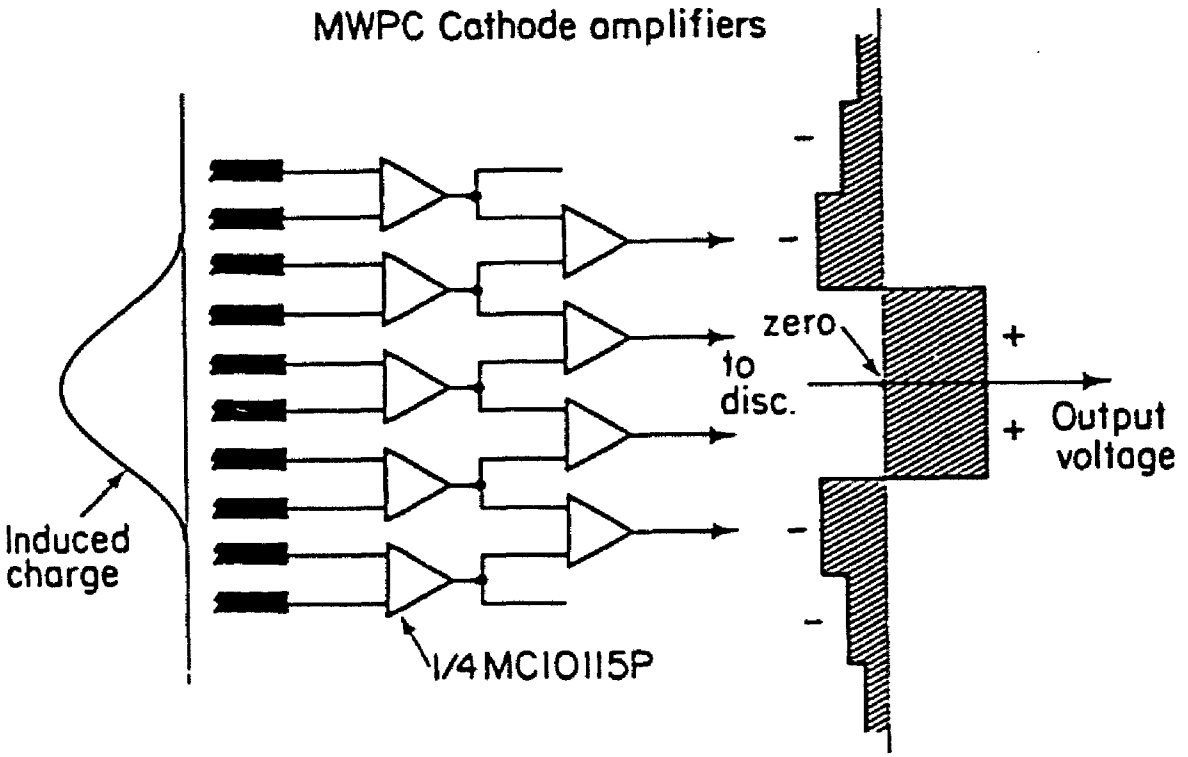

XBL 795-1599

Figure 11.

Figure 12.-- A drift chamber cell and preamplifier. The cathode wire spacing is 1/12 inch and the separation between cathode planes is 1/4 inch. The full width of the drift cell is 3/4 inch. In the circuit, each stage is one-third of a 10116 ECL triple line receiver. Not shown in the circuit diagram are "pull-down" resistors connecting both outputs from each stage to -5V.

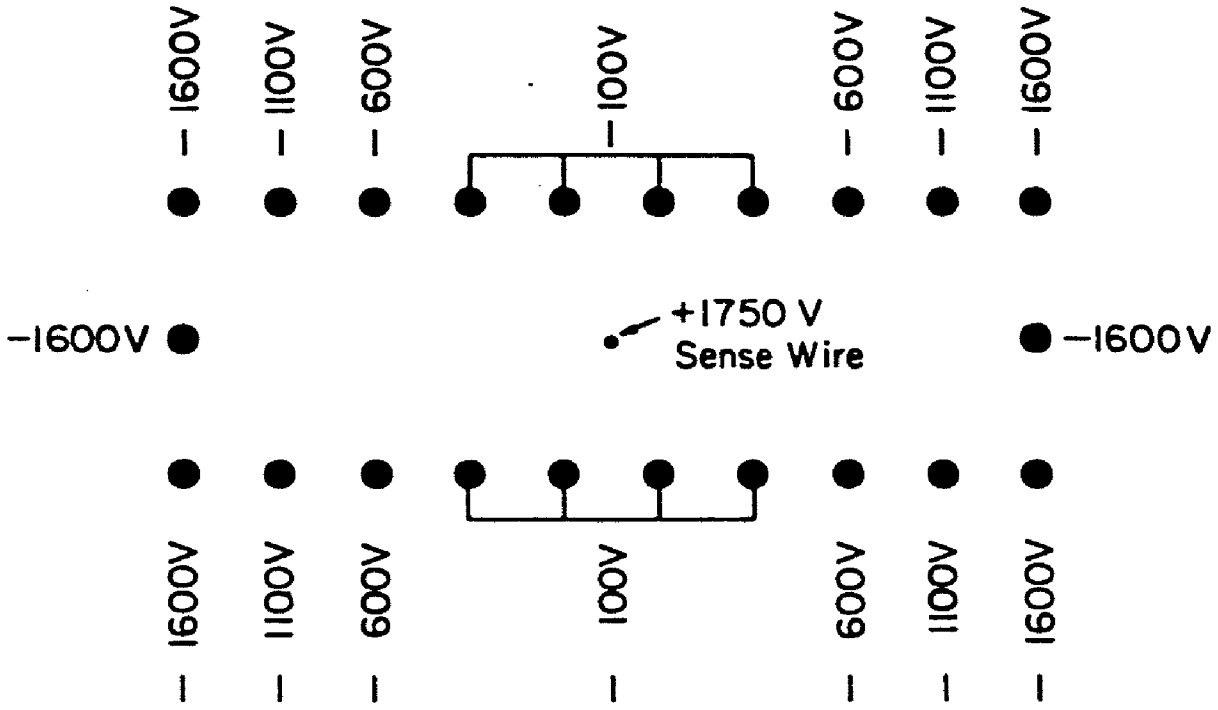
-1600V
-1100V
-600V
-100V
-600V
-1100V
-1600V
-1600V
+1750 V
Sense Wire
-1600V
1600V
1100V
600V
100V
600V
1100V
1600V

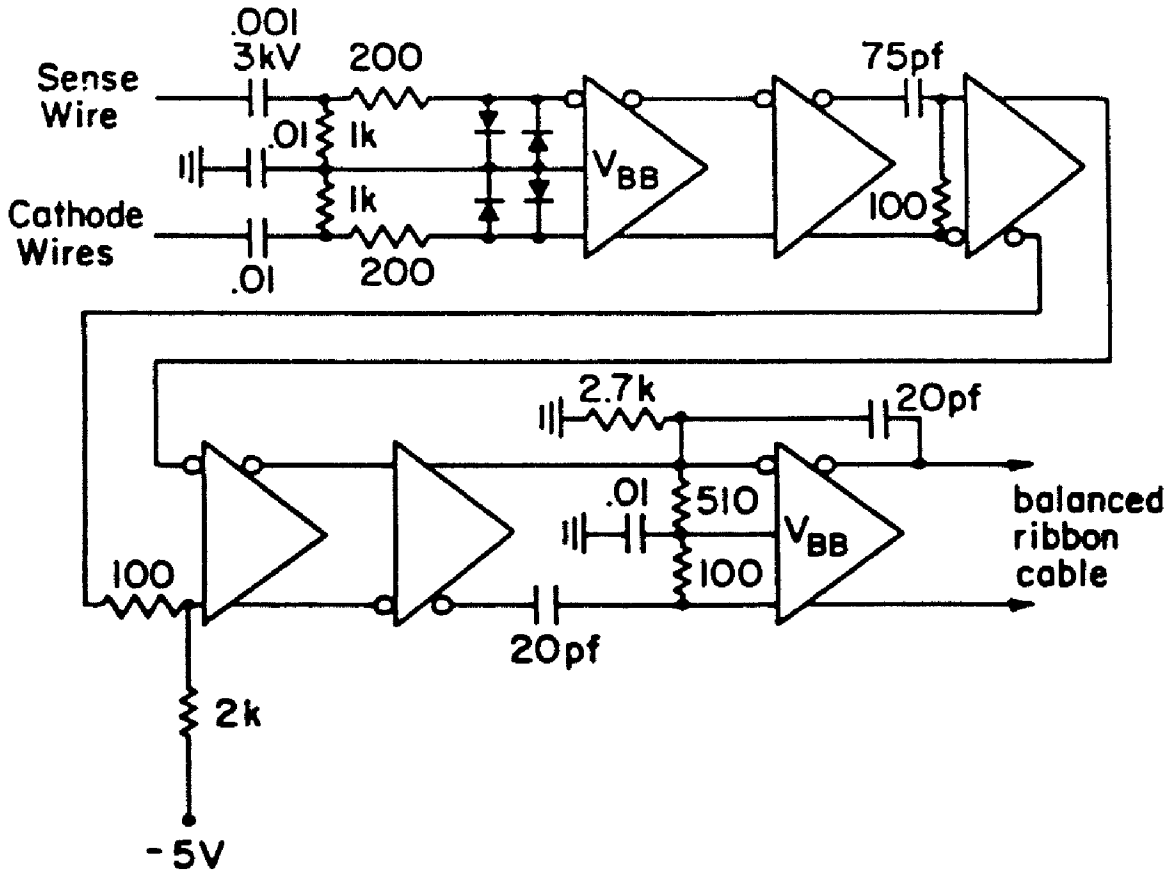
.001
3kV
200
Sense
Wire
.01
1k
1k
Cathode
Wires
.01
200
V_{BB}
75pf
100
2.7k
20pf
.01
510
100
V_{BB}
balanced
ribbon
cable
100
20pf
2k
-5V

Figure 12.

Figure 13.--"Logical" flow in the track-fitting program.

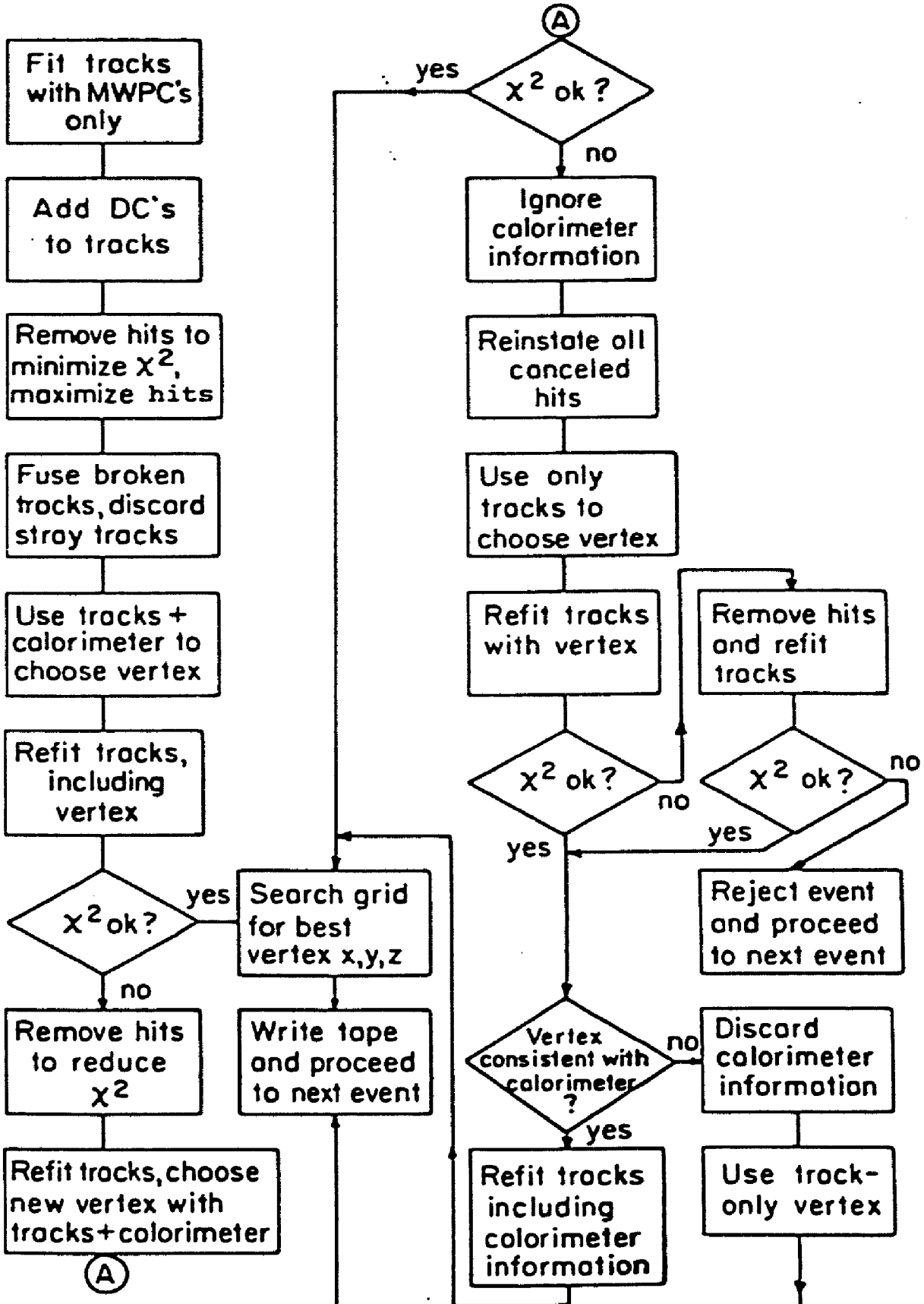
Fit tracks with MWPC's only
Add DC's to tracks
Remove hits to minimize χ^2, maximize hits
Fuse broken tracks, discord stray tracks
Use tracks + colorimeter to choose vertex
Refit tracks, including vertex
χ^2 ok?
yes
no
Search grid for best vertex x,y,z
Write tape and proceed to next event
Remove hits to reduce χ^2
Refit tracks, choose new vertex with tracks+colorimeter
A
A
χ^2 ok ?
yes
no
Ignore colorimeter information
Reinstate all canceled hits
Use only tracks to choose vertex
Refit tracks with vertex
χ^2 ok?
no
yes
Remove hits and refit tracks
χ^2 ok?
no
yes
Reject event and proceed to next event
Vertex consistent with colorimeter ?
no
yes
Discard colorimeter information
Use track-only vertex
Refit tracks including colorimeter information

Figure 13.

Figure 14.-- $c\bar{c}$ pair mass in the photon-gluon-fusion model.

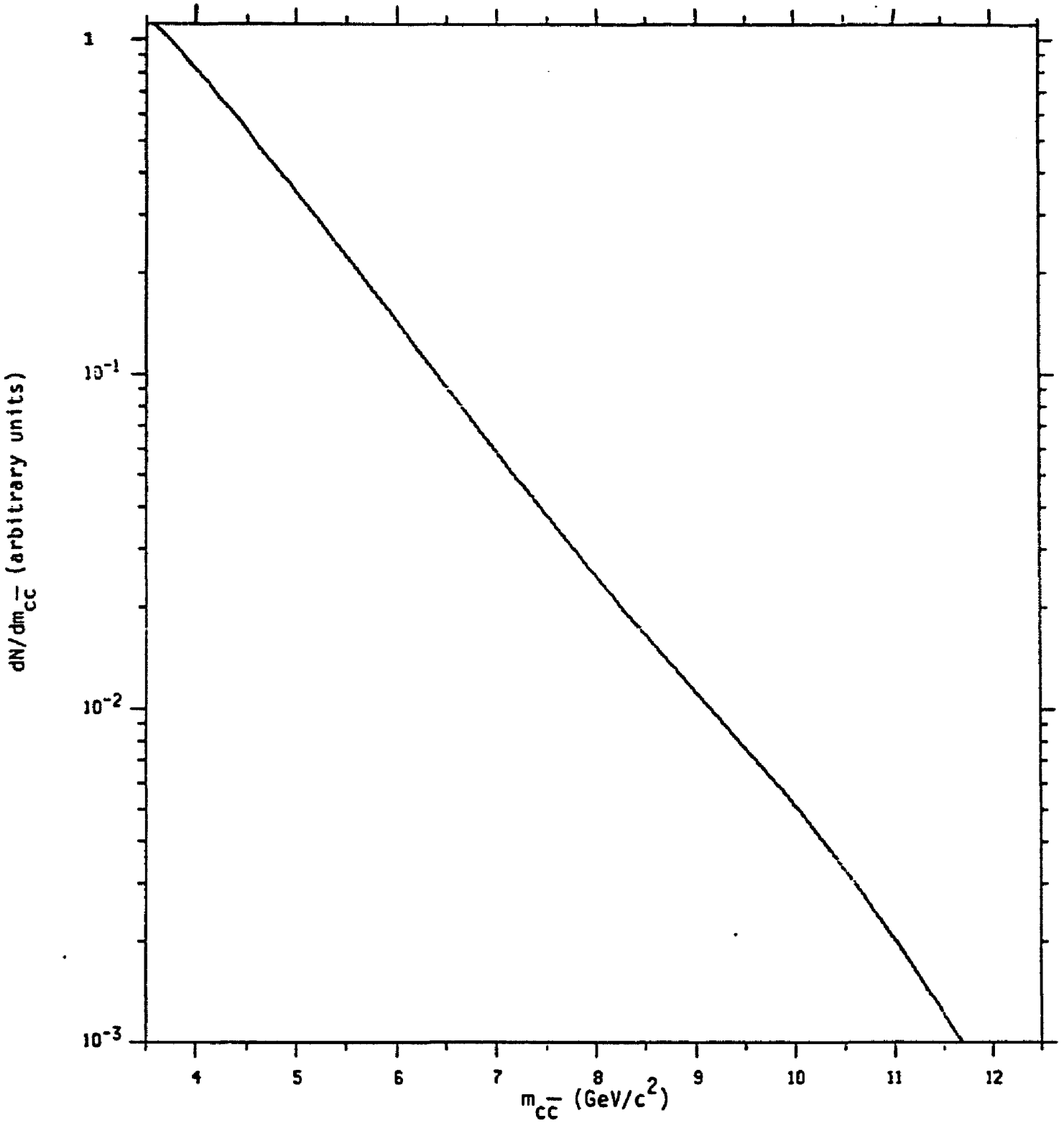
1
10^{-1}
10^{-2}
10^{-3}
$dN/dm_{c\bar{c}}$ (arbitrary units)
4
5
6
7
8
9
10
11
12
$m_{c\bar{c}}$ (GeV/c^2)

Figure 14.

Figure 15.-- Momentum transfer-squared in the photon-gluon-fusion model. (a) All events generated; (b) Events satisfying the dimuon trigger.

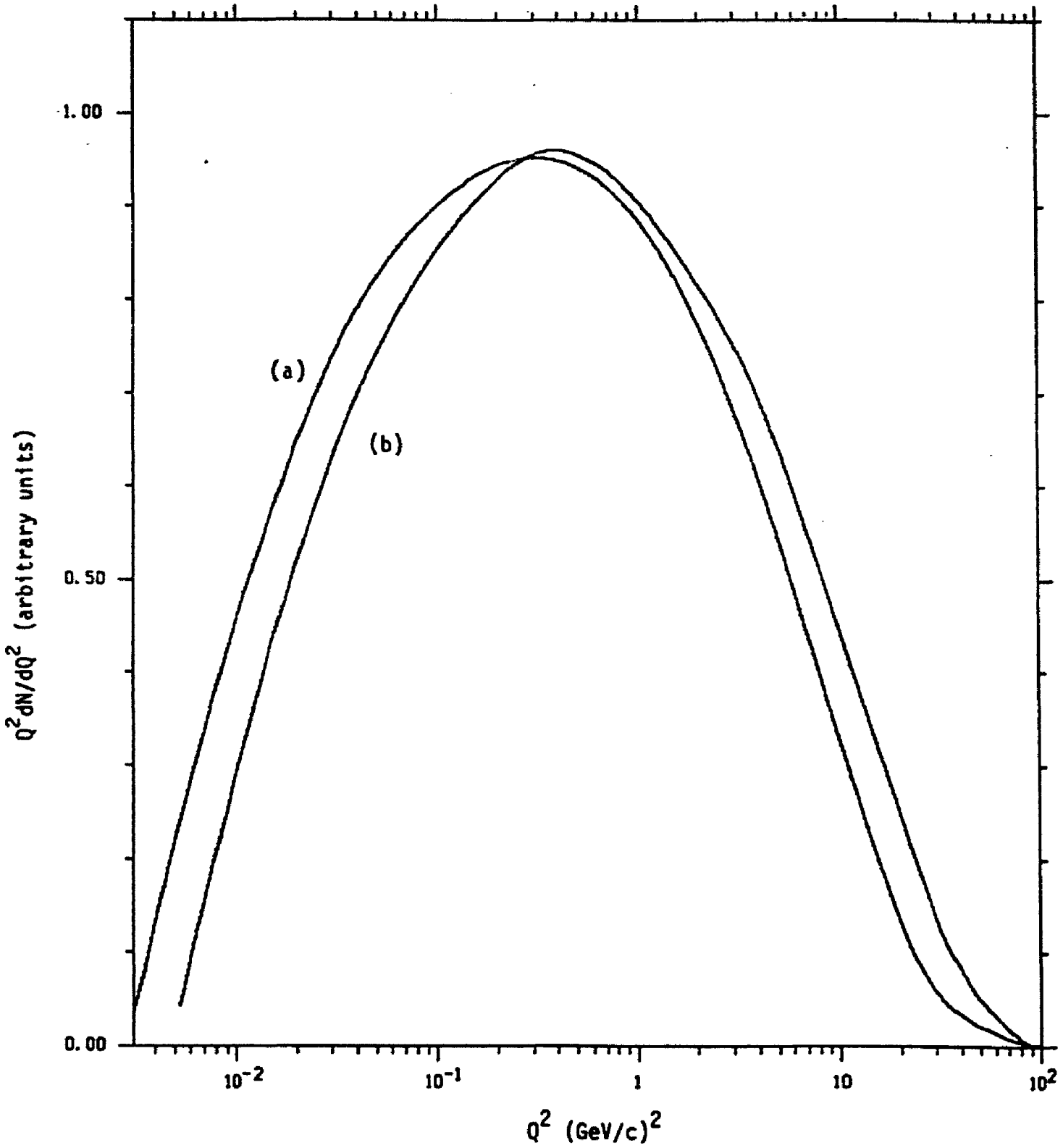
1.00
0.50
0.00
(a)
(b)
$Q^2 dN/dQ^2$ (arbitrary units)
10^{-2}
10^{-1}
1
10
10^2
Q^2 (GeV/c)^2

Figure 15.

Figure 16.-- Hadronic shower energy in the photon-gluon-fusion model. (a) All events generated; (b) Events satisfying the dimuon trigger.

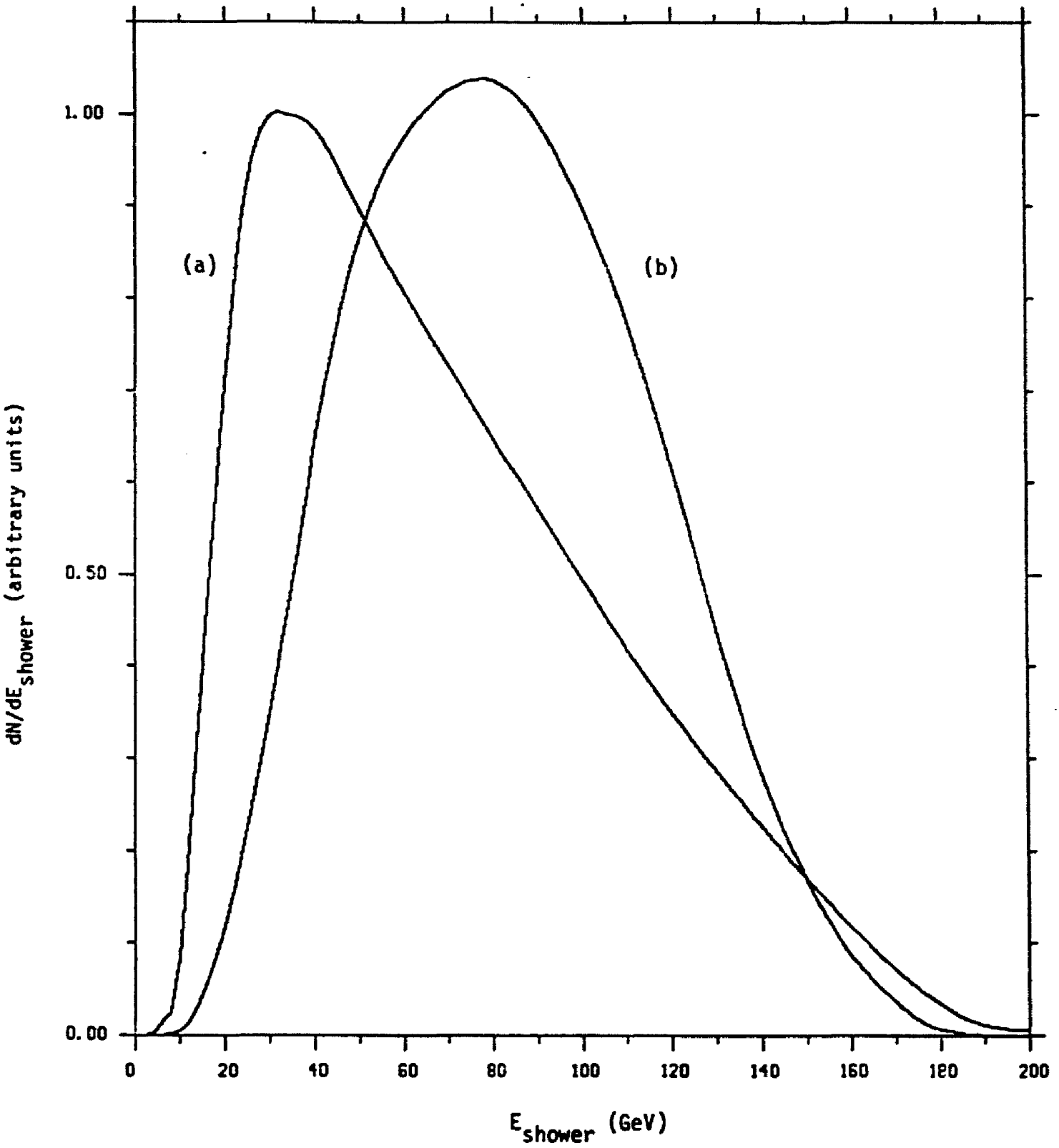
1.00
0.50
0.00
(a)
(b)
0
20
40
60
80
100
120
140
160
180
200
dN/dE shower (arbitrary units)
E shower (GeV)

Figure 16.

Figure 17.-- Daughter muon energy in the photon-gluon-fusion model: (a) all events generated; (b) events satisfying the dimuon trigger.

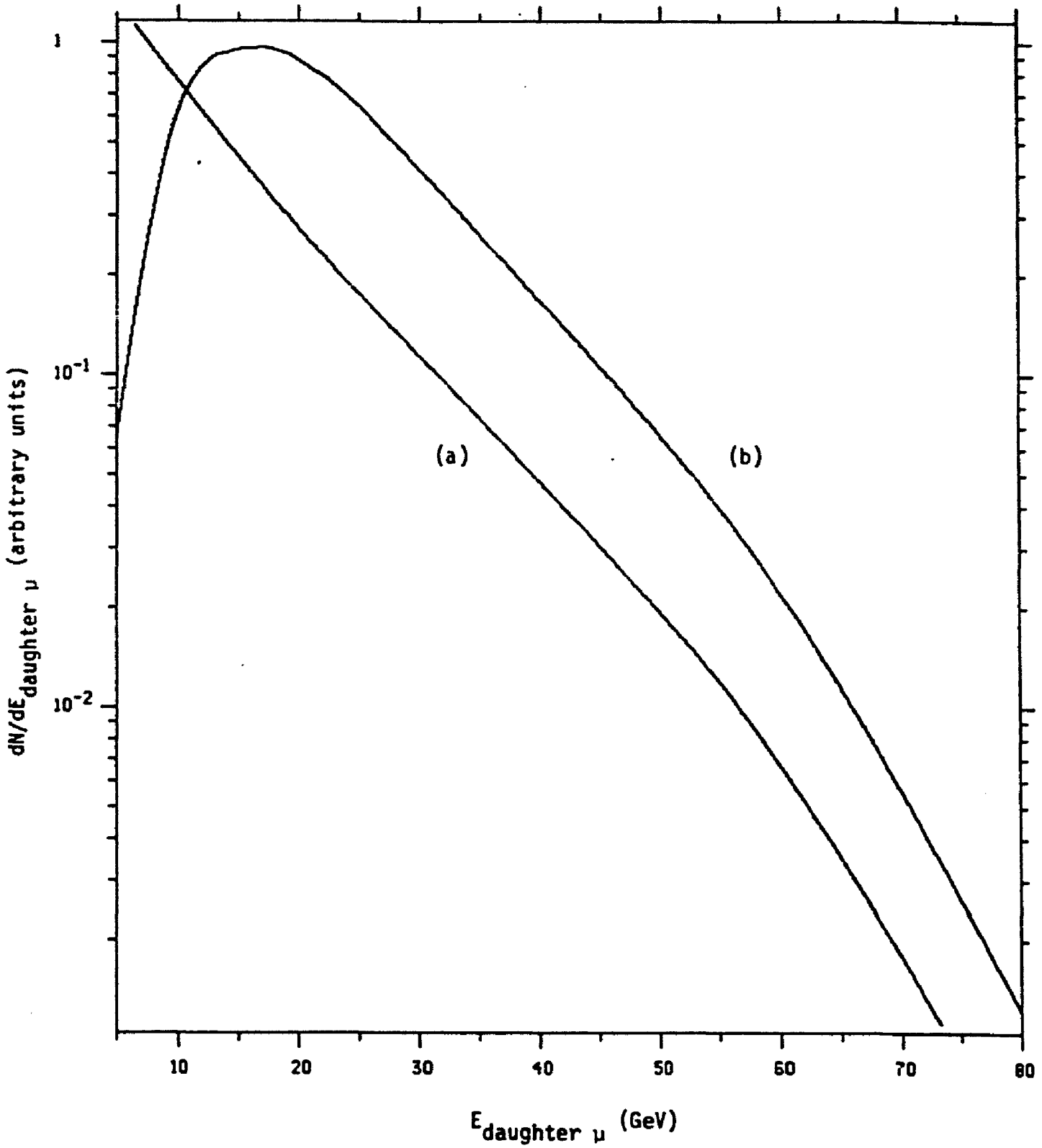
1
10^{-1}
10^{-2}
$dN/dE_{daughter\ \mu}$ (arbitrary units)
(a)
(b)
10
20
30
40
50
60
70
80
$E_{daughter\ \mu}$ (GeV)

Figure 17.

Figure 18.-- Energy lost by the beam muon in the photon-gluon-fusion model. (a) All events generated; (b) Events satisfying the dimuon trigger.

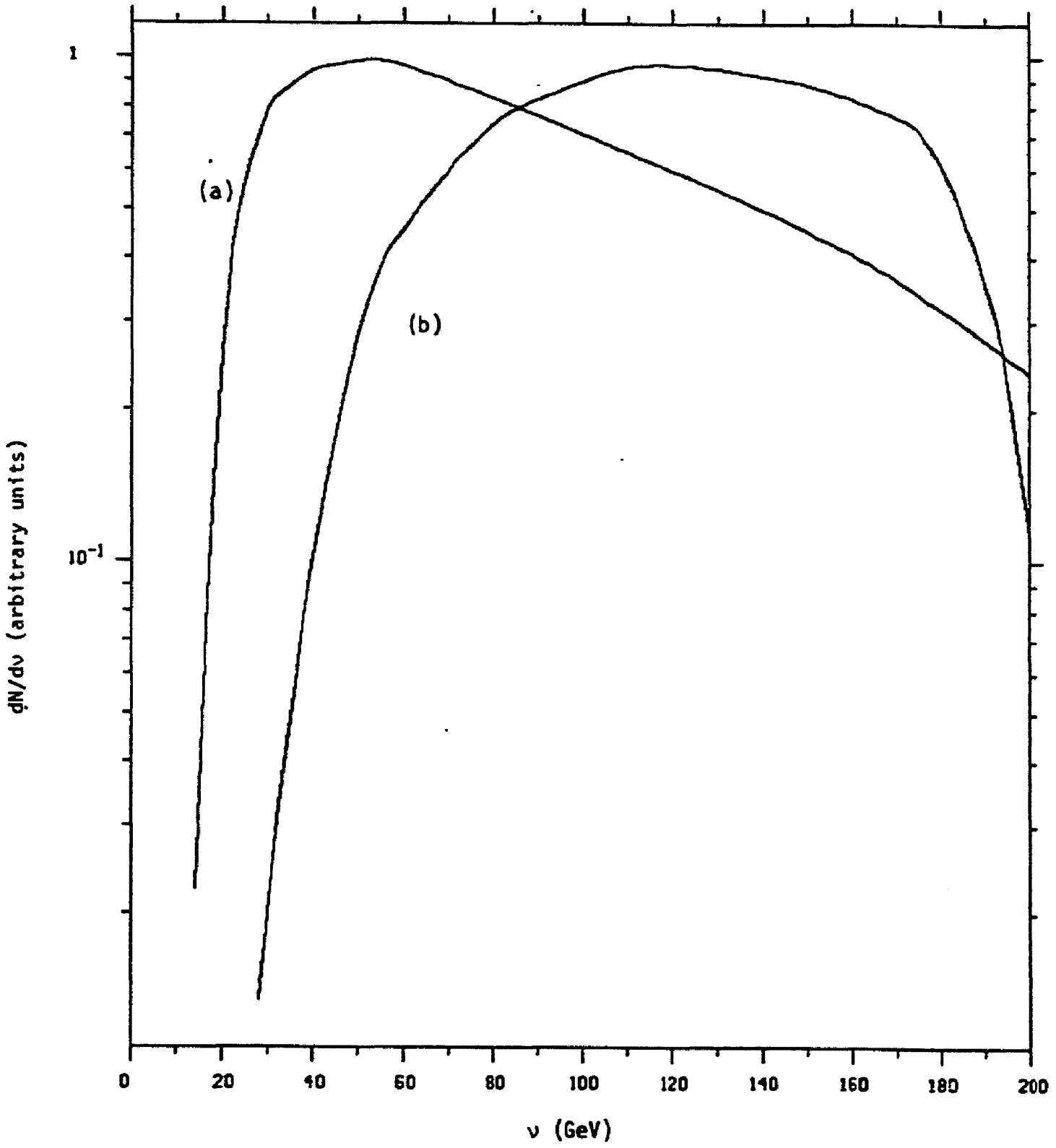
1
10^{-1}
(a)
(b)
dN/dν (arbitrary units)
0
20
40
60
80
100
120
140
160
180
200
ν (GeV)

Figure 18.

Figure 19.-- Distribution of interaction vertices in slabs in a module for shower Monte Carlo events.

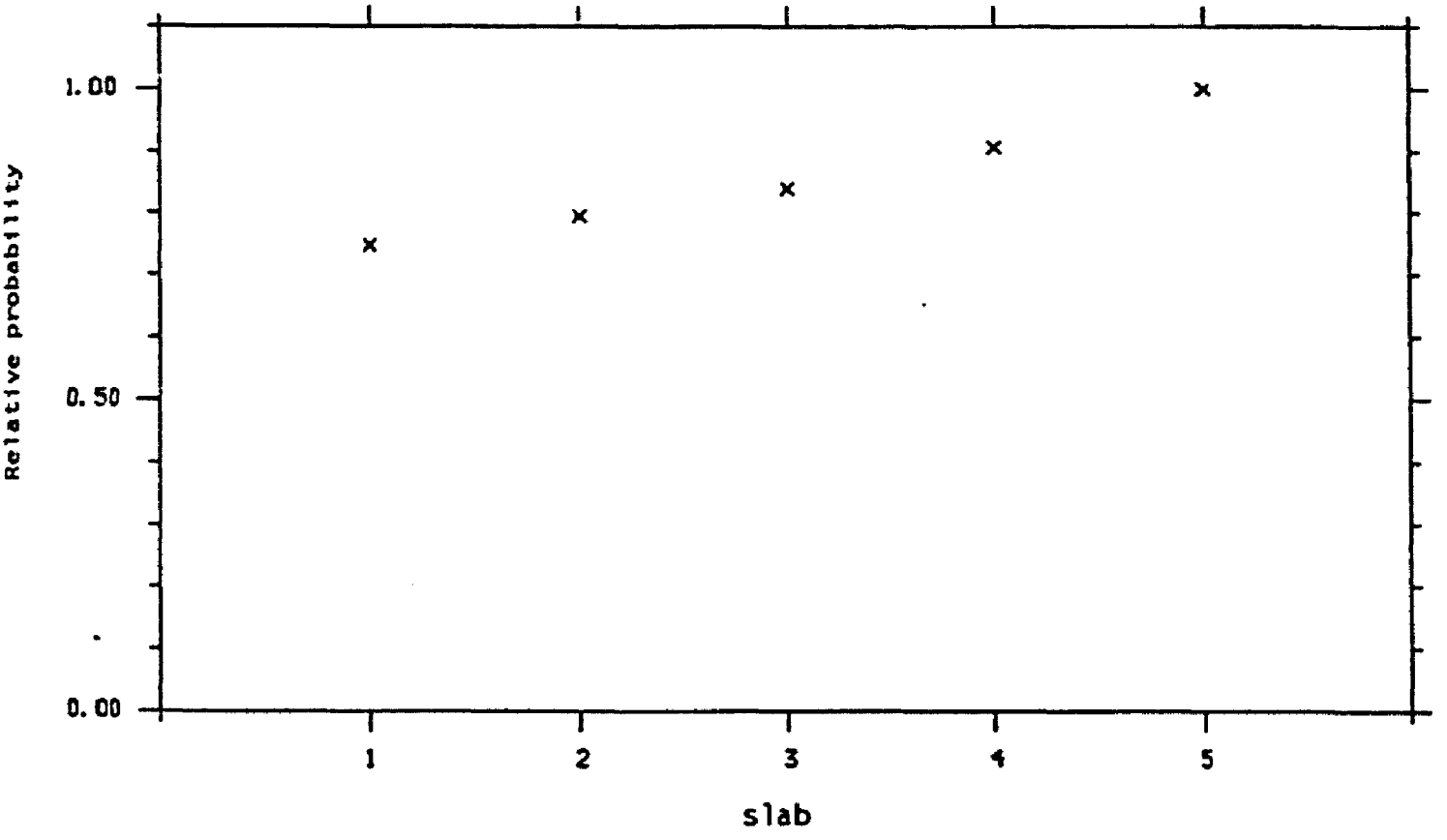

Figure 19.

Figure 20.-- Distance from vertex to meson decay point for shower Monte Carlo events.

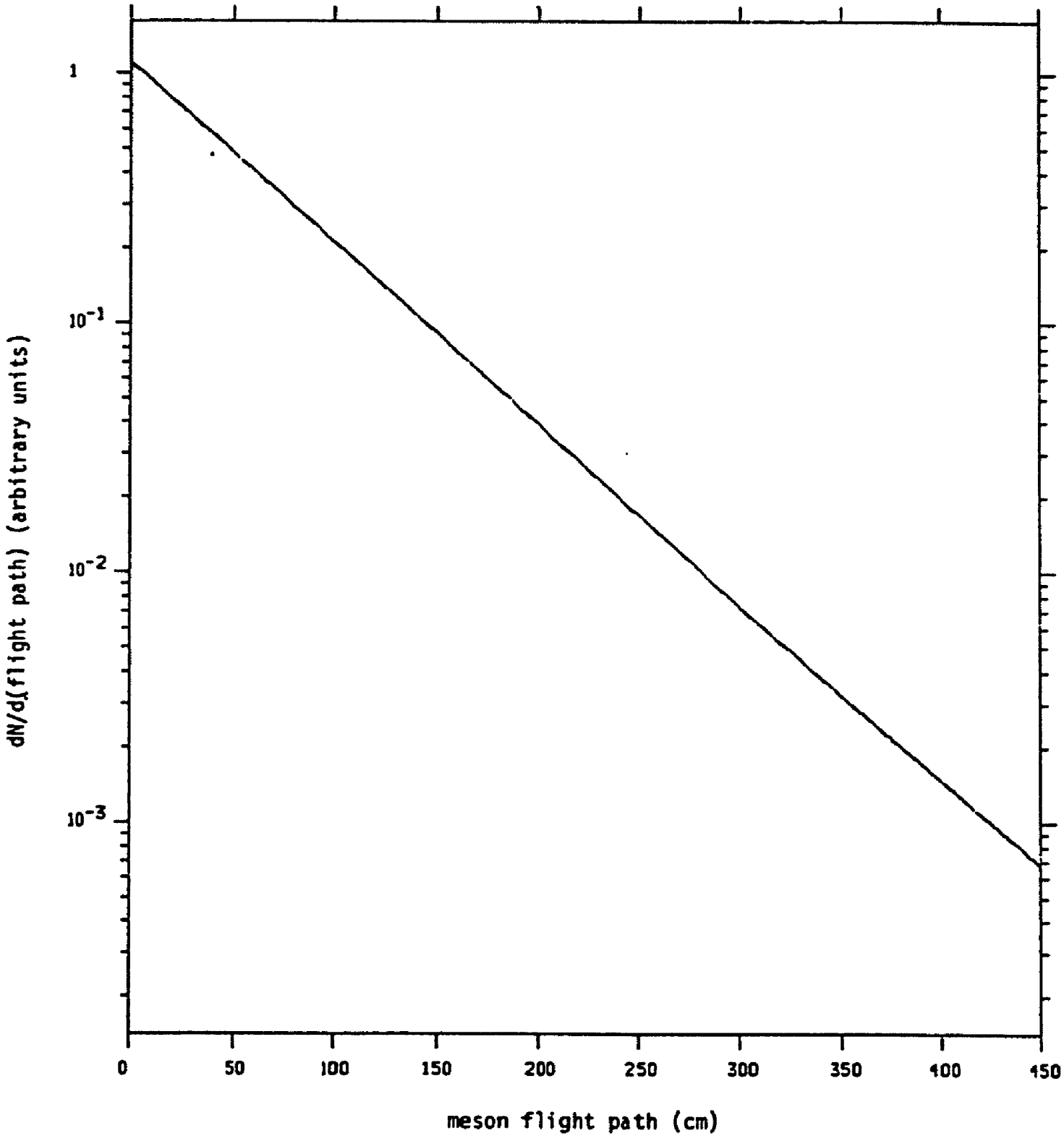
1
10^{-1}
10^{-2}
10^{-3}
dN/d(flight path) (arbitrary units)
0
50
100
150
200
250
300
350
400
450
meson flight path (cm)

Figure 20.

Figure 21.-- Probability vs. shower energy for a shower to yield a decay muon with more than 9 GeV of energy.

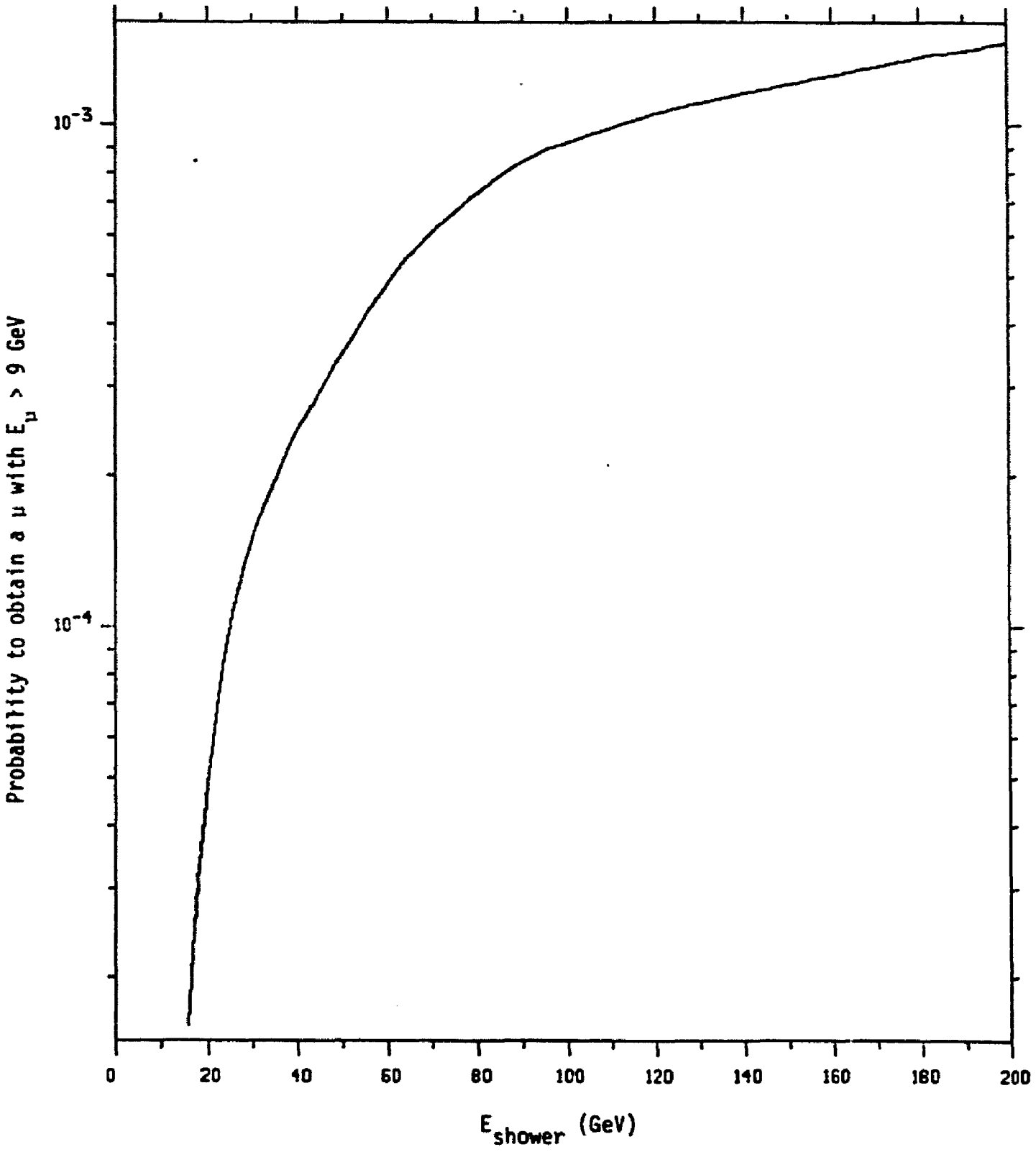
Probability to obtain a μ with E_μ > 9 GeV
10^{-3}
10^{-4}
0
20
40
60
80
100
120
140
160
180
200
E_{shower} (GeV)

Figure 21.

Figure 22.-- Charged multiplicity in simulated showers for π, K mesons with more than 5 GeV of energy.

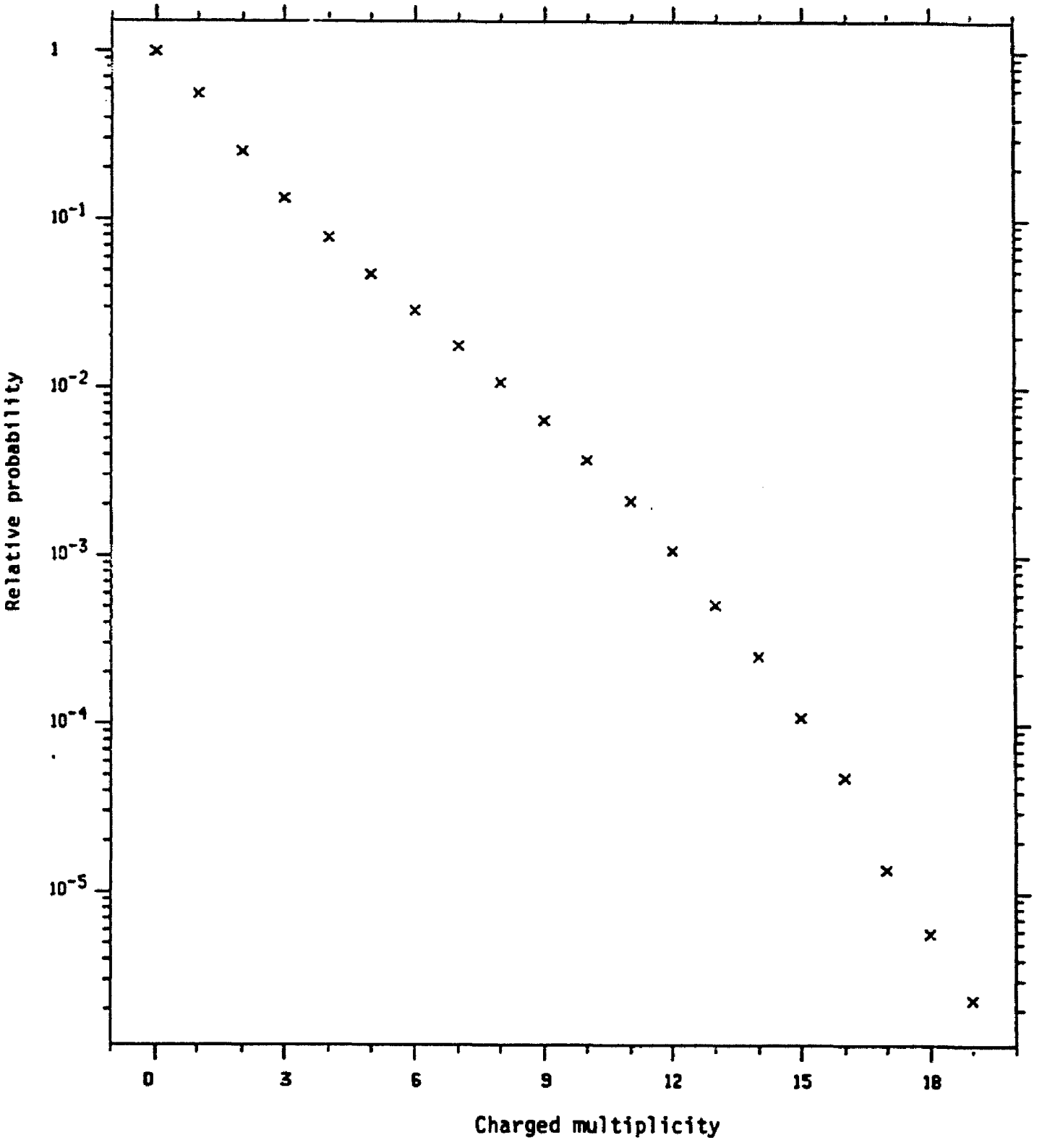
1
10^{-1}
10^{-2}
10^{-3}
10^{-4}
10^{-5}
Relative probability
0
3
6
9
12
15
18
Charged multiplicity

Figure 22.

Figure 23.-- Number of meson generations between virtual photon-nucleon interaction and decay muon in simulated showers.

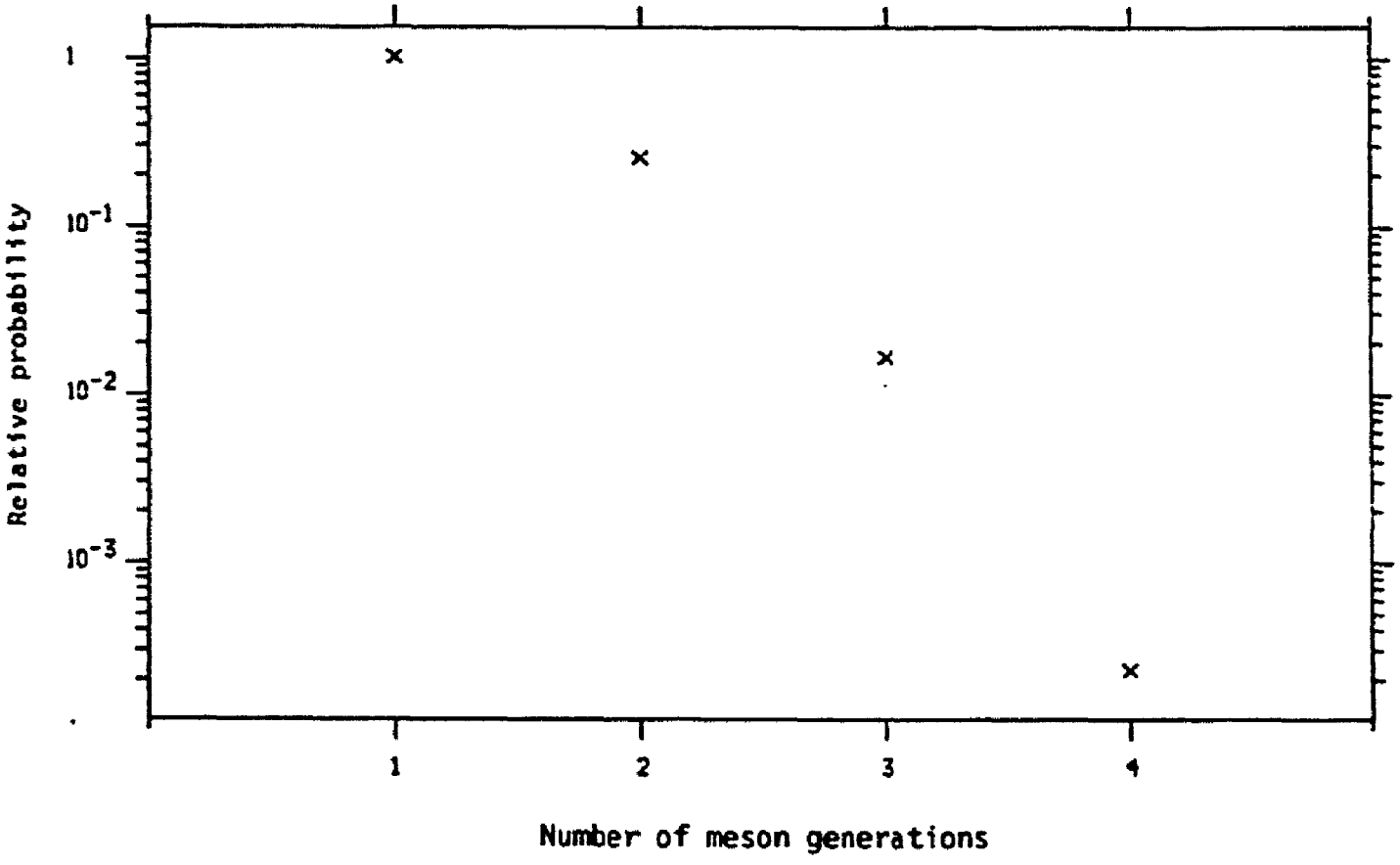
Relative probability
1
10^{-1}
10^{-2}
10^{-3}
1
2
3
4
Number of meson generations

Figure 23.

Figure 24.-- Decay probability for π's and K's in simulated showers.

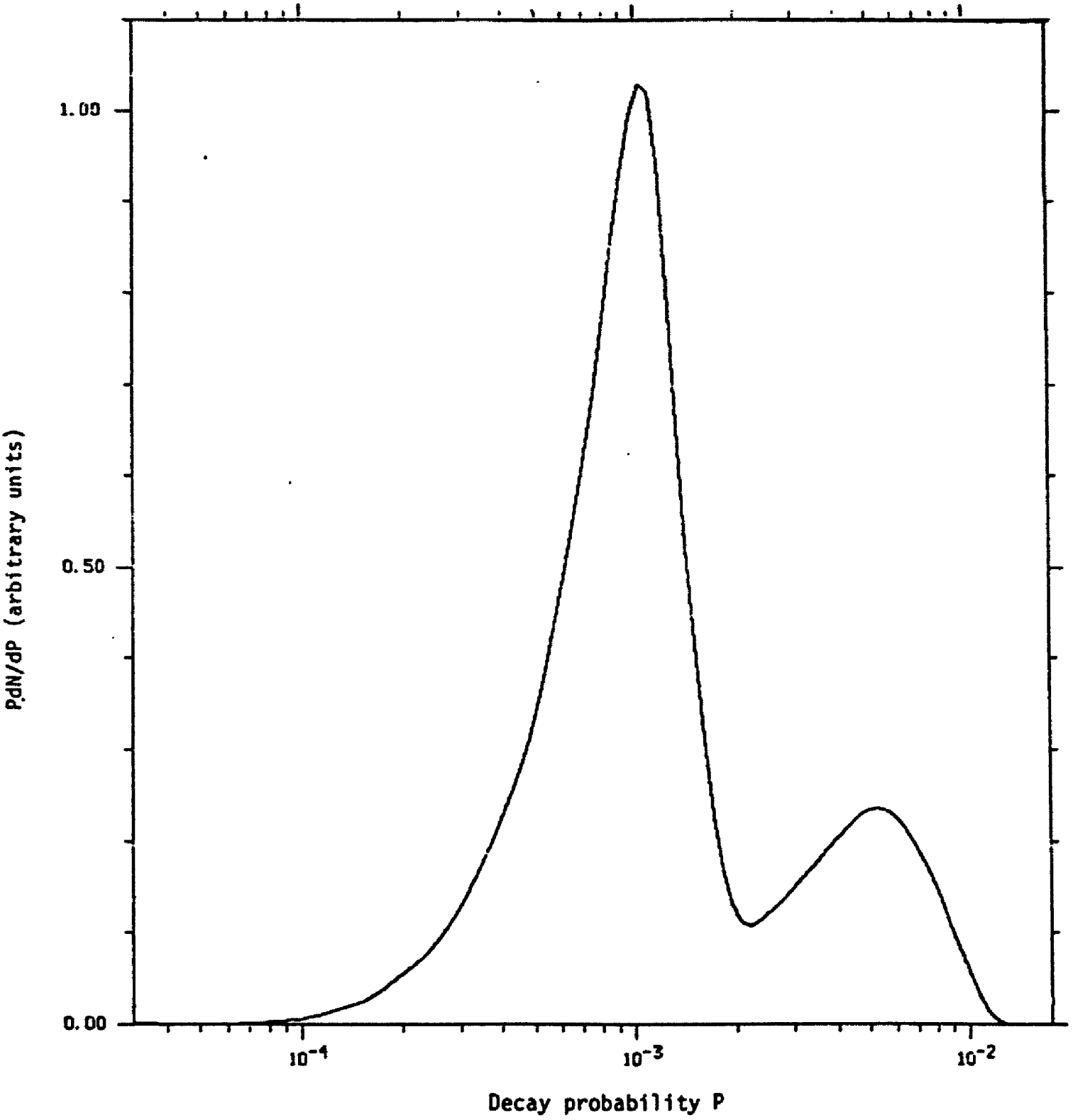
1.00
0.50
0.00
P.dN/dP (arbitrary units)
10^{-4}
10^{-3}
10^{-2}
Decay probability P

Figure 24.

Figure 25.-- Energy lost by the beam muon in simulated inelastic collisions.

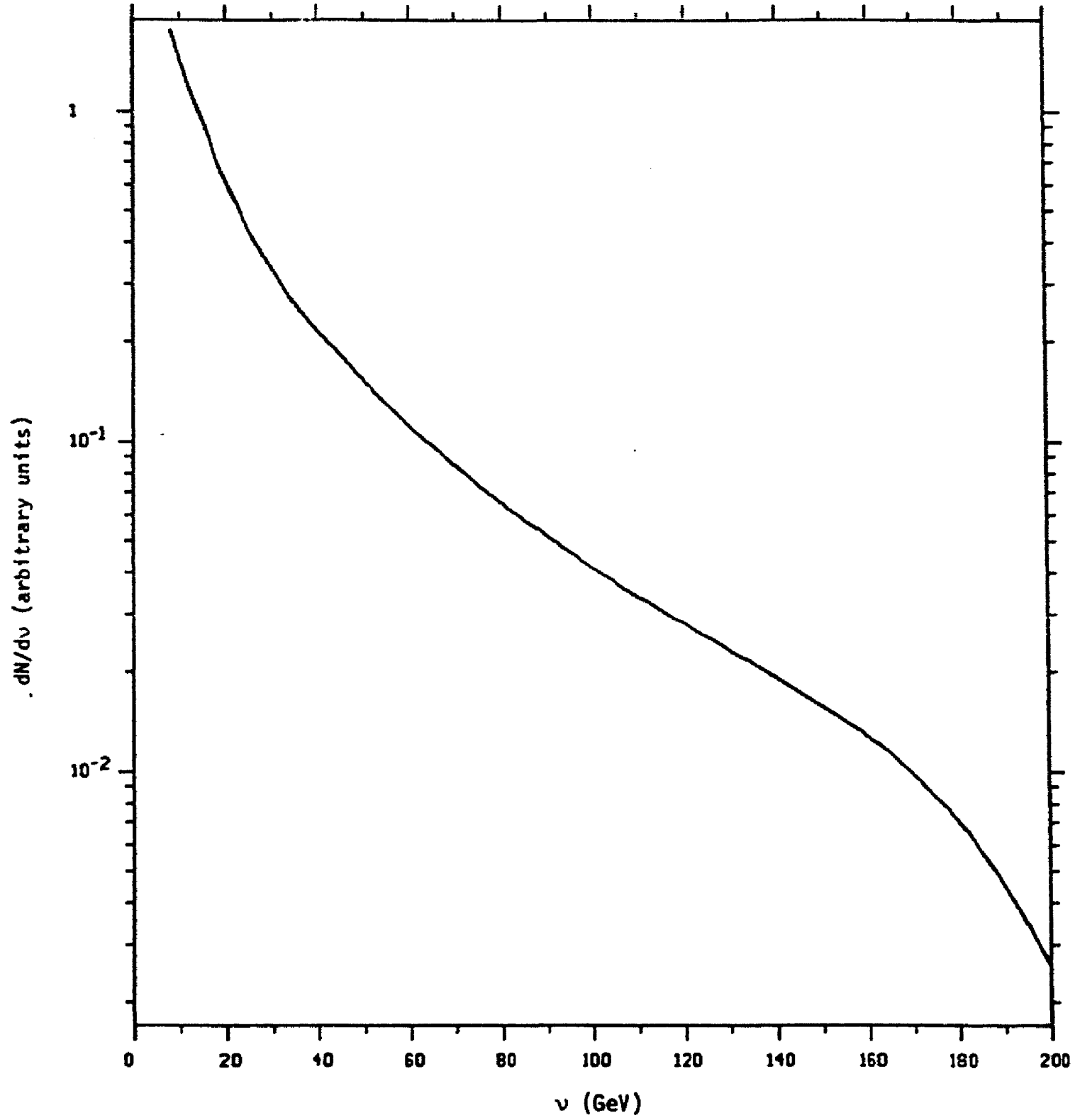
1
10^{-1}
10^{-2}
dN/dν (arbitrary units)
0
20
40
60
80
100
120
140
160
180
200
ν (GeV)

Figure 25.

Figure 26.-- Momentum transfer-squared in simulated muon-nucleon inelastic collisions.

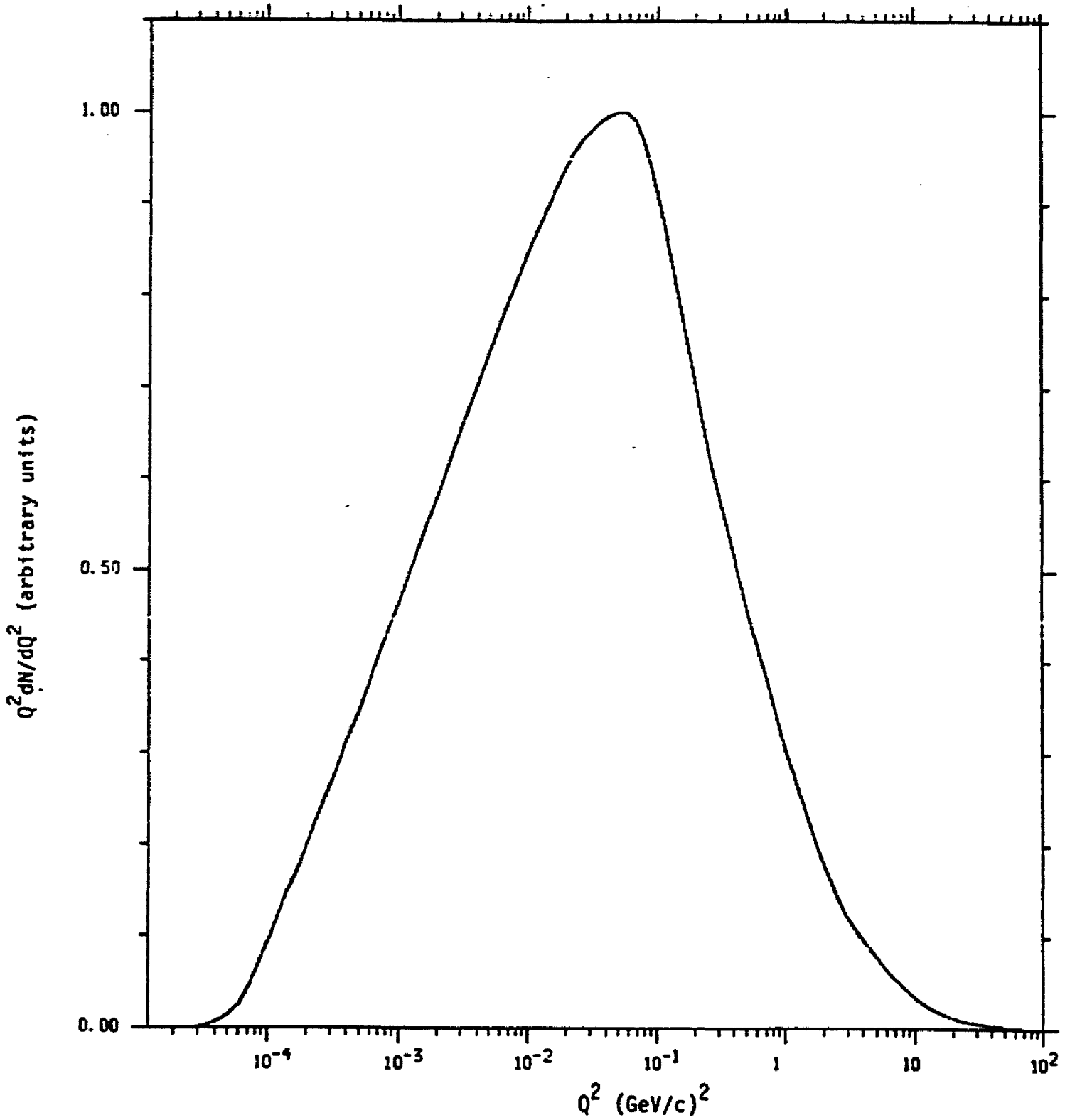
1.00
0.50
0.00
$Q^2 dN/dQ^2$ (arbitrary units)
10^{-4}
10^{-3}
10^{-2}
10^{-1}
1
10
10^2
Q^2 (GeV/c)^2

Figure 26.

Figure 27.-- Feynman x for primary shower mesons with more than 5 Gev of energy in simulated showers.

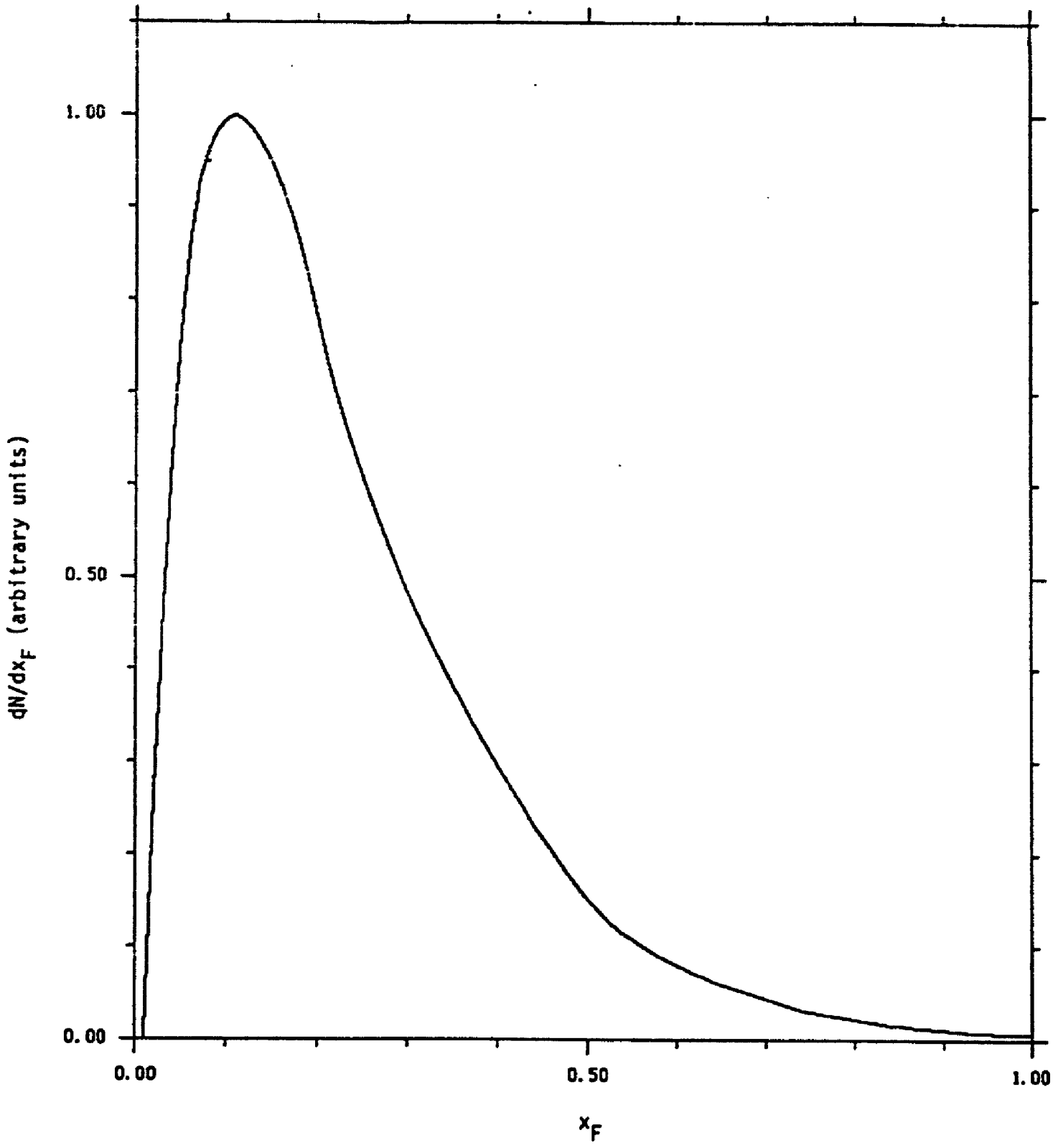

Figure 27.

Figure 28.-- p_T^2 distributions for primary shower mesons with more than 5 GeV of energy in simulated showers.

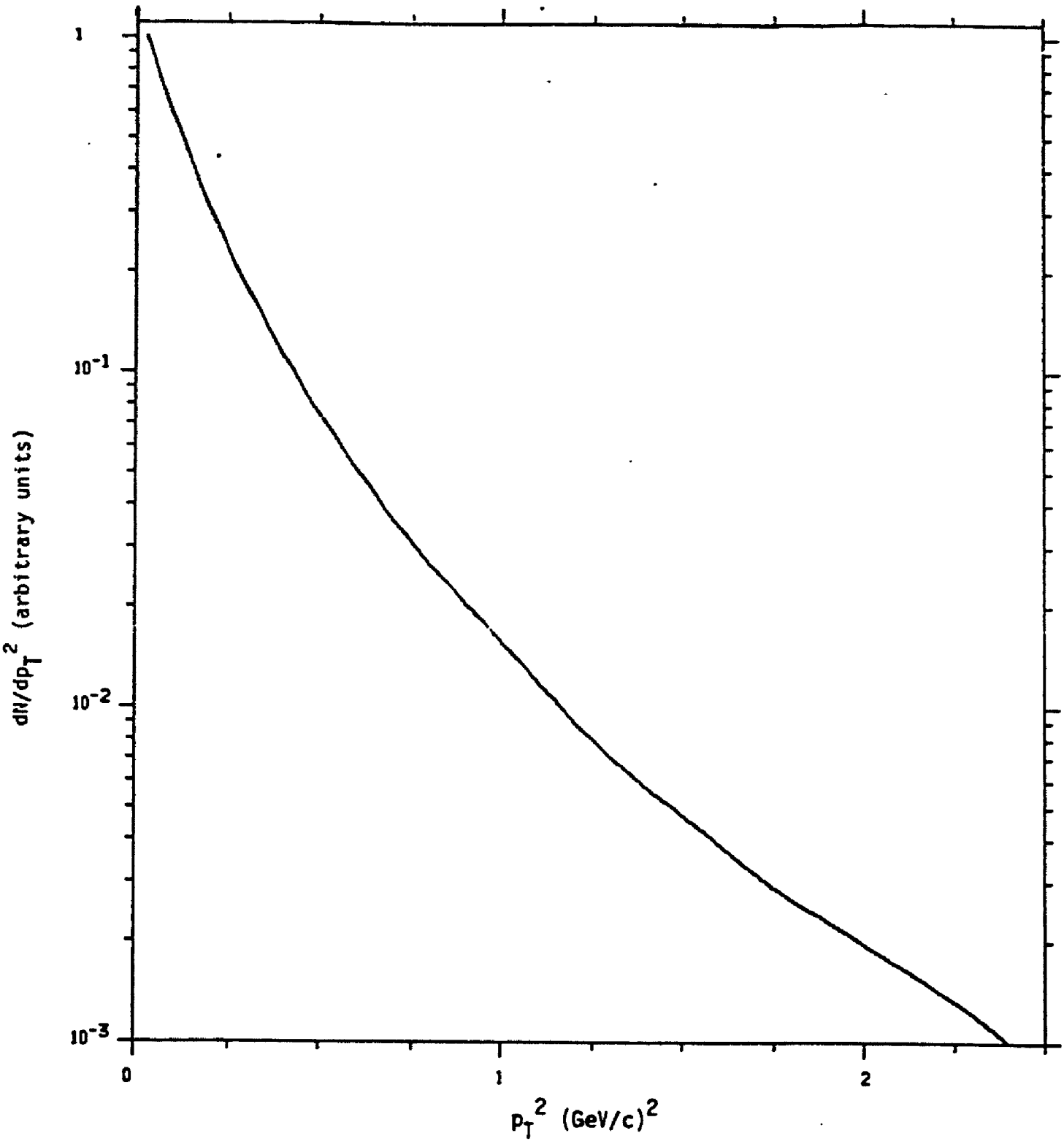

Figure 28.

Figure 29.-- Feynman x distributions for all secondary mesons before imposing energy conservation in simulated showers.

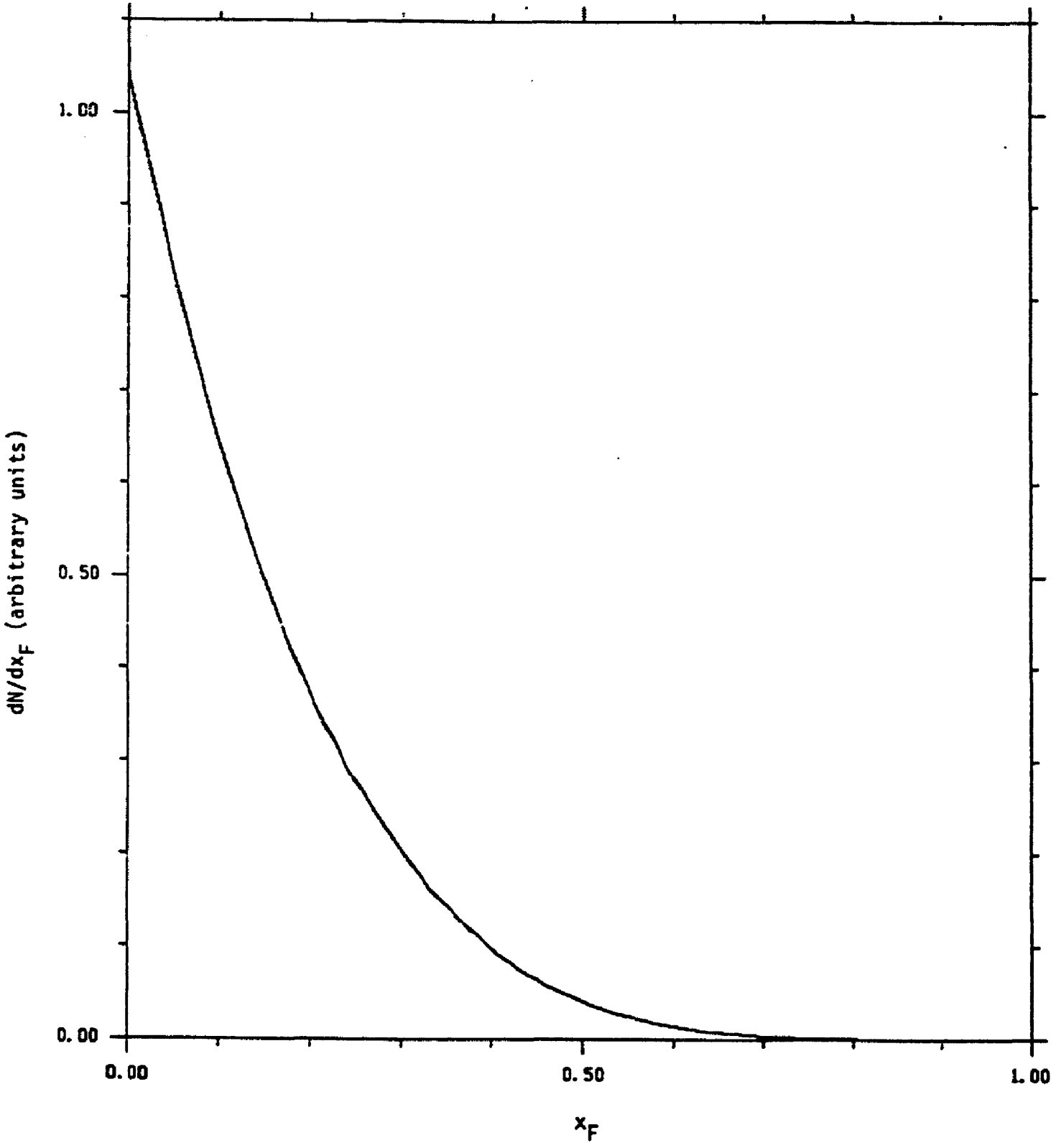

Figure 29.

Figure 30.-- p_T^2 distributions for all secondary mesons before imposing energy conservation in simulated showers.

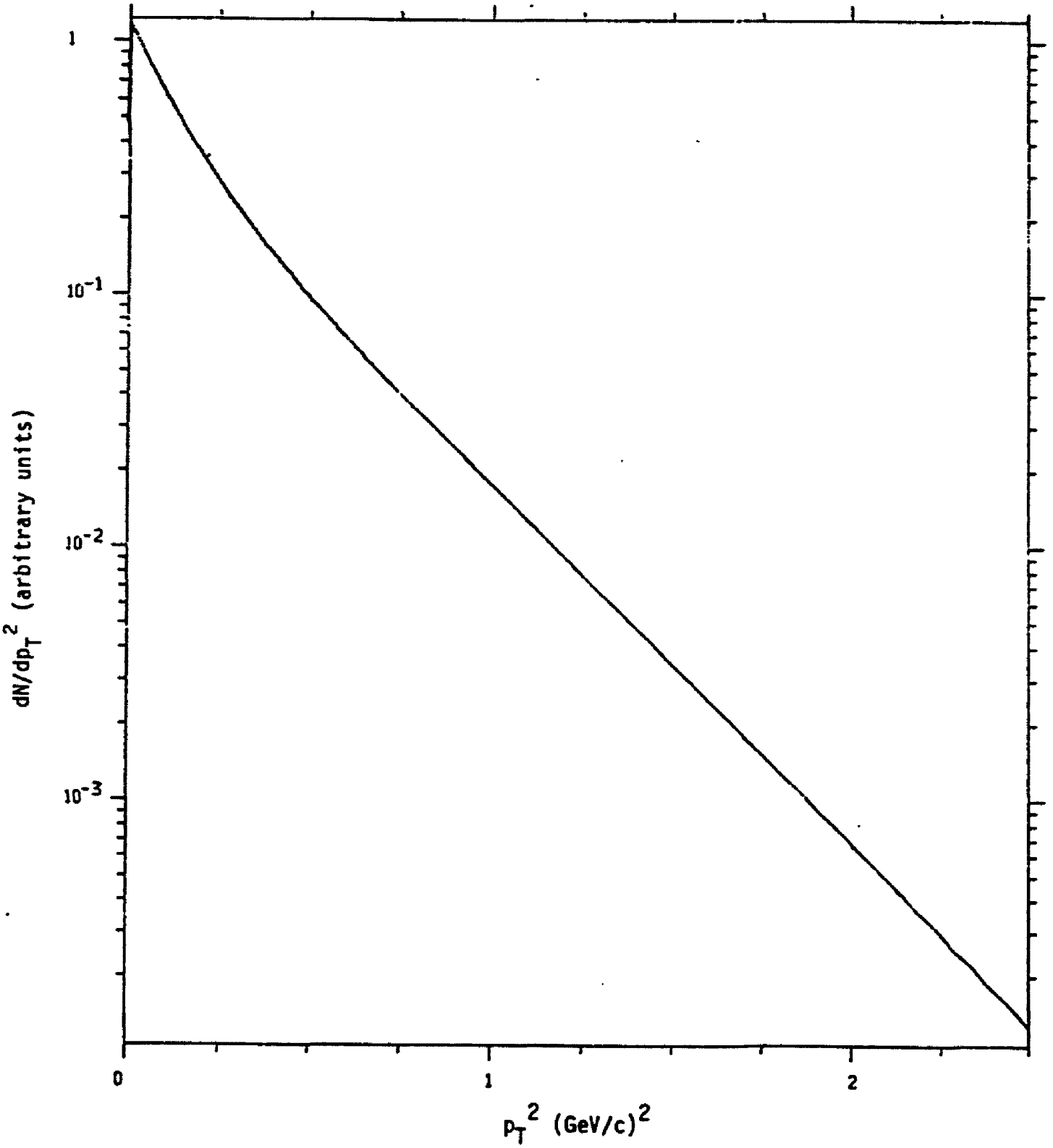

Figure 30.

Figure 31.-- Energy of hadrons which decay in simulated showers.

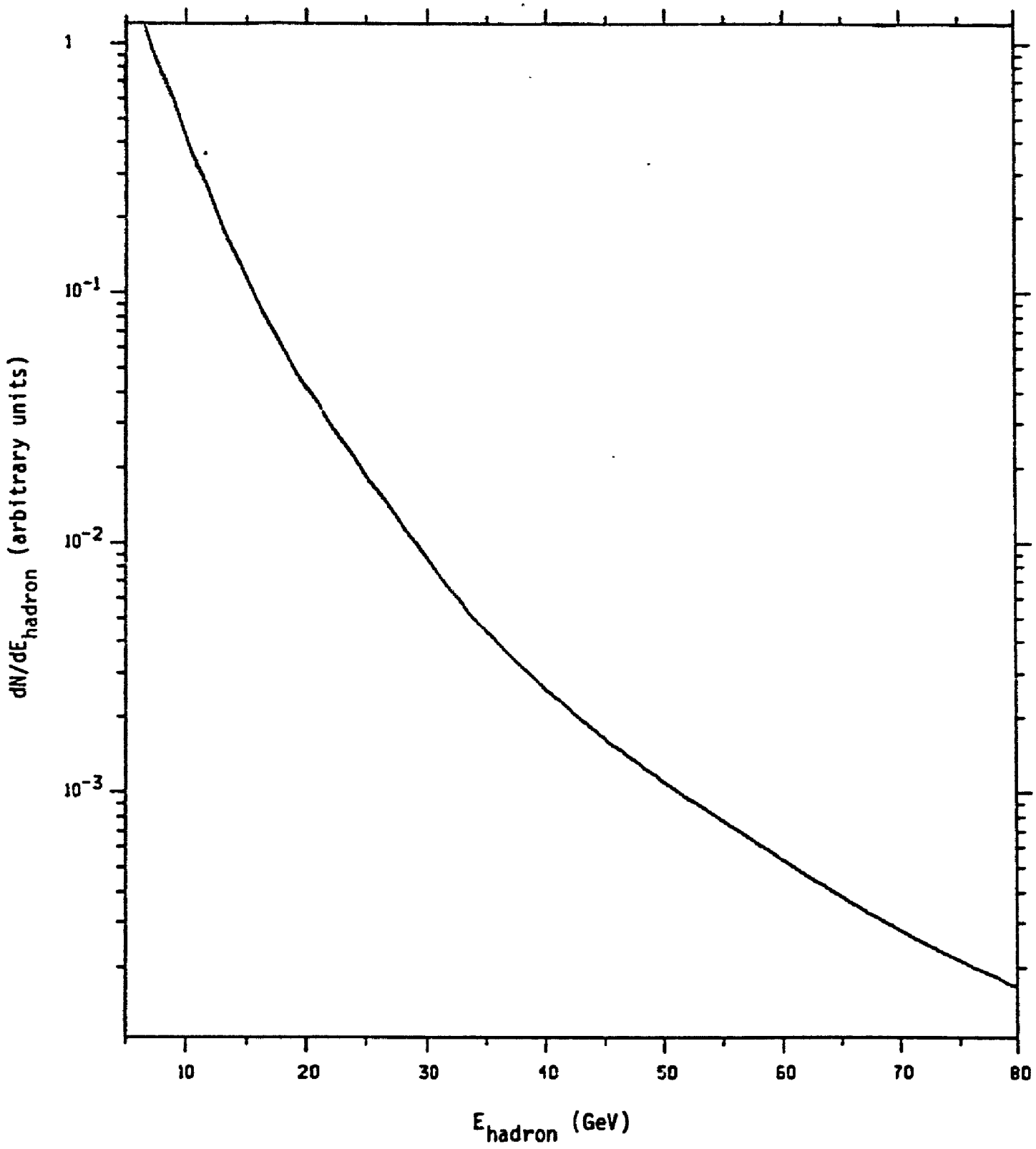
1
10^{-1}
10^{-2}
10^{-3}
dN/dE_{hadron} (arbitrary units)
10
20
30
40
50
60
70
80
E_{hadron} (GeV)

Figure 31.

Figure 32.-- Muon momentum along z axis for decay muon from simulated showers.

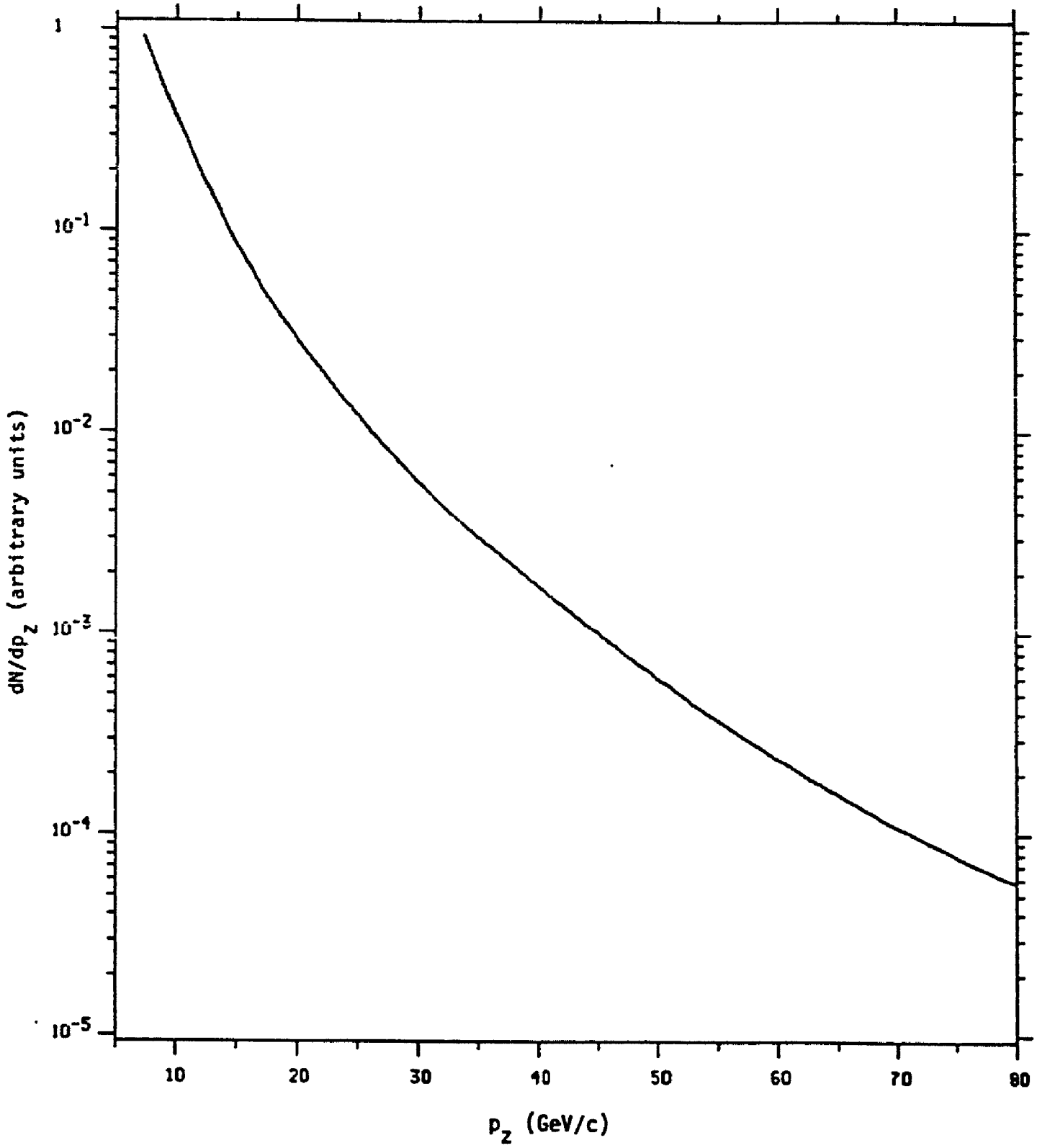
1
10^{-1}
10^{-2}
10^{-3}
10^{-4}
10^{-5}
dN/dp_z (arbitrary units)
10
20
30
40
50
60
70
80
p_z (GeV/c)

Figure 32.

Figure 33.-- Energy of produced muons for simulated shower events satisfying the dimuon trigger.

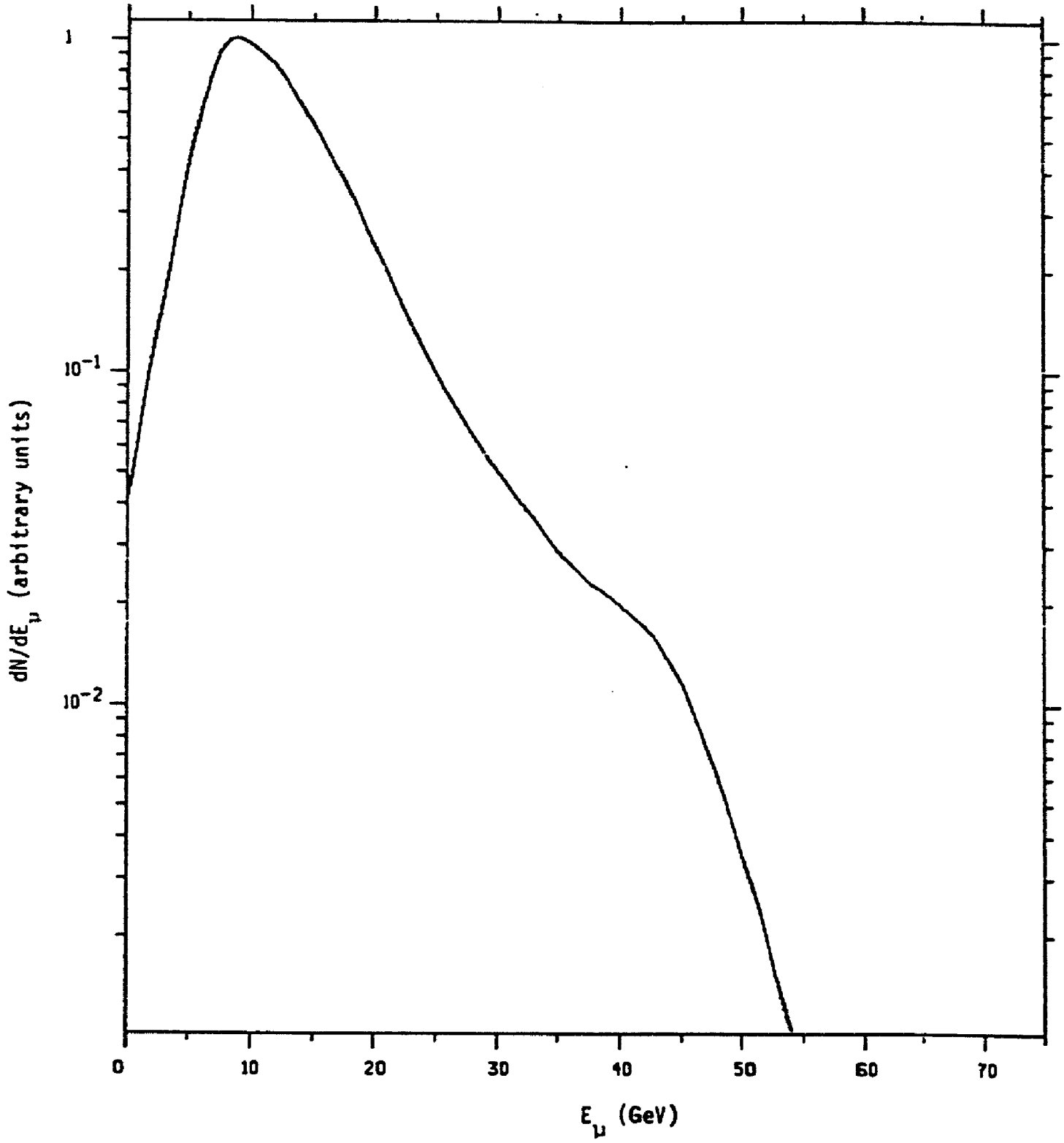

Figure 33.

Figure 34.-- Momentum perpendicular to the virtual photon for produced muons at the decay point in simulated shower events satisfying the dimuon trigger.

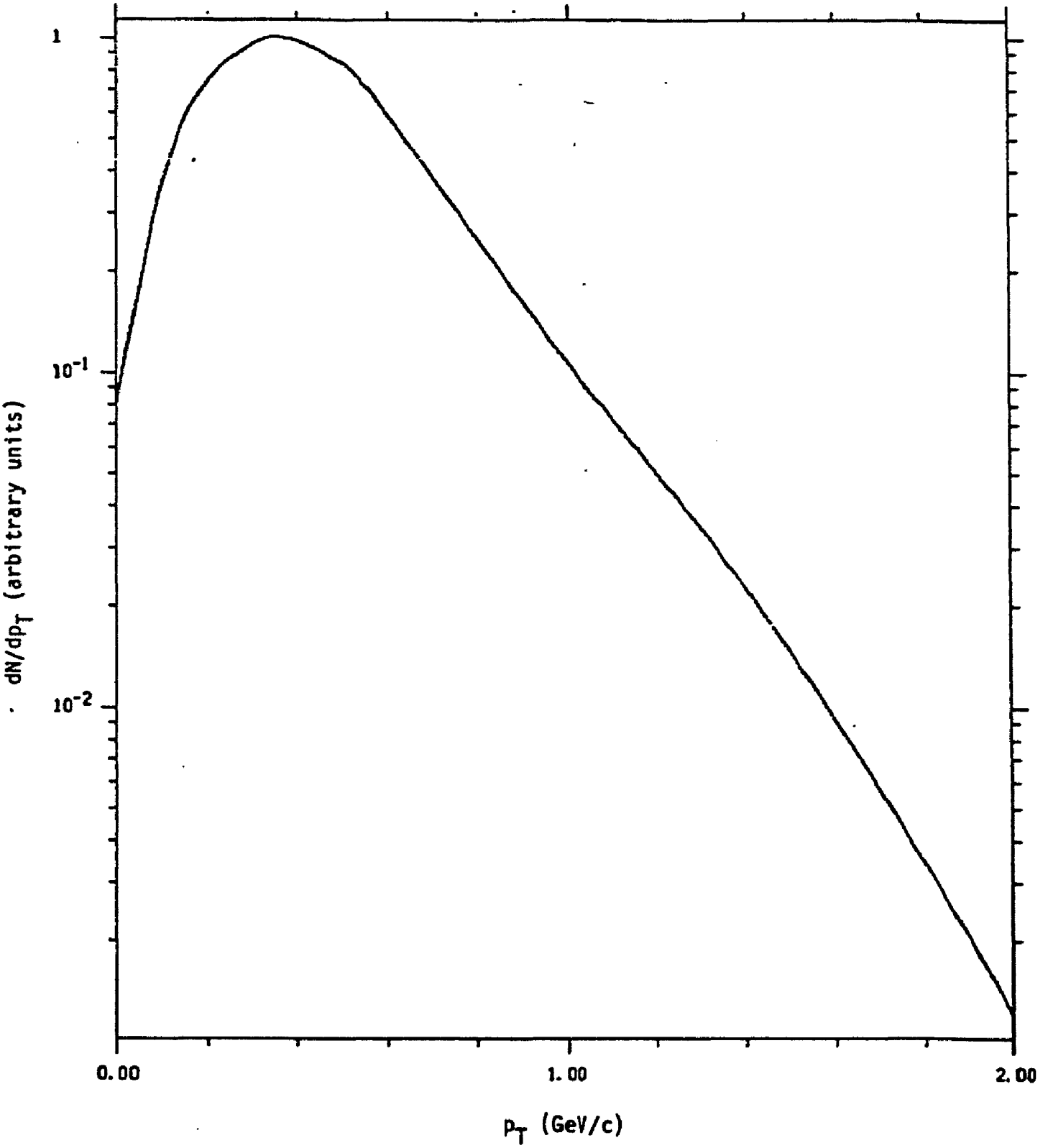

Figure 34.

Figure 35.-- Neutrino energy for simulated shower events satisfying the dimuon trigger.

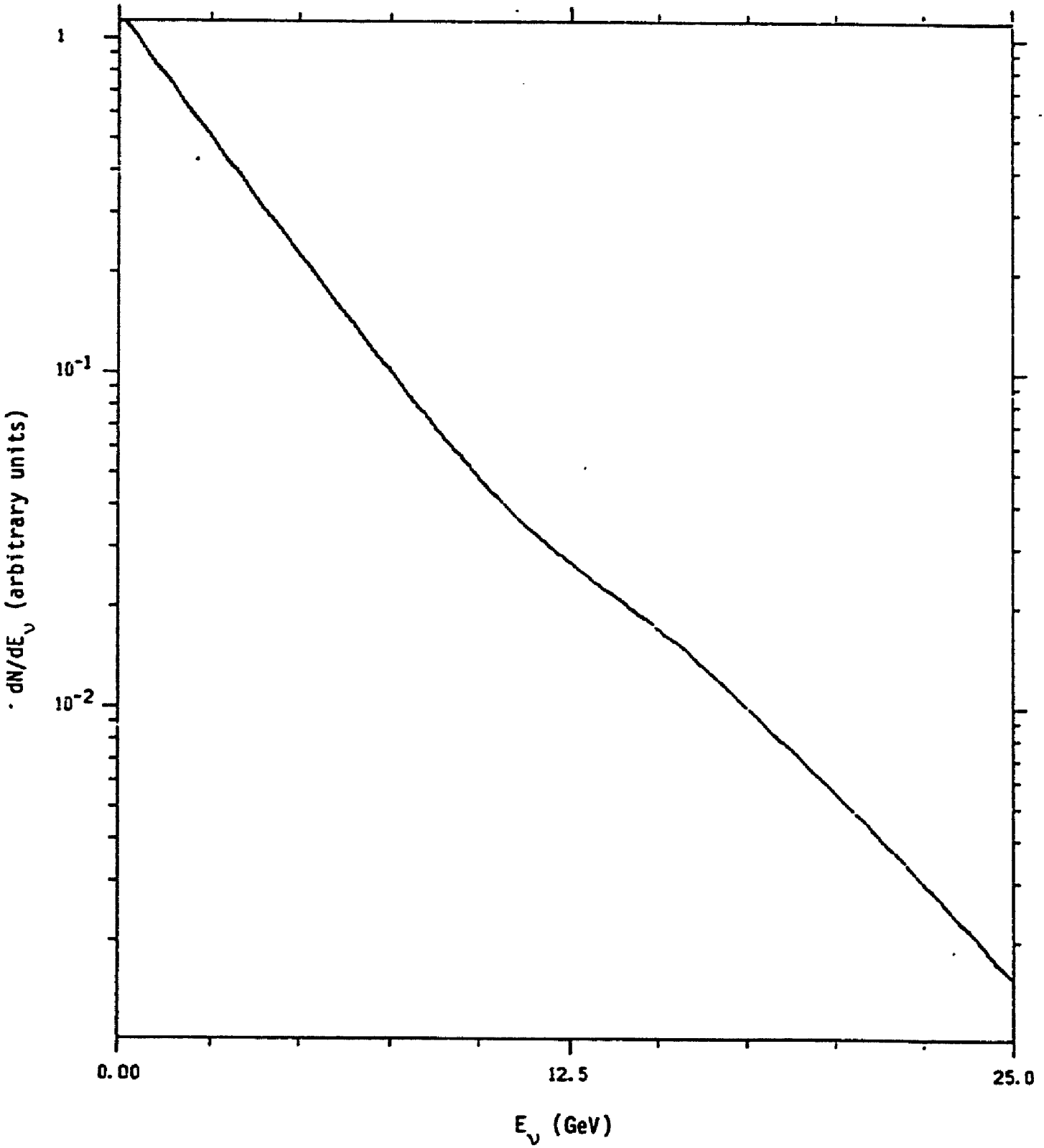

Figure 35.

Figure 36.-- Feynman diagrams for muon trident production calculated by Barger, Keung, and Phillips.[55] (a) Bethe-Heitler production; (b) Muon bremsstrahlung; (c) Target bremsstrahlung.

(a) Bethe-Heitler

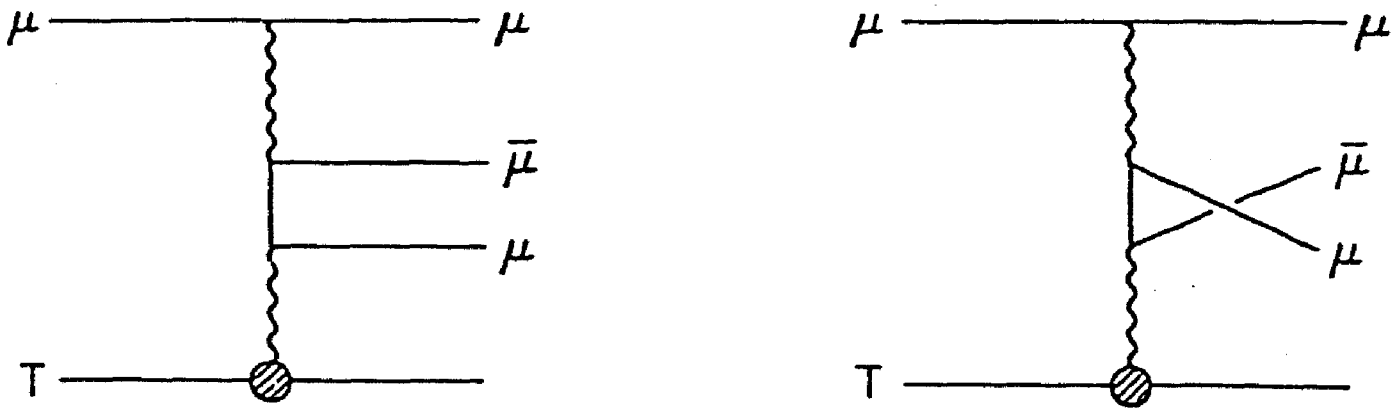

(b) Muon-Bremsstrahlung

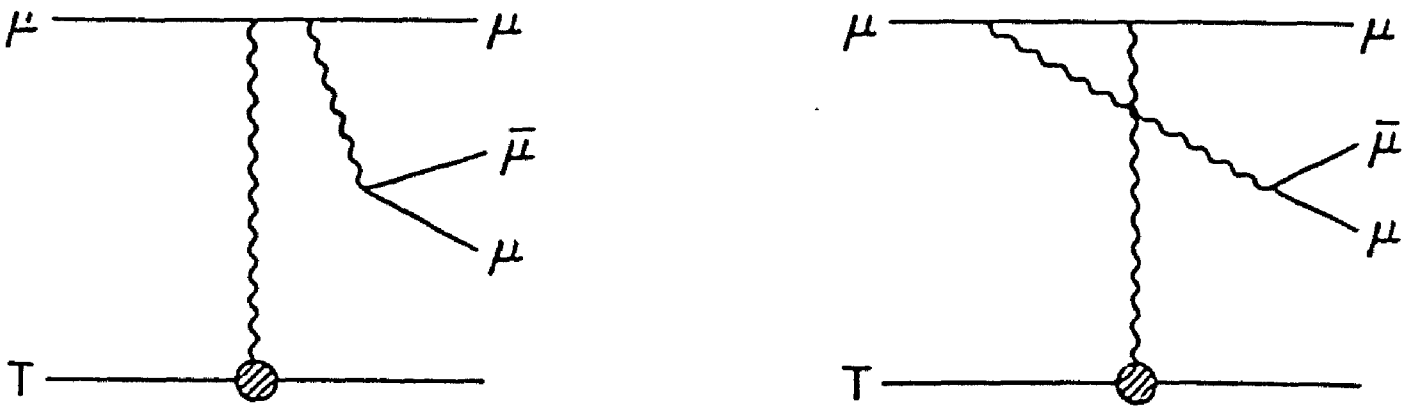

(c) Target-Bremsstrahlung

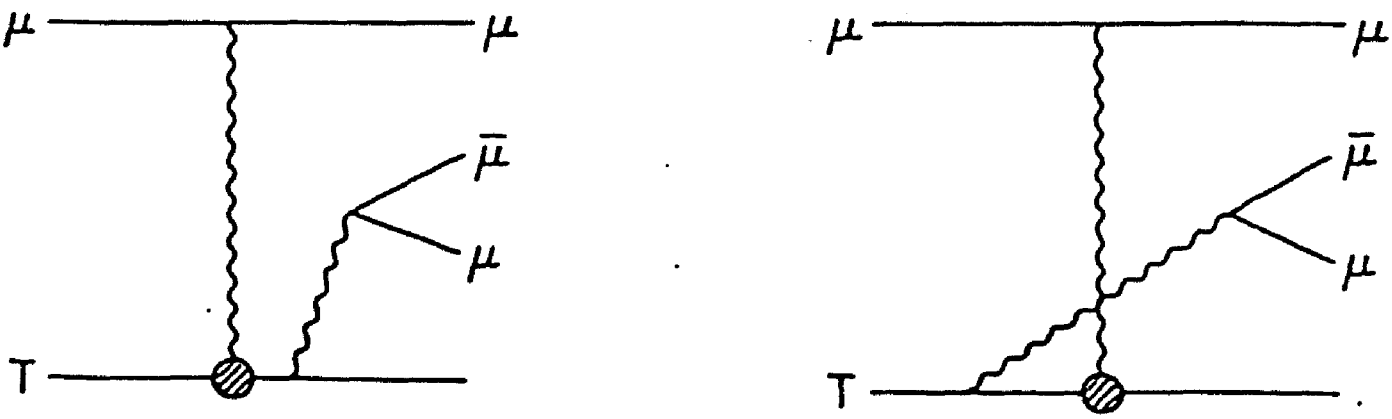

Figure 36.

Figure 37.-- Distributions in daughter muon energy for background- subtracted data, charm Monte Carlo, and π, K-decay Monte Carlo. The ordinate represents events per bin with acceptance not unfolded. The inverted histogram shows the simulated π, K-decay background, normalized to the beam flux. The upright histogram represents background-subtracted data. Errors are statistical. The curve, normalized to the data after analysis cuts, is the photon-gluon-fusion charm calculation. Events satisfy standard cuts described in the text except they have $\nu > 150$ GeV. The unusual ν cut increases the sensitivity of the predictions of the Monte Carlo simulation to assumptions about charmed quark fragmentation. The horizontal bar indicates typical resolution.

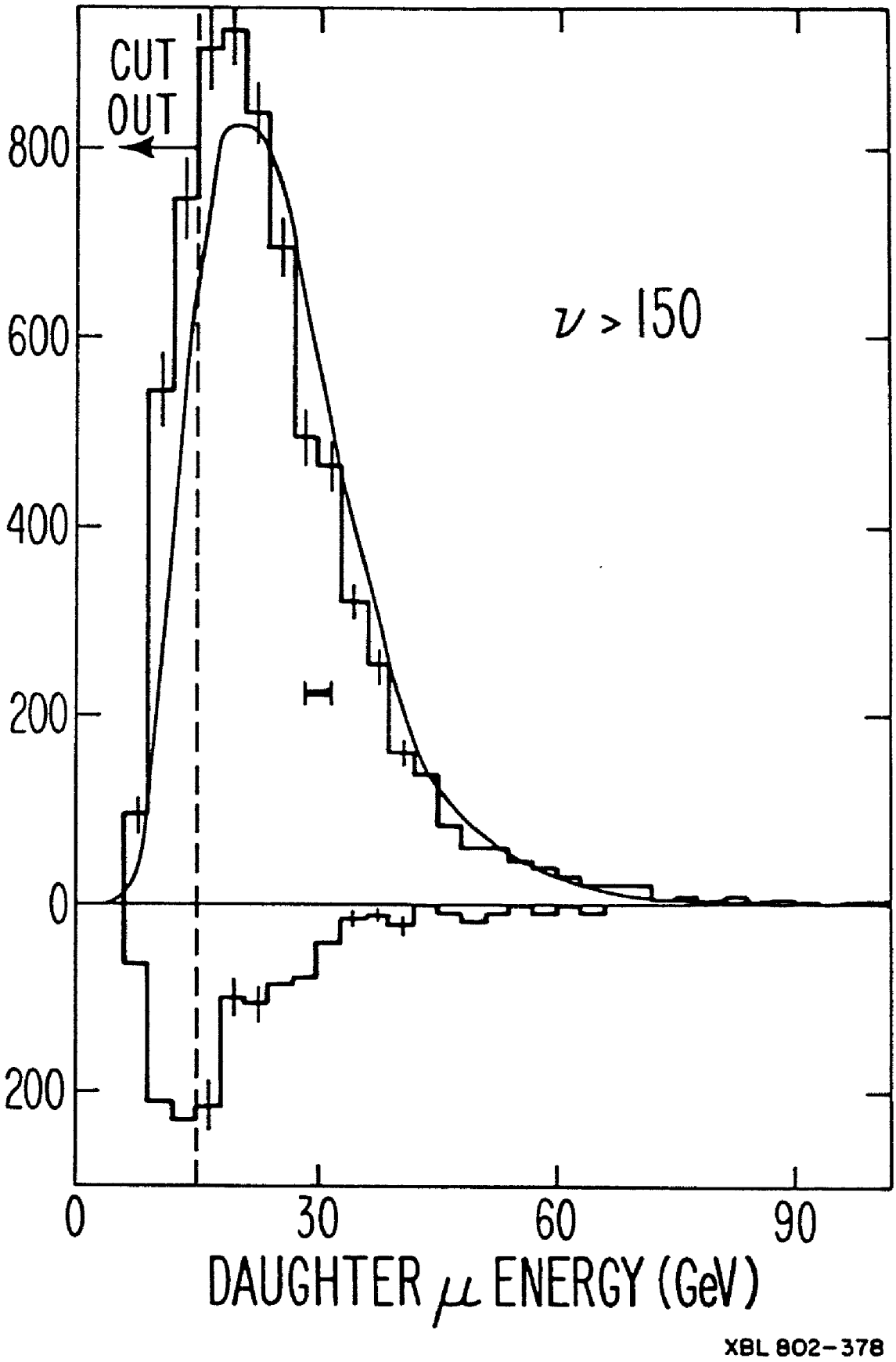
CUT
OUT
800
600
400
200
0
200
$\nu > 150$
0
30
60
90
DAUGHTER μ ENERGY (GeV)
XBL 802-378

Figure 37.

Figure 38.-- Reconstructed vertex distribution for background- subtracted data and charm Monte Carlo. Monte Carlo events were generated only in the upstream ~800 cm of the detector. (a) The histogram shows subtracted data with Monte Carlo superimposed as x's; (b) The histogram shows Monte Carlo with subtracted data superimposed as x's.

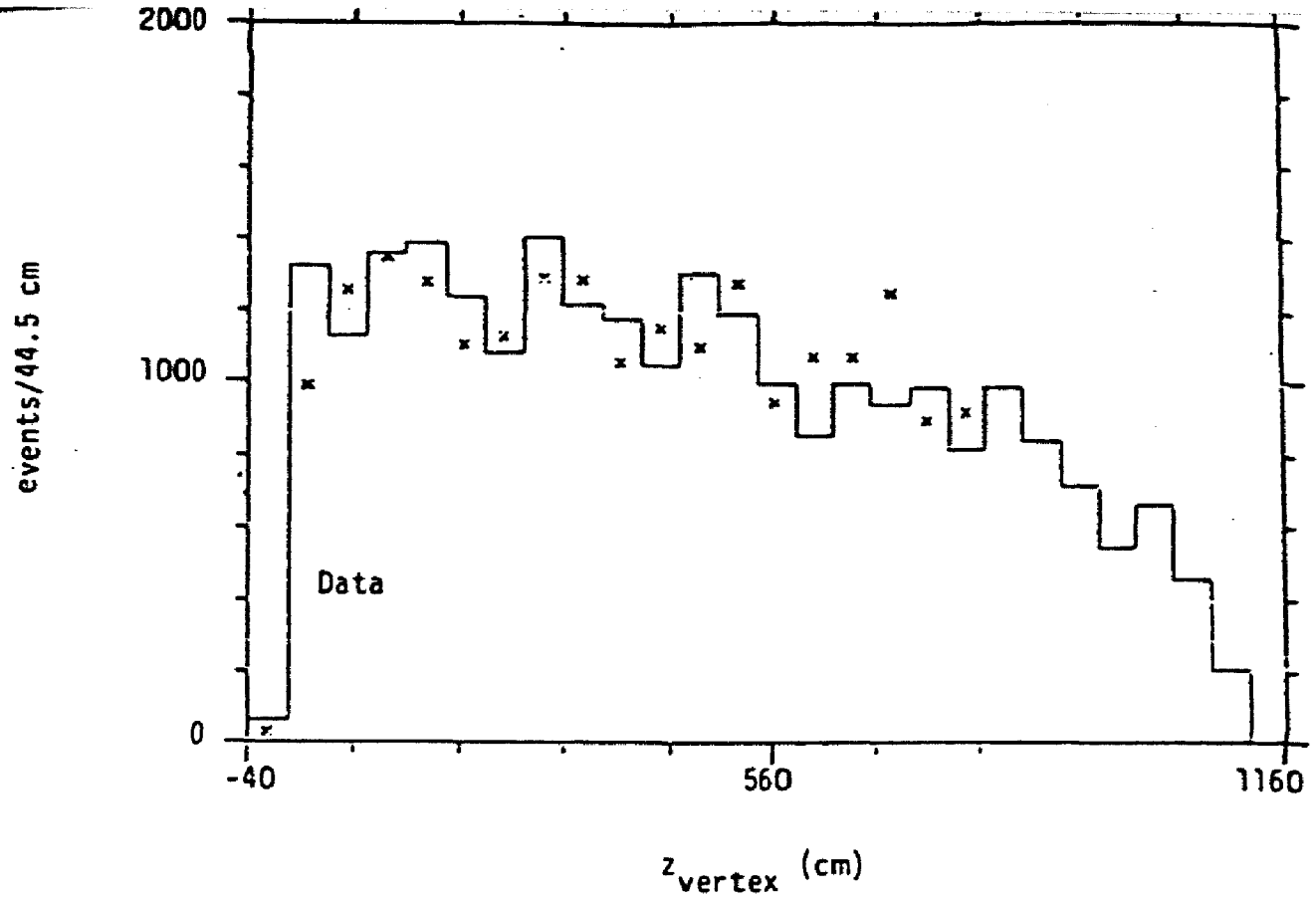
2000
1000
0
events/44.5 cm
Data
-40
560
1160
z_{vertex} (cm)

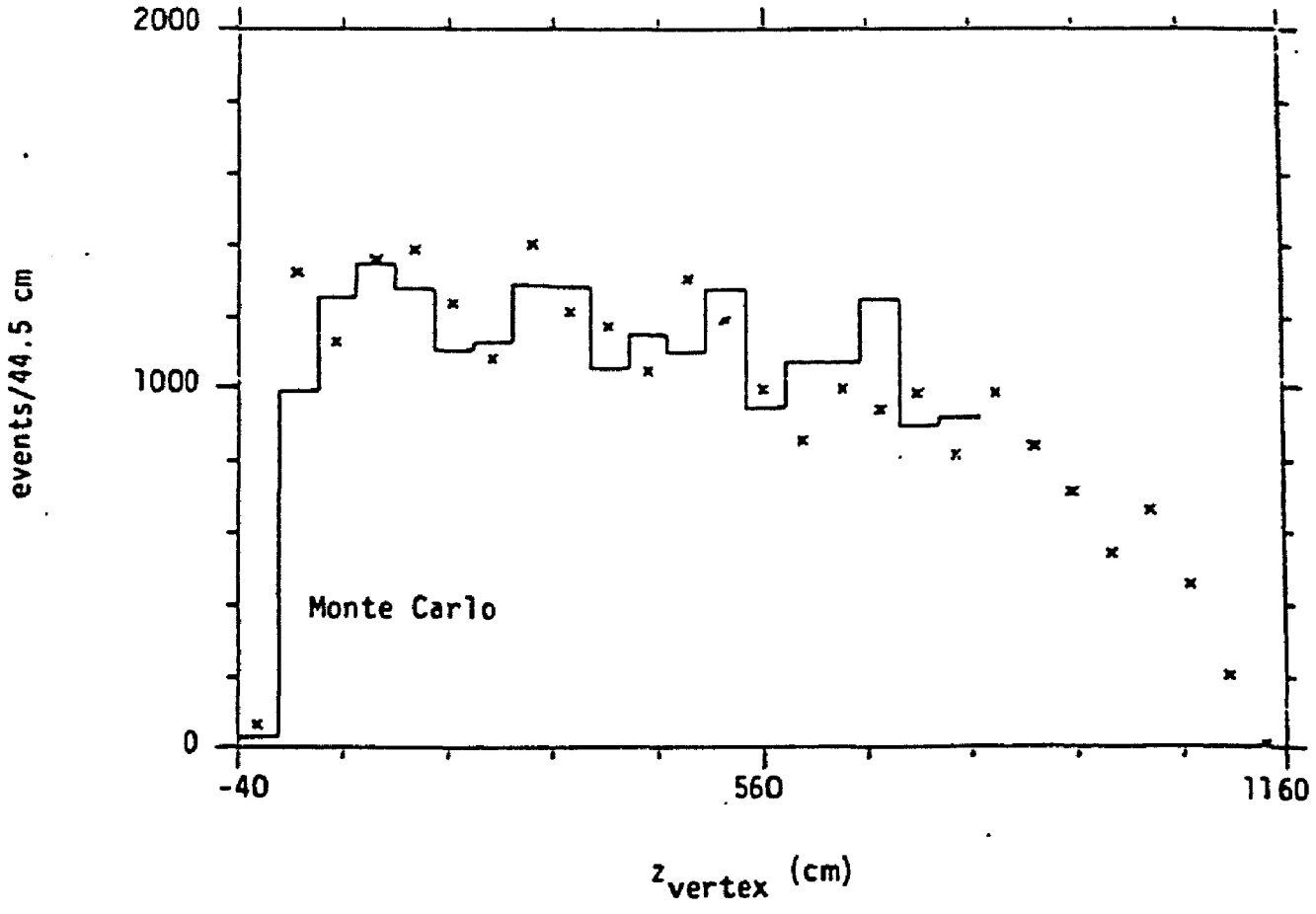
2000
1000
0
events/44.5 cm
Monte Carlo
-40
560
1160
z_{vertex} (cm)

Figure 38.

Figure 39.-- Distributions in daughter muon momentum perpendicular to the virtual photon for background-subtracted data, charm Monte Carlo, and π, K-decay Monte Carlo. The ordinate represents events per bin with acceptance not unfolded. The inverted histogram shows the simulated π, K-decay background, normalized to the beam flux. The upright histogram represents background-subtracted data. Errors are statistical. The curve, normalized to the data after analysis cuts, is the photon-gluon-fusion charm calculation. Events satisfy standard cuts described in the text. The horizontal bar indicates typical resolution.

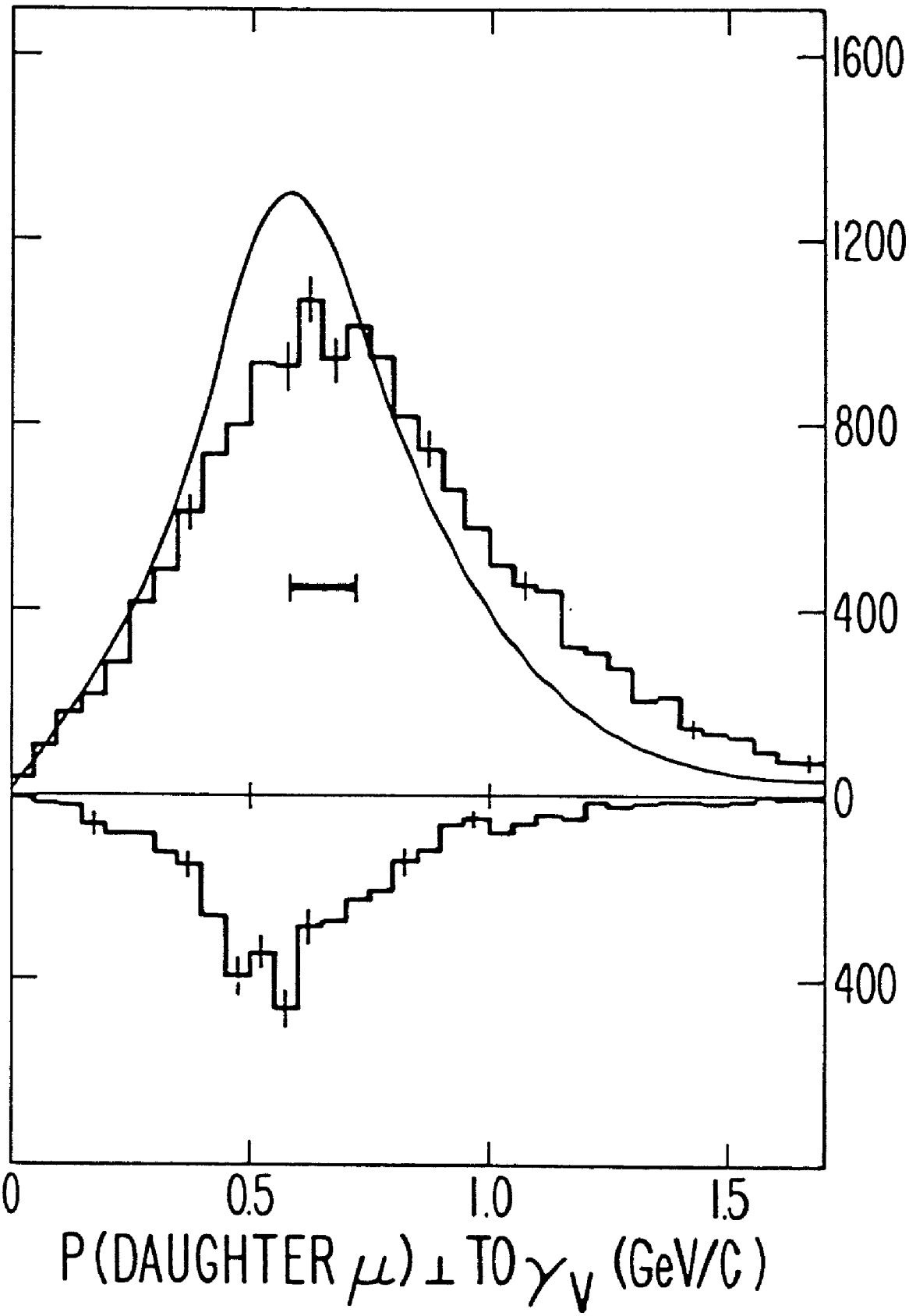
1600
1200
800
400
0
400
0
0.5
1.0
1.5
P(DAUGHTER μ) ⊥ TO γV (GeV/C)
XBL802-381

Figure 39.

Figure 40.-- Distributions in energy transfer for background- subtracted data, charm Monte Carlo, and π, K-decay Monte Carlo. The ordinate represents events per bin with acceptance not unfolded. The inverted histogram shows the simulated π, K-decay background, normalized to the beam flux. The upright histogram represents background-subtracted data. Errors are statistical. The solid curve, normalized to the data after analysis cuts, is the photon-gluon- fusion charm calculation. The dashed curve represents an alternative model in which $D\bar{D}$ pairs are produced with a hard fragmentation function and a probability independent of ν. Events satisfy standard cuts described in the text except that no ν cut is imposed. The horizontal bar indicates typical resolution.

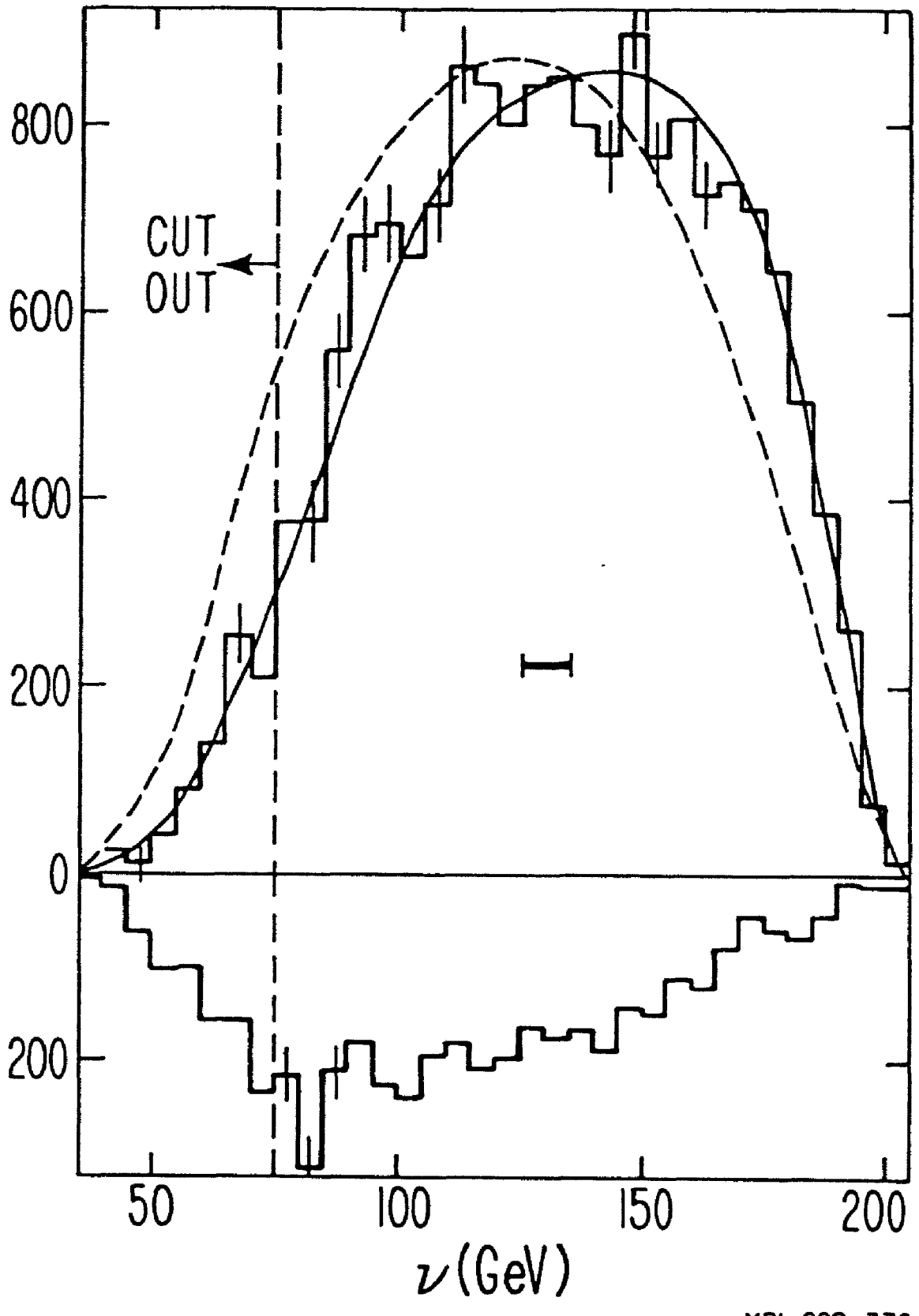

Figure 40.

Figure 41.-- Distributions in momentum transfer-squared for background- subtracted data, charm Monte Carlo, and π, K-decay Monte Carlo. The ordinate represents events per bin with acceptance not unfolded. The inverted histogram shows the simulated π, K-decay background, normalized to the beam flux. The upright histogram represents background-subtracted data. Errors are statistical. The curve, normalized to the data after analysis cuts, is the photon-gluon- fusion charm calculation. Events satisfy standard cuts described in the text. The horizontal bars indicate typical resolution.

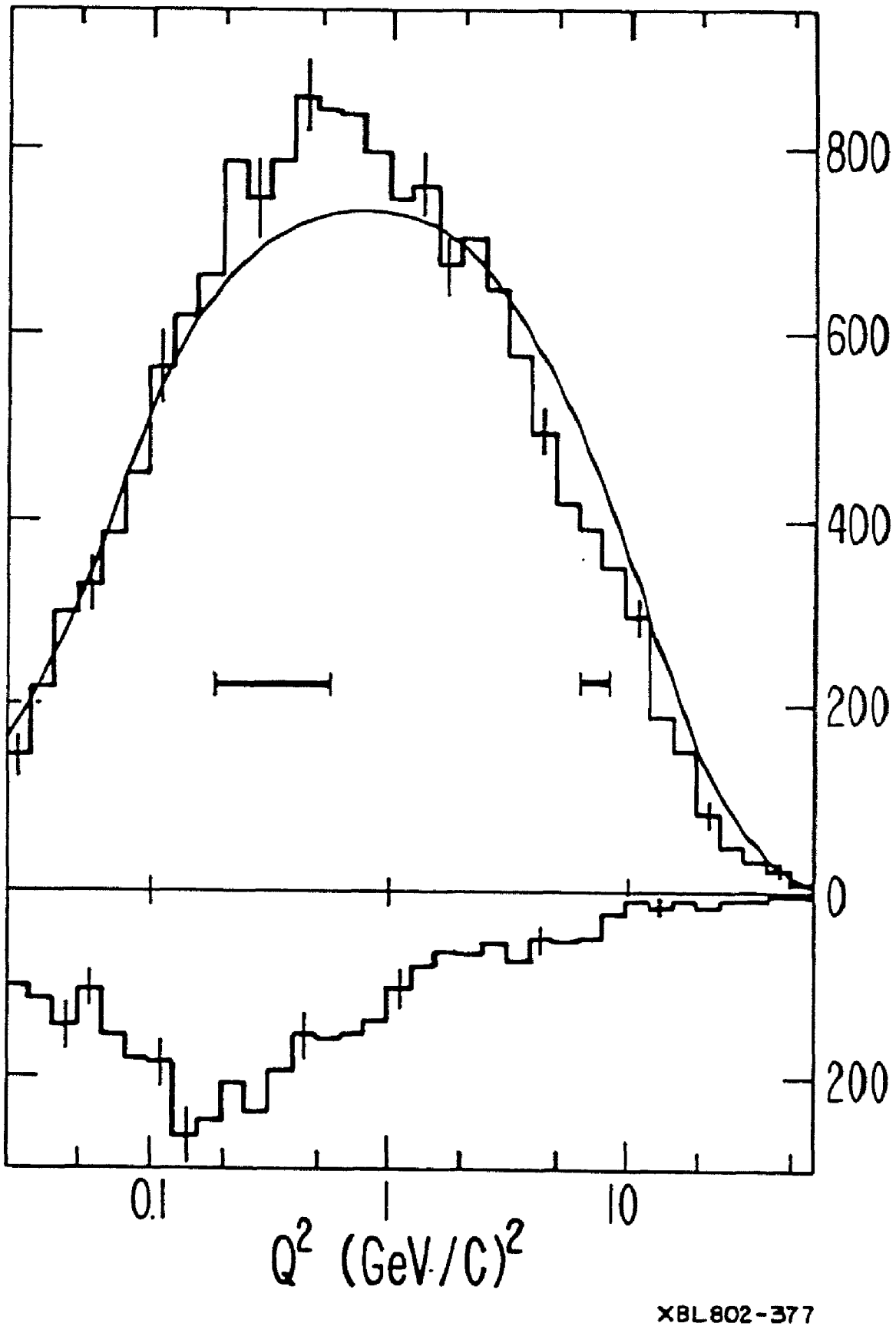

Figure 41.

Figure 42.-- Distributions in missing (neutrino) energy for background- subtracted data, charm Monte Carlo, and π, K-decay Monte Carlo. The ordinate represents events per bin with acceptance not unfolded. The inverted histogram shows the simulated π, K-decay background, normalized to the beam flux. The upright histogram represents background-subtracted data. Errors are statistical. The curve, normalized to the data after analysis cuts, is the photon-gluon- fusion charm calculation. Events satisfy standard cuts described in the text. The horizontal bar indicates typical rms resolution. The arrow indicates the shift in the centroid of the data caused by a $\pm$2.5% change in the calorimeter calibration.

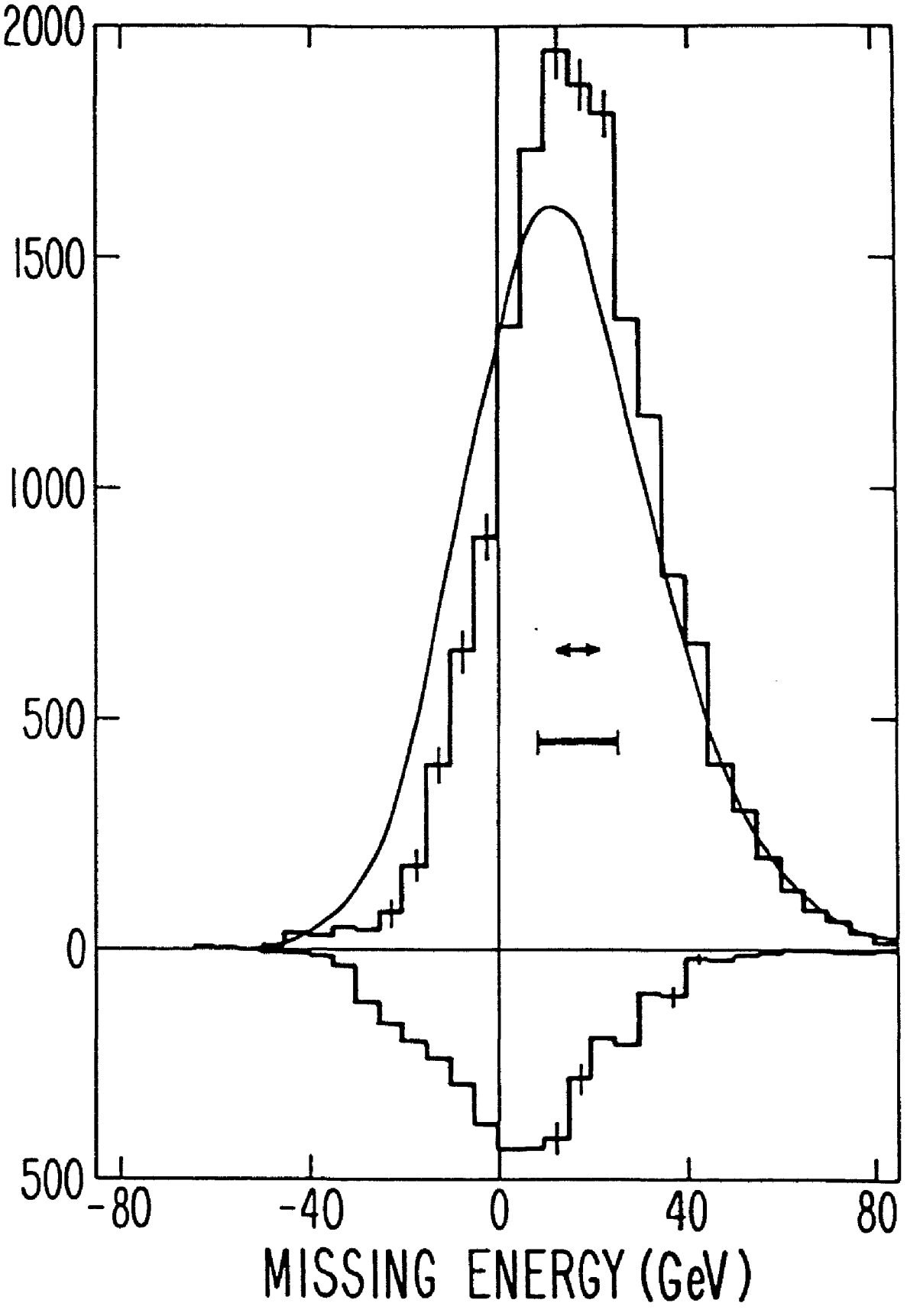

XBL 802-380

Figure 42.

Figure 43.-- Distributions in inelasticity for background- subtracted data, charm Monte Carlo, and π, K-decay Monte Carlo. The ordinate represents events per bin with acceptance not unfolded. The inverted histogram shows the simulated π, K-decay background, normalized to the beam flux. The upright histogram represents background-subtracted data. Errors are statistical. The curve, normalized to the data after analysis cuts, is the photon-gluon- fusion charm calculation. Events satisfy standard cuts described in the text.

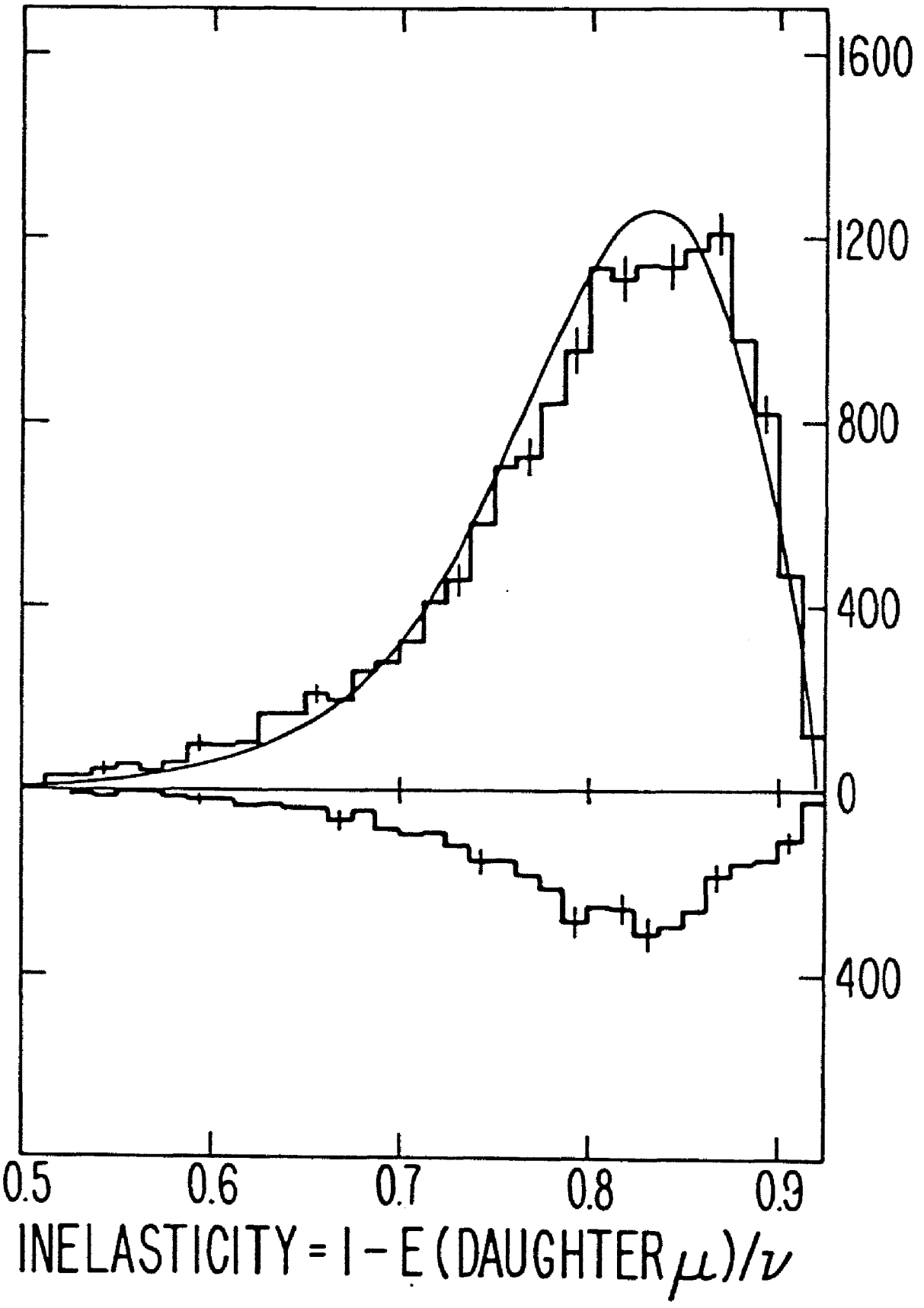

XBL 802-379

Figure 43.

Figure 44.-- Flux of transversely polarized virtual photons accompanying a 209 GeV muon. The flux is in units of c^2 GeV^{-3} and represents the number of photons per unit interval of Q^2 and ν. Shown in the figure is Q^2 times the flux.

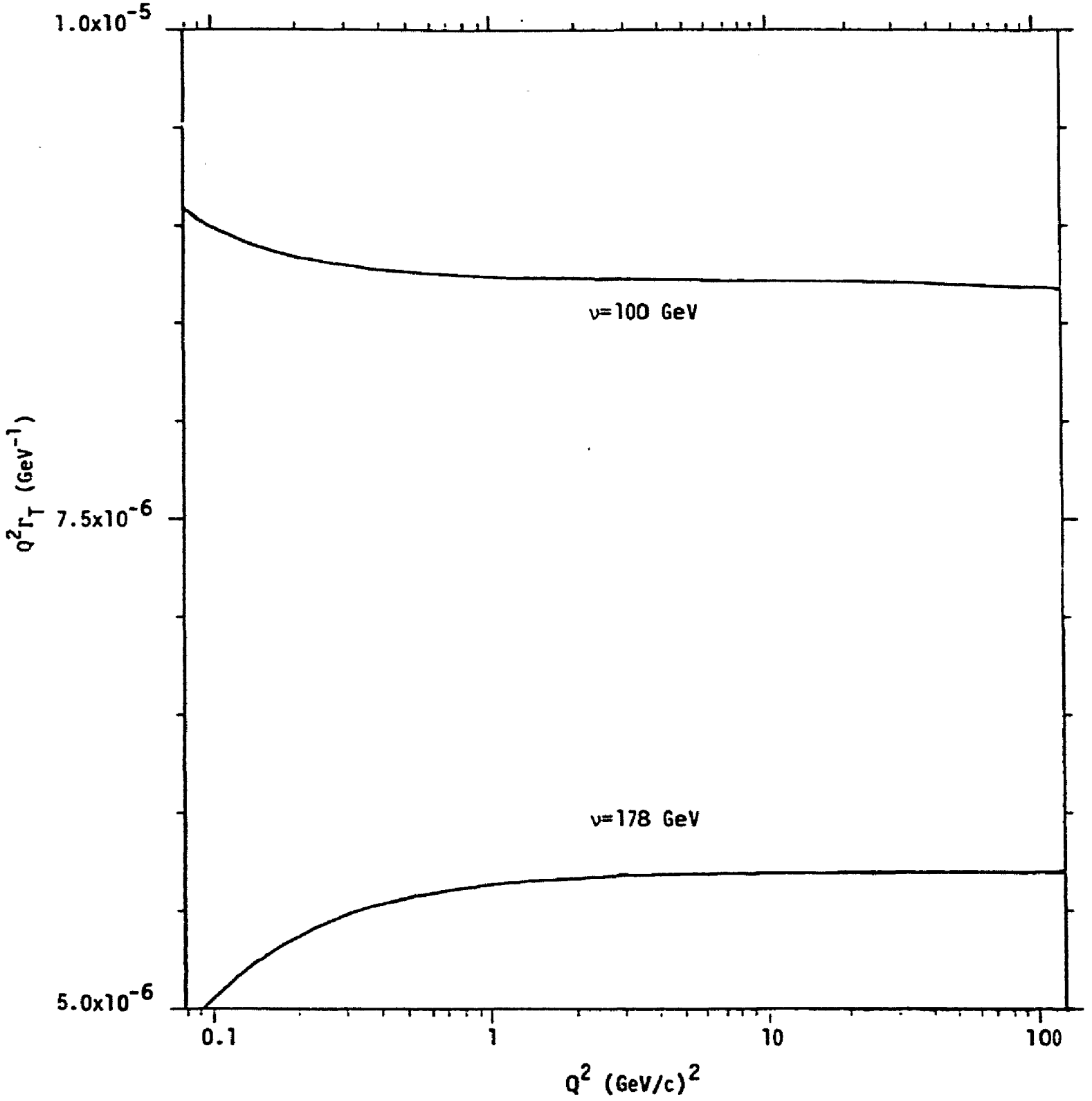
1.0x10^-5
7.5x10^-6
5.0x10^-6
Q^2Γ_T (GeV^-1)
ν=100 GeV
ν=178 GeV
0.1
1
10
100
Q^2 (GeV/c)^2

Figure 44.

Figure 45.-- Virtual photon polarization ϵ. The muon beam energy is 209 GeV.

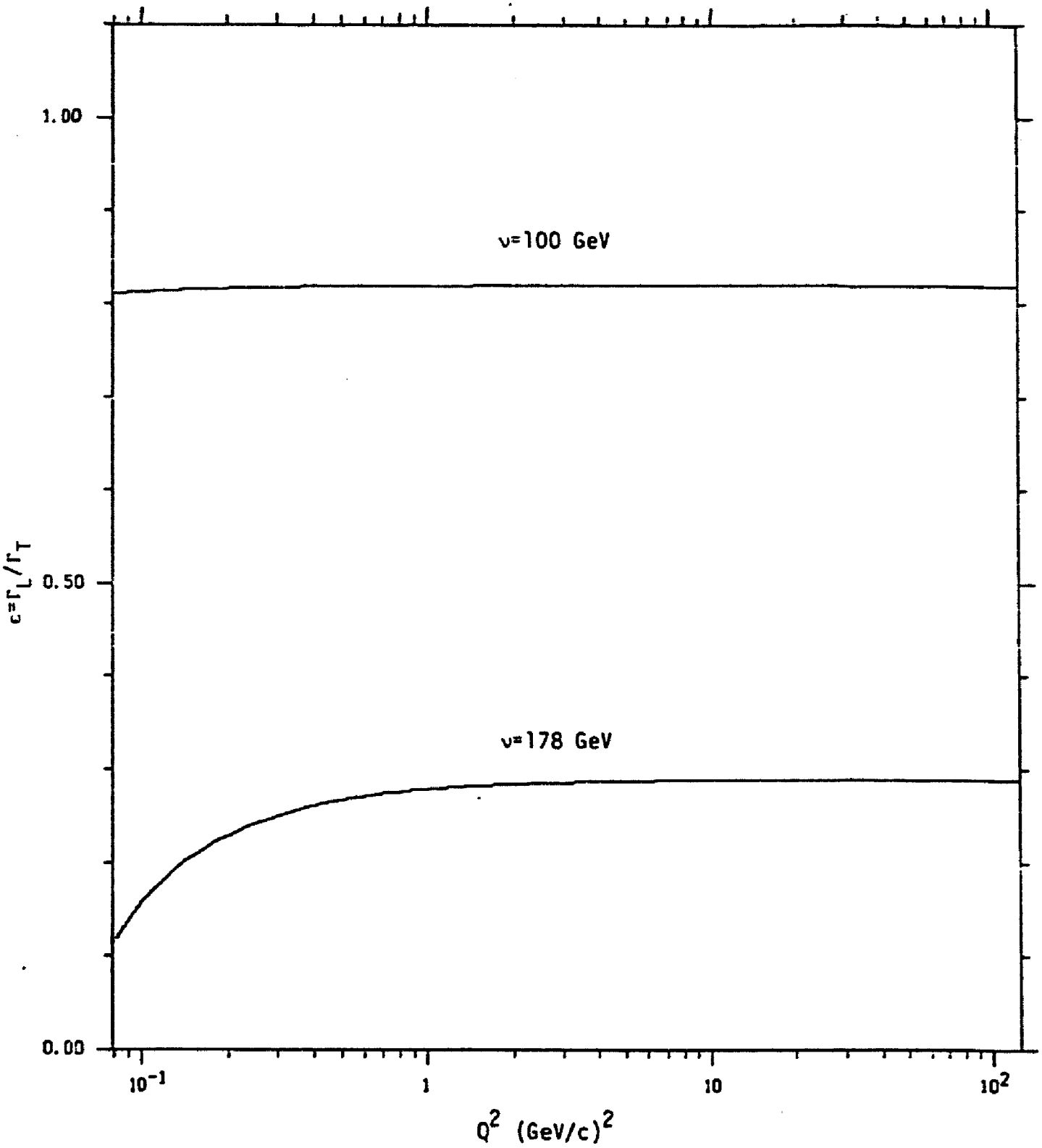
1.00
0.50
0.00
$\varepsilon = \Gamma_L/\Gamma_T$
ν=100 GeV
ν=178 GeV
10^{-1}
1
10
10^2
Q^2 (GeV/c)^2

Figure 45.

Figure 46.--σ_L/σ_T in the photon-gluon- fusion model. σ_L (σ_T) is the probability for a longitudinally (transversely) polarized virtual photon to produce charm through the reaction $\gamma N \rightarrow c\bar{c}X$.

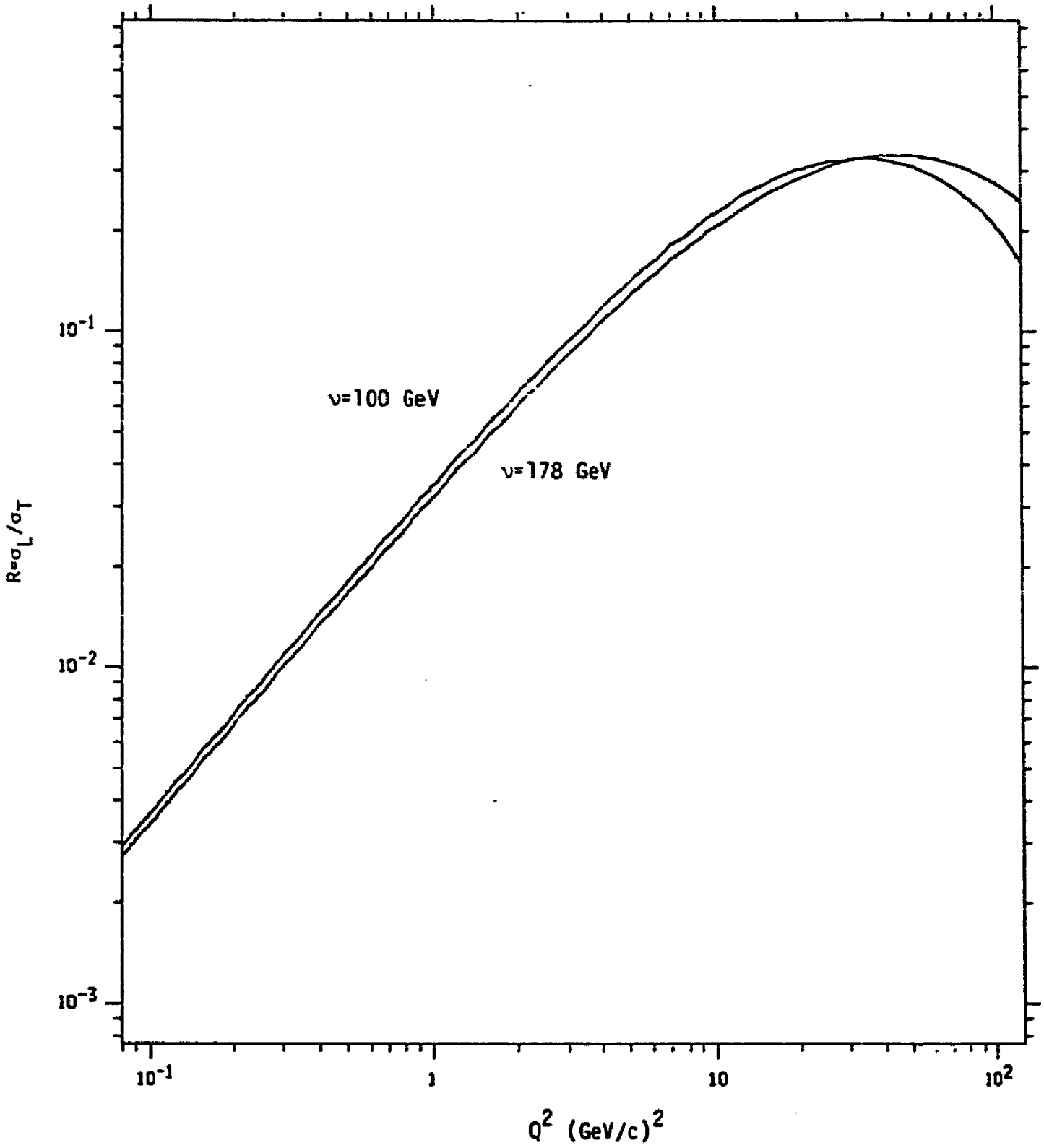
10^{-1}
10^{-2}
10^{-3}
$R=\sigma_L/\sigma_T$
ν=100 GeV
ν=178 GeV
10^{-1}
1
10
10^2
Q^2 (GeV/c)^2

Figure 46.

Figure 47.-- ϵR in the photon-gluon-fusion model. R is σ_L / σ_T; ϵ is the virtual photon polarization (see figures 45 and 46).

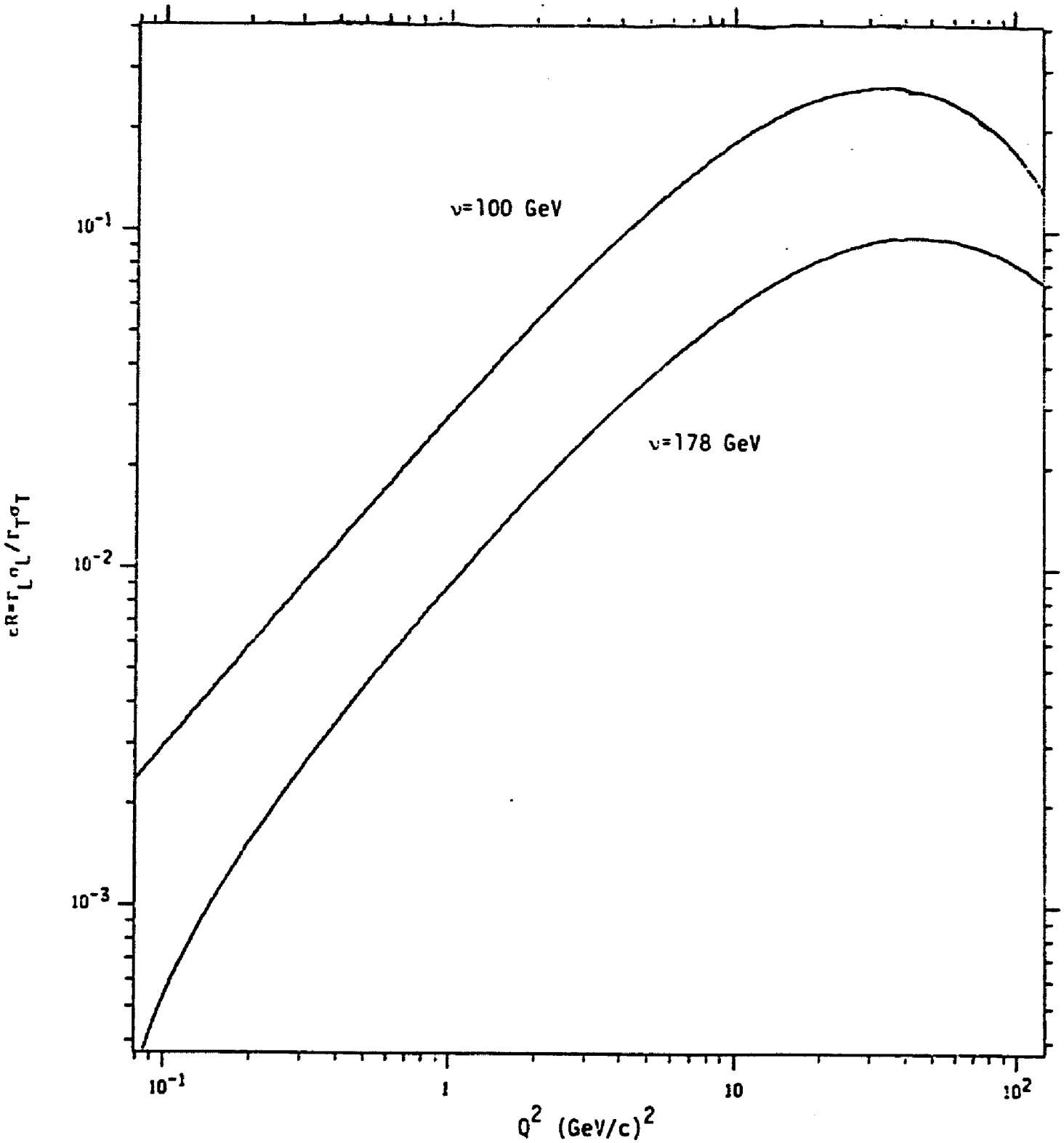
ν=100 GeV
ν=178 GeV
10^{-1}
10^{-2}
10^{-3}
$\sigma_R = \Gamma_L \sigma_L / \Gamma_T \sigma_T$
10^{-1}
1
10
10^2
Q^2 (GeV/c)^2

Figure 47.

Figure 48.-- Diffractive charm photoproduction cross sections. Parts (a) and (b) show the extrapolation of the effective cross section to $Q^2=0$ at $\nu=$ (a) 178 and (b) 100 GeV. Errors are statistical. The solid curves are fits to $\sigma(o)(1+Q^2/\Lambda^2)^{-2}$, with $\Lambda=$ (a) 3.3 and (b) 2.9 GeV/c; the arrows labeled "NOM" exhibit $\sigma(o)$. Systematic errors are parametrized by (1) decreasing, (2) increasing by 50% the subtracted π, K-decay background, and by recalculating acceptance with a (3) softer, (4) harder fragmentation as described in the text. The effects on $\sigma(o)$ are indicated by the numbered arrows and the effects on Λ are indicated by the dashed curves, normalized to the same $\sigma(o)$. Horizontal bars show typical rms resolution.

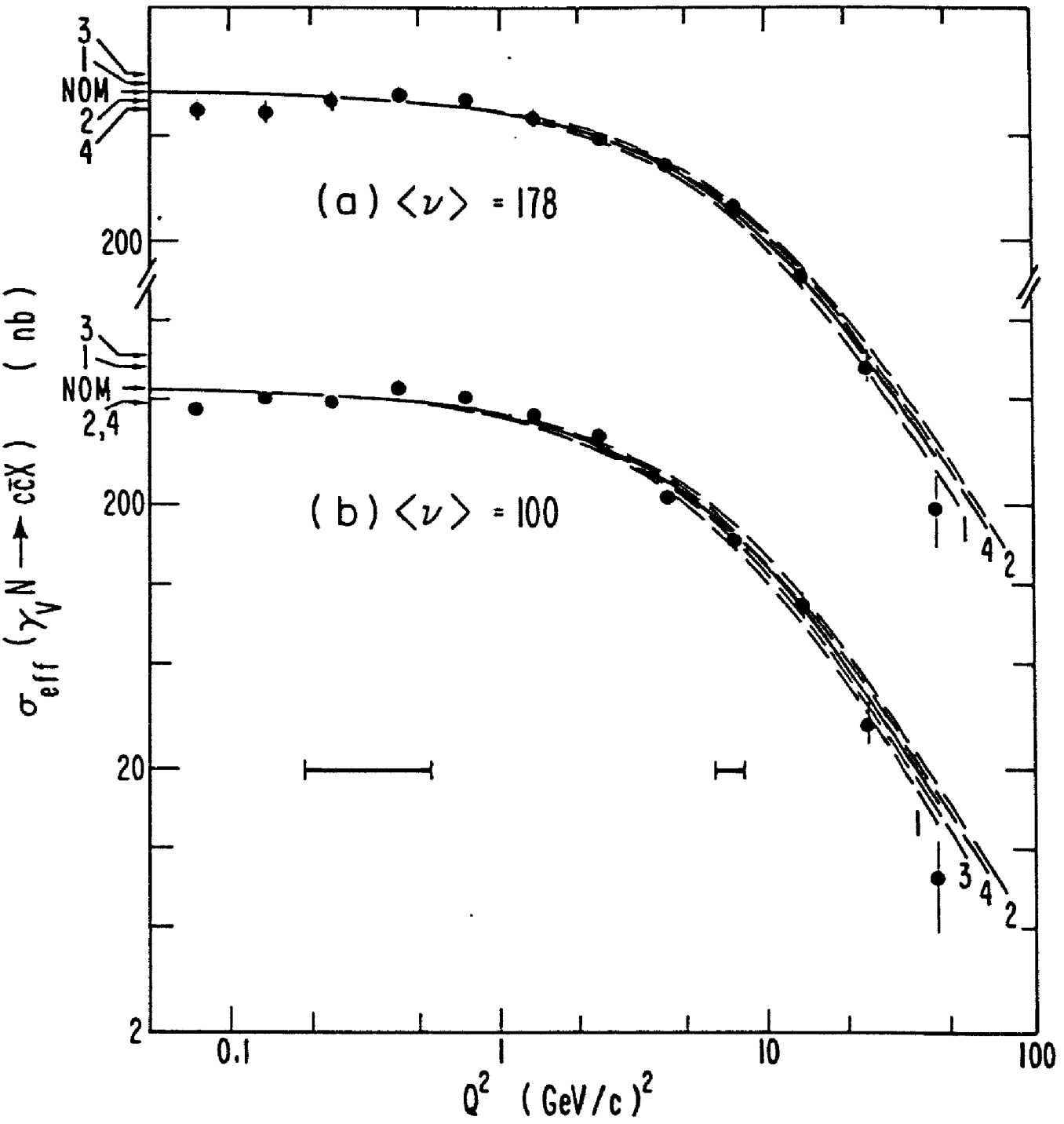

XBL 803-384

Figure 48.

Figure 49.-- The role of charm in the rise of the γN total cross section. Data points representing the effective photon cross section (right scale) are compared with a fit from Ref. 64 to half the photon-deuteron cross section (curve, left scale). Systematic uncertainties dominate the errors.

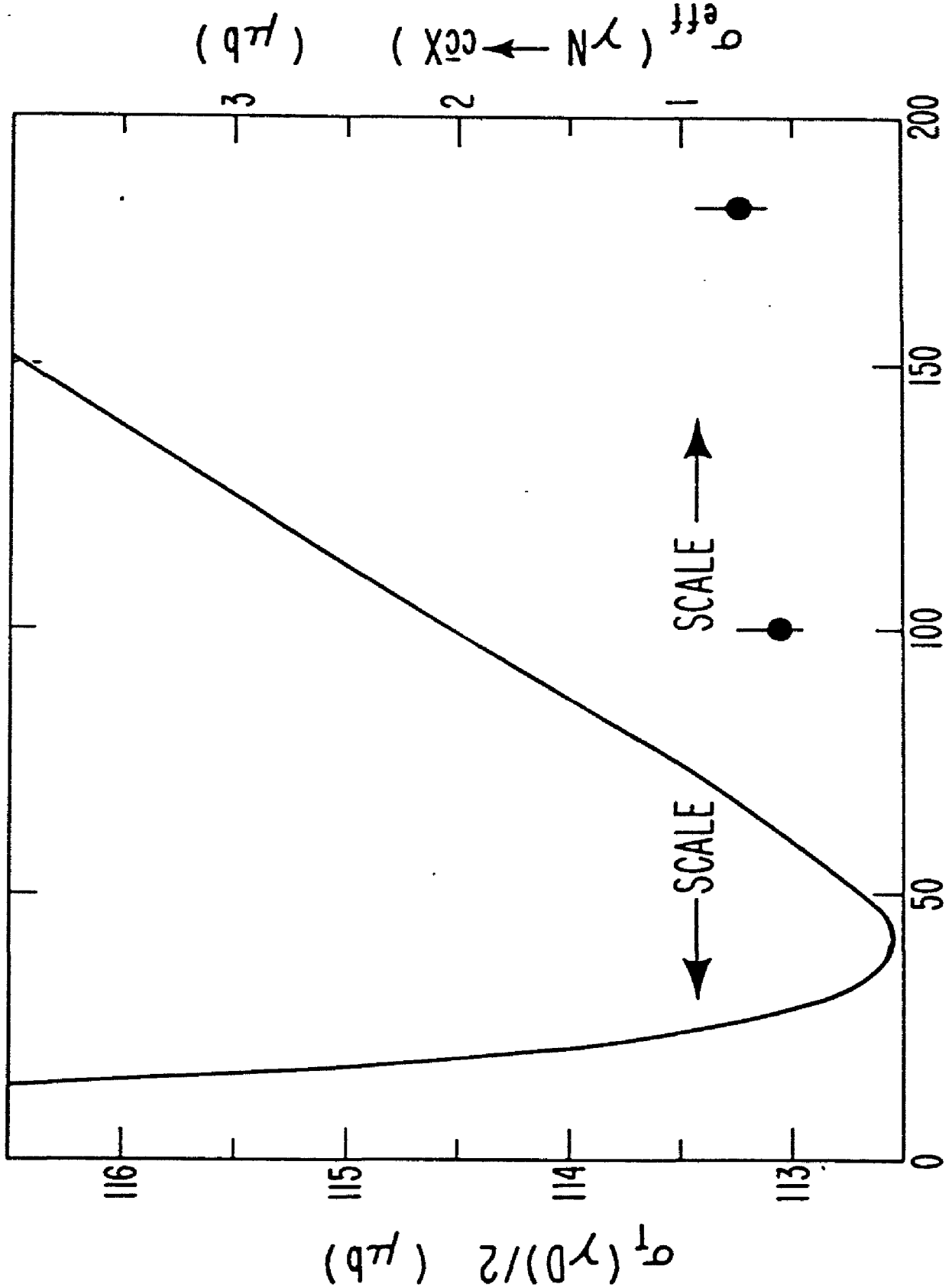

XBL803-383

Figure 49.

Figure 50.-- Energy-dependence of the effective cross section for diffractive charm photoproduction. For $0.32<Q^2<1.8(\mathrm{GeV/c})^2$, σ_{eff} varies with Q^2 by $\lesssim 20\%$. Errors are statistical. The solid curve exhibits the ν-dependence of the photon-gluon-fusion model with the "counting-rule" gluon x_g distribution $3(1-x_g)^5/x_g$, and represents the data with 13% confidence. Other gluon-distribution choices $(1-x_g)^9/x_g$, and "broad glue" $(1-x_g)^5(13.5+1.07/x_g)$ (Ref. 17) are indicated by dashed curves. The dashed curve labeled BN is the phenomenological parametrization of Ref. 66, and the dashed horizontal line represents energy-independence. Curves are normalized to the data. The shaded band exhibits the range of changes in shape allowed by systematic uncertainies. For visual clarity it is drawn relative to the solid curve. Data below $\nu = 75$ GeV are excluded from further analysis.

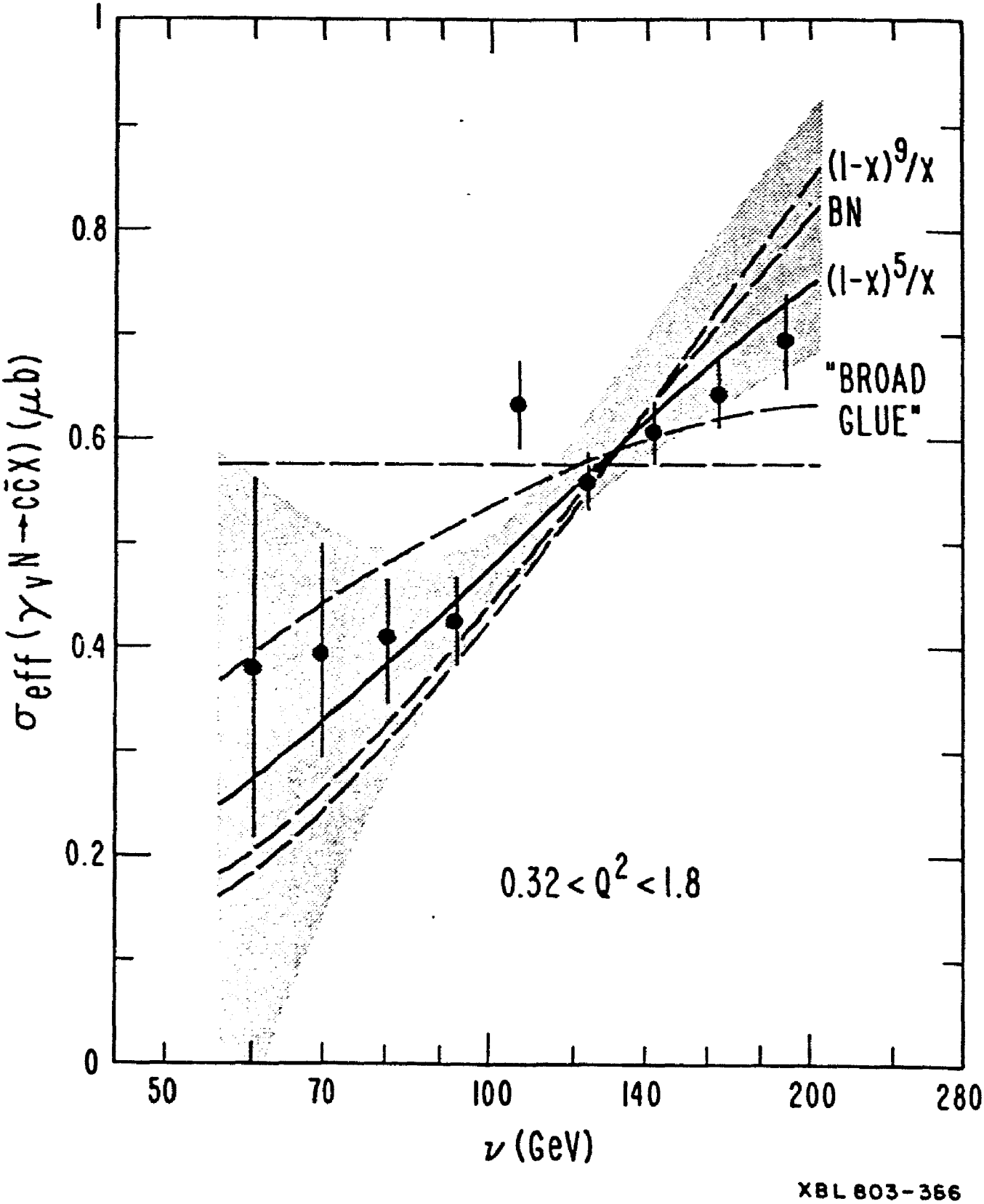
$\sigma_{eff}(\gamma_V N \to c\bar{c}X)$ (μb)
ν (GeV)
$(1-x)^9/x$
BN
$(1-x)^5/x$
"BROAD GLUE"
$0.32 < Q^2 < 1.8$
0
0.2
0.4
0.6
0.8
1
50
70
100
140
200
280
XBL 803-366

Figure 50.

Figure 51.-- Q^2 dependence of the structure function $F_2(c\bar{c})$ for diffractive charm muoproduction. At each of the two average photon energies, each curve is normalized to the data. Errors are statistical. The solid (short dashed) curves labeled m_c=1.5 (1.2) exhibit the photon-gluon-fusion model prediction with a charmed quark mass of 1.5 (1.2) GeV/c^2. Solid curves labeled ψDM correspond to a ψ-dominance propagator, and long-dashed curves labeled BN represent the model of Ref. 66. Shown at the top is a fit adapted from Ref. 20 to the inclusive structure function F_2 for isospin-0 muon-nucleon scattering. The shape variations allowed by systematic errors are represented by the shaded bands.

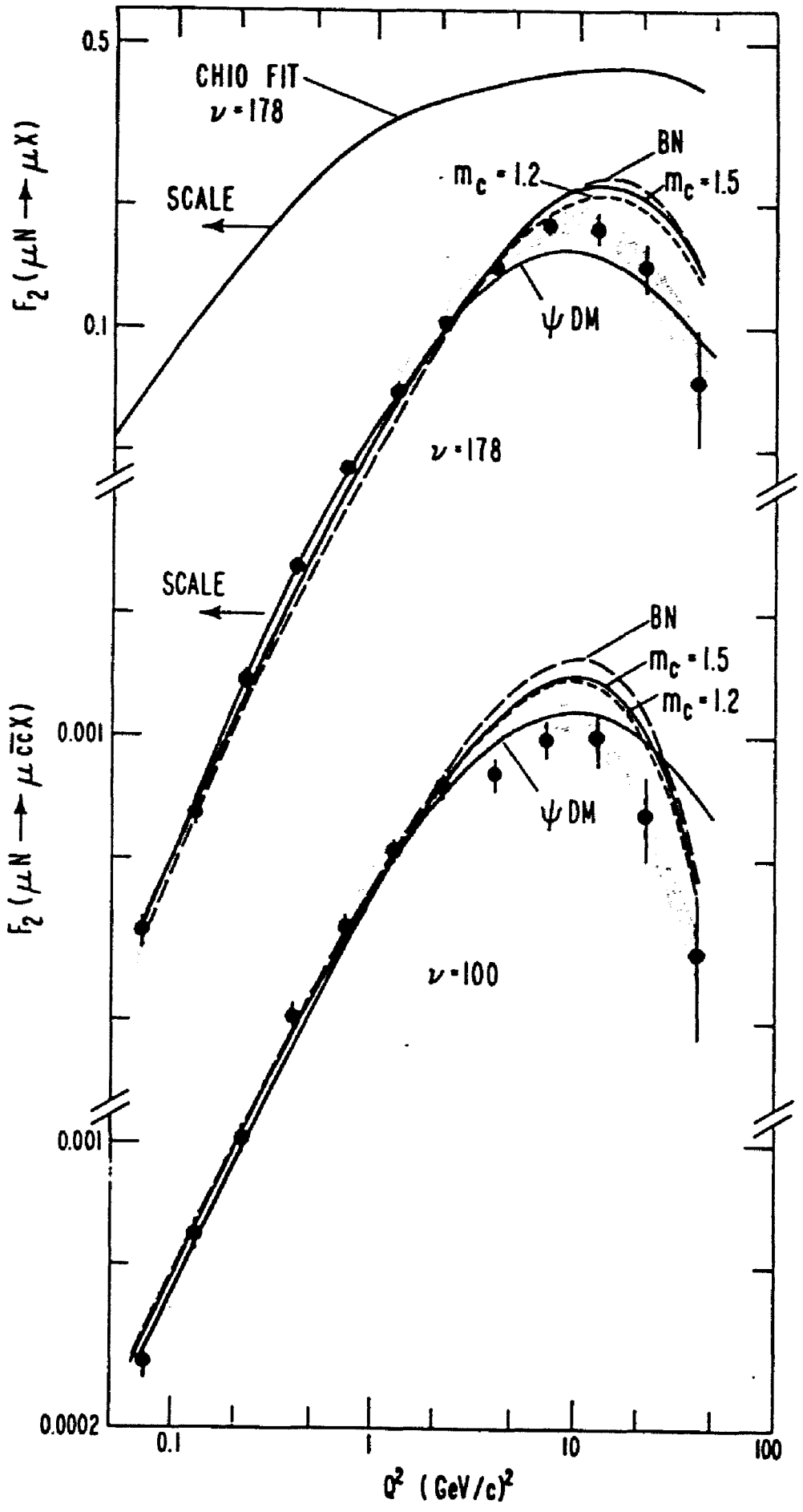

Figure 51.

XBL803-382

Figure 52.-- Scale-noninvariance of $F_2(c\bar{c})$. Data points are arranged in pairs, alternately closed and open. The points in each pair are connected by a solid band and labeled by their common average value of Bjorken $x = Q^2/(2M\nu)$. Errors are statistical. The dashed lines are predictions of the photon-gluon-fusion model with m_c=1.5 GeV/c^2 except that the model is renormalized and damped at high Q^2 as described in the text. The solid bands represent the slope variations allowed by systematic errors. The dot-dashed lines represent the changes in $F_2(c\bar{c})$ as Q^2 is increased but x is held constant that would be necessary to equal the changes in the CHIO fit to F_2 which occur under the same circumstances. The percentages next to these lines indicate the relative sizes of the changes in $F_2(c\bar{c})$ and F_2, fit by CHIO.

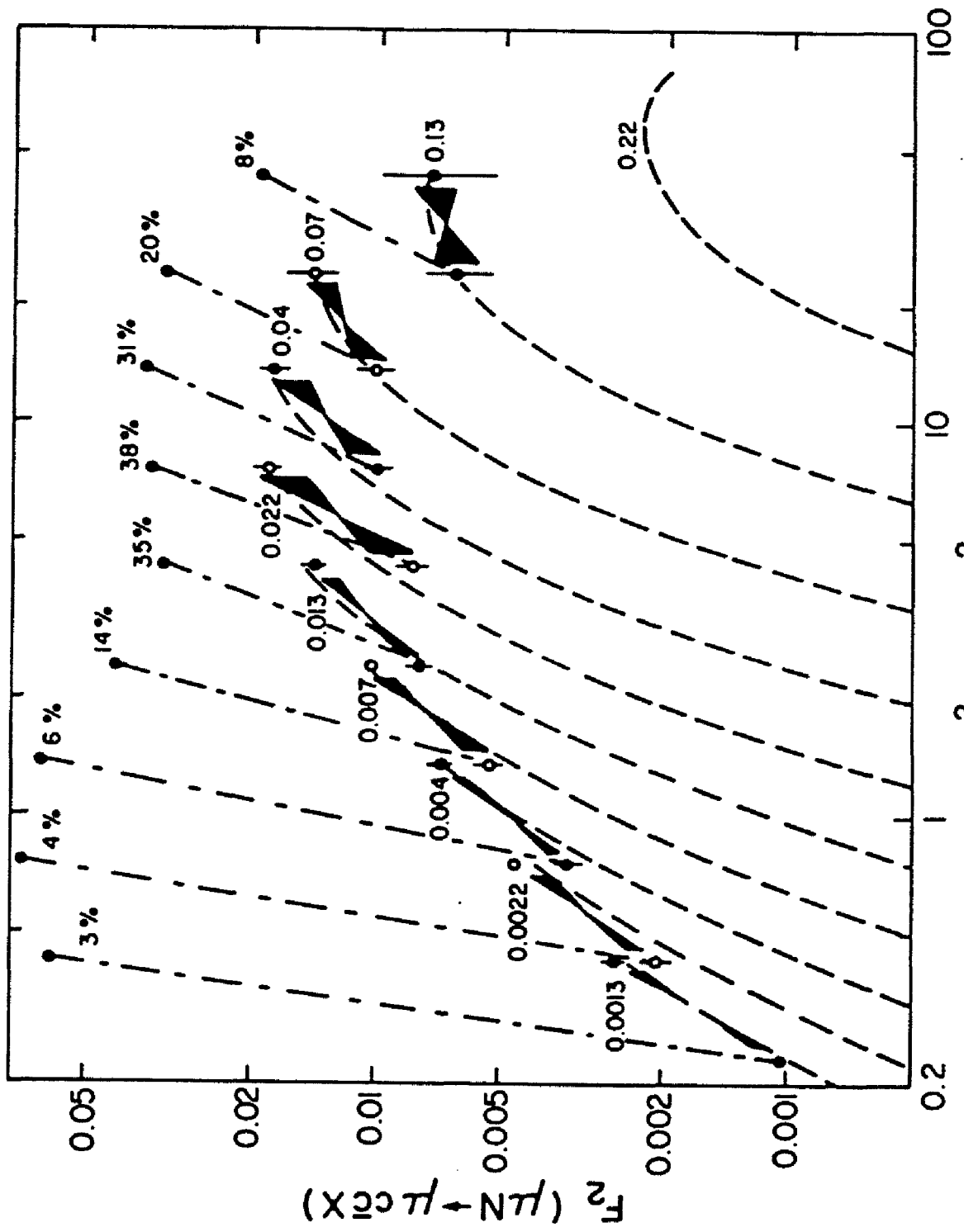

Figure 52.